

Predicting properties of quantum systems by regression on a quantum computer

Andrey Kardashin,^{*} Yerassyl Balkybek, and Vladimir V. Palyulin
Skolkovo Institute of Science and Technology, Moscow 121205, Russia

Konstantin Antipin
*Faculty of Physics, M.V. Lomonosov Moscow State University,
 Leninskie gory, GSP-1, Moscow 119991, Russia and
 Skolkovo Institute of Science and Technology, Moscow 121205, Russia*

Quantum computers can be considered as a natural means for performing machine learning tasks for inherently quantum labeled data. Many quantum machine learning techniques have been developed for solving classification problems, such as distinguishing between phases of matter or quantum processes. Similarly, one can consider a more general problem of regression, when the aim is to predict continuous labels quantifying properties of quantum states, such as purity or entanglement. In this work, we propose a method for predicting such properties. The method is based on the notion of parametrized quantum circuits, and it seeks to find an observable the expectation of which gives the prediction of the property of interest with a low variance. We numerically test our approach in learning to predict (i) the parameter of a parametrized channel given its output state, (ii) entanglement of two-qubit states, and (iii) the parameter of a parametrized Hamiltonian given its ground state. The results show that the proposed method is able to find observables such that they provide highly accurate predictions of the considered properties, and in some cases even saturate the Cramer-Rao bound, which characterizes the prediction error. We also compare our method with the Bayesian approach, and find that the latter prefers to minimize the prediction variance, having therefore a larger bias.

I. INTRODUCTION

Quantum machine learning (QML) is a promising application for quantum computers [1–5]. In QML one commonly considers datasets of labeled classical data points mapped to quantum states via various encoding strategies [6–9]. Often data labeled with discrete labels need to be classified [10–12], or a regression problem has to be solved for predicting continuous labels [13–16].

One approach for solving these problems uses kernel-based methods centered around computing a similarity measure (inner products) between data points [17–19]. The other approach of processing quantum states in QML is built upon the notion of parametrized (sometimes called variational) quantum circuits [20, 21]. Essentially these circuits are parametrized unitary operators used for transforming quantum states [22, 23]. For instance, one can find the ground state of a given Hamiltonian [24–26], solve linear algebra problems [27, 28], perform state [29] and Hamiltonian diagonalization [30–32], etc. Additionally, variational quantum computing methods have been applied for quantum metrology and parameter estimation [33–35], i.e. to find optimal input states and measurements that provide an estimation of parameters of a quantum channel as precise as possible [36–38].

QML techniques can also be used for processing data which are initially quantum. For instance, one can classify phases of matter [39–41], detect anomalies in sets of

quantum states [42, 43], and discern between quantum states [44, 45] and quantum channels [46–48]. Additionally, QML helps with simulating the dynamics of quantum systems [49], detecting and classifying entanglement in quantum states [50, 51], and even with discovery of quantum algorithms [52] as well as error correction codes [53].

In this work, we propose a method for solving regression problems for labeled data represented by quantum states ρ_α with labels α . The method is based on variational quantum circuits, and assumes no knowledge about the connection between the labeled states and their labels. Among such connections, we consider: (i) the labeled state ρ_α is output state of a parametrized channel $\Phi_\alpha[\rho]$ for some fixed input ρ , (ii) α is an entanglement measure of ρ_α , and (iii) $\rho_\alpha = |\psi_\alpha\rangle\langle\psi_\alpha|$ is such that $|\psi_\alpha\rangle$ is the ground state of a parametrized Hamiltonian H_α . Case (i) is often considered in quantum metrology and channel estimation, (ii) is similar to the problem of entanglement quantification [54, 55], and (iii) can be viewed as a generalization of the classification of phases of matter [16].

The performance of our method is assessed with quantum Fisher information, a key concept of quantum metrology [56, 57]. Using that notion, one can lower-bound the error of the prediction of the label. We compare the results given by our method with this bound and with the Bayesian approach [58].

This work is structured as follows. In Section II we formulate the problem setting, describe the method of predicting the labels of labeled states, and introduce the Fisher information and Cramer-Rao bounds, as well as the Bayesian approach. Section III reviews the literature

^{*} andrey.kardashin@skoltech.ru

and states the contribution of our work. Section IV contains analytical considerations of the method we propose. Section V shows the results of the numerical application of the method for solving the regression problems (i)-(iii) mentioned above. The work is concluded with Section VI where we discuss the results and outline directions for further studies.

II. METHODS

We start with establishing the notation and the formulation of the regression problem. For this problem, we present a method for predicting the label of a given datum. Then we discuss the importance of the variance of this prediction, introduce both classical and quantum Fisher information, and use the latter to bound the prediction error.

A. Problem statement

Suppose we are given the following training set:

$$\mathcal{T} = \{\rho_{\alpha_j}, \alpha_j\}_{j=1}^T, \quad (1)$$

where ρ_{α_j} are labeled data points and $\alpha_j \in \mathbb{R}$ are their corresponding labels. We consider the data points to be quantum states described by density operators, i.e. $\rho_\alpha \geq 0$ and $\text{Tr } \rho_\alpha = 1$. Hereinafter, we assume that ρ_α describes a state of n qubits, so that ρ_α acts in a Hilbert space of dimensionality 2^n . Given the training set \mathcal{T} , the goal is to learn the prediction of parameters α for unseen data ρ_α (the data not present in \mathcal{T}).

Essentially, we formulate a regression problem with data points being represented by quantum states. It should be emphasized that we assume no knowledge about the connection of the states ρ_α with their labels α . One instance of such connection is α quantifying the entanglement of the state ρ_α . Thus, our aim is to devise a method for predicting the labels having as little information about the data as possible.

B. The estimator and the cost function

Since the data points ρ_α are quantum states, it is natural to obtain the label α from the expected value of an observable measured in ρ_α . Generally, such expectation will be a function \mathbf{a} of α , which we represent as

$$\mathbf{a}(\mathbf{x}, \Pi, \rho_\alpha) = \sum_i x_i \text{Tr}(\Pi_i \rho_\alpha), \quad (2)$$

where $\mathbf{x} = \{x_i\}_i \subset \mathbb{R}$ and the operators $\Pi = \{\Pi_i\}_i$ form a positive operator-valued measure (POVM),

$$\Pi_i \geq 0, \quad \sum_i \Pi_i = \mathbb{1},$$

where $\mathbb{1}$ is the identity operator. For a given state ρ_α , an estimate of α is formally $\hat{\alpha} = \mathbf{a}^{-1}(\hat{\mathbf{a}})$, where $\hat{\mathbf{a}}$ is an estimate of the expectation \mathbf{a} obtained in a measurement experiment. Essentially, \mathbf{a} is the expected value of an observable represented by a POVM Π with the corresponding measurement outcomes \mathbf{x} measured with respect to ρ_α .

To avoid confusion, we list the notations and terminology we use in this work:

- α is the true label of a labeled state ρ_α .
- \mathbf{a} we call a *prediction* of the label α ; it is obtained as the expected value (2) and generally is a function of α .
- $\hat{\mathbf{a}}$ is an *estimate of the expectation* \mathbf{a} obtained in a measurement experiment; essentially, it is generally a *biased* estimate of the true label α .
- $\hat{\alpha}$ is an *estimate of the true label* α , which can be obtained by inverting the function \mathbf{a} , i.e., $\hat{\alpha} = \mathbf{a}^{-1}(\hat{\mathbf{a}})$.

To find optimal Π and \mathbf{x} in (2), we minimize the least squares between the labels α_j given in \mathcal{T} and our predictions $\mathbf{a}_j(\mathbf{x}, \Pi) \equiv \mathbf{a}(\mathbf{x}, \Pi, \rho_{\alpha_j})$,

$$(\mathbf{x}^*, \Pi^*) = \arg \min_{\mathbf{x}, \Pi} \sum_{j=1}^T \left(\alpha_j - \mathbf{a}_j(\mathbf{x}, \Pi) \right)^2. \quad (3)$$

In other words, the operators Π^* with the corresponding outcomes \mathbf{x}^* form an engineered observable. If this observable is measured with respect to a state ρ_{α_j} , it gives a prediction \mathbf{a}_j presumably as close to a given α_j as possible.

It is not difficult to optimize over a set of real numbers \mathbf{x} . However, the problem is more challenging for Π . Nonetheless, the POVM elements $\Pi_i \in \Pi$ can be found with the variational quantum computing approach. Let us assume that $\Pi_i \Pi_j = \delta_{ij} \Pi_i$ with the operators Π_i being rank-one projectors. With this assumption, we can obtain POVM elements as

$$\Pi_i \equiv \Pi_i(\boldsymbol{\theta}) = U^\dagger(\boldsymbol{\theta}) |i\rangle\langle i| U(\boldsymbol{\theta}), \quad (4)$$

where $|i\rangle\langle i|$ is the projector onto the i th state of the computational basis, and $U(\boldsymbol{\theta})$ is a variational ansatz, i.e., a quantum circuit parametrized by $\boldsymbol{\theta} = \{\theta_k\}_k \subset \mathbb{R}$. That is, instead of optimizing over the operators Π , we optimize over real numbers $\boldsymbol{\theta}$. Denoting $\Pi(\boldsymbol{\theta}) = \{\Pi_i(\boldsymbol{\theta})\}_i$, we rewrite (3) as

$$(\mathbf{x}^*, \boldsymbol{\theta}^*) = \arg \min_{\mathbf{x}, \boldsymbol{\theta}} \sum_{j=1}^T \left(\alpha_j - \mathbf{a}_j(\mathbf{x}, \Pi(\boldsymbol{\theta})) \right)^2. \quad (5)$$

Note that in the case of an orthogonal POVM (4), one can associate the measurement operators Π and the corresponding measurement outcomes \mathbf{x} with an n -qubit

Hermitian operator H , which has \mathbf{x} and Π as its eigenvalues and eigenprojectors, respectively,

$$H(\mathbf{x}, \boldsymbol{\theta}) = \sum_{i=1}^{2^n} x_i \Pi_i(\boldsymbol{\theta}). \quad (6)$$

Omitting the dependence on \mathbf{x} and $\boldsymbol{\theta}$, we can rewrite (2) simply as $\mathbf{a} = \text{Tr } H \rho_\alpha$, i.e., the expected value of H in the state ρ_α . Equivalently, we can say that we transform the state ρ_α with a unitary U , measure the resulting state $U \rho_\alpha U^\dagger$ in the computational basis $\{|i\rangle\langle i|\}_i$, and associate the outcome i with the eigenvalue x_i . Note also that if the ansatz $U(\boldsymbol{\theta})$ is expressive enough, there is always an assignment for \mathbf{x} and $\boldsymbol{\theta}$ such that the decomposition (6) gives any Hermitian matrix of the size $2^n \times 2^n$.

In order to obtain a non-orthogonal POVM, one can utilize the Naimark's extension theorem. Namely, one can attach an auxiliary quantum system to a pure state, say, $|0\rangle\langle 0|$, and find a variational ansatz $U(\boldsymbol{\theta})$ acting on the joint state $\rho_\alpha \otimes |0\rangle\langle 0|$ such that [12, 59]

$$\text{Tr } \Pi_i \rho_\alpha = \text{Tr} \left[U^\dagger(\boldsymbol{\theta}) (\mathbb{1} \otimes |i\rangle\langle i|) U(\boldsymbol{\theta}) (\rho_\alpha \otimes |0\rangle\langle 0|) \right]. \quad (7)$$

Thus, one can measure a non-orthogonal POVM by measuring an orthogonal POVM in an extended Hilbert space. The dimensionality of this extension should coincide with the number of the POVM elements. As we show further in Sections VB 2 and VB 3, Naimark's extension may be advantageous in solving certain regression problems.

C. Number of measured qubits

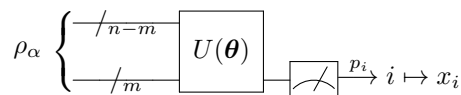
It was assumed above that we measure all qubits of the n -qubit state ρ_α making the number of varied parameters $|\mathbf{x}| = 2^n$ exponentially large. In some cases, however, it may be sufficient to measure only m out of n qubits. Hence, we can modify the observable (6) to

$$H(\mathbf{x}, \boldsymbol{\theta}) = \sum_{i=1}^{2^m} x_i \Pi_i(\boldsymbol{\theta}), \quad (8)$$

for which one can take the POVM elements to be, e.g.,

$$\Pi_i(\boldsymbol{\theta}) = U^\dagger(\boldsymbol{\theta}) \left(\mathbb{1}^{\otimes(n-m)} \otimes |i\rangle\langle i| \right) U(\boldsymbol{\theta}), \quad (9)$$

being now orthogonal projectors of the rank $2^{(n-m)}$. Schematically, the process of measuring such $H(\mathbf{x}, \boldsymbol{\theta})$ with respect to ρ_α can be depicted as follows:



That is, we measure the last $m \leq n$ qubits of the state $\rho_\alpha(\boldsymbol{\theta}) \equiv U(\boldsymbol{\theta}) \rho_\alpha U^\dagger(\boldsymbol{\theta})$ in the computational basis, and

with probability $p_i = \text{Tr}[(\mathbb{1}^{\otimes(n-m)} \otimes |i\rangle\langle i|) \rho_\alpha(\boldsymbol{\theta})]$ get the outcome i associated with x_i , evaluating the expectation therefore to $\text{Tr } H \rho_\alpha = \sum_{i=1}^{2^m} x_i p_i$.

In the case of measuring all n qubits, the parametrized unitary $U(\boldsymbol{\theta})$ can be, for example, a hardware efficient ansatz [25]. If we measure only $m = 1$ or 2 qubits, the circuit may take the form of a quantum convolutional neural network (QCNN) [60]. In Appendix A, we show examples of both such ansätze. In addition to having fixed depth and being resistant to the phenomenon of vanishing gradients [61], QCNNs in our setting also allow to decrease the number of varied parameters to $|\mathbf{x}| = 2^m$. However, as we show in this work, to achieve better results in some cases, one needs to measure all qubits of the n -qubit states; we discuss one of such cases in Section VB 2.

D. Estimation variance

One can estimate the label α of a given ρ_α from the expected value of an observable H measured with respect to the state ρ_α , i.e. from an estimate $\hat{\mathbf{a}}$ of $\mathbf{a} = \text{Tr } H \rho_\alpha$ the desired estimation of the label is obtained as $\hat{\alpha} = \mathbf{a}^{-1}(\hat{\mathbf{a}})$ [62]. Let us now consider the variance of this estimation.

As a simple example, assume that ρ_α is an output state of a single-qubit depolarizing channel acting on an input state ρ :

$$\rho_\alpha = (1 - \alpha)\rho + \frac{\alpha}{2}\mathbb{1}, \quad (10)$$

where the parameter α can take values from 0 to 4/3 [63]. Let us also assume that the input state is $\rho = (\mathbb{1} + \sigma_x)/2 = |+\rangle\langle +|$, where σ_x is a Pauli operator and $|+\rangle = (|0\rangle + |1\rangle)/\sqrt{2}$. Consider a single-qubit Hermitian observable H decomposed in the Pauli basis:

$$H = \sum_{i=0}^3 h_i \sigma_i, \quad h_i \in \mathbb{R},$$

where $\sigma_0 \equiv \mathbb{1}$ is the single-qubit identity. One can show that $h_0 = 1$, $h_1 = -1$, and arbitrary h_2 and h_3 give the expectation $\langle H \rangle_{\rho_\alpha} \equiv \text{Tr } H \rho_\alpha = \alpha$. At the same time, the variance of H in the state ρ_α is

$$\Delta_{\rho_\alpha}^2 H \equiv \langle H^2 \rangle_{\rho_\alpha} - \langle H \rangle_{\rho_\alpha}^2 \quad (11)$$

$$= -\alpha^2 + 2\alpha + h_2^2 + h_3^2. \quad (12)$$

Thus, even if an observable produces a target expectation, the variance could be substantial. This is crucial since the variance $\Delta_{\rho_\alpha}^2 H$ is connected to the mean squared error (MSE) of the estimation $\Delta^2 \hat{\alpha} \equiv \langle (\alpha - \hat{\alpha})^2 \rangle_{\hat{\alpha}}$ via the error propagation formula [58, 64–66]

$$\Delta^2 \hat{\alpha} = \frac{\Delta_{\rho_\alpha}^2 H}{\mu |\partial_\alpha \langle H \rangle_{\rho_\alpha}|^2} = \frac{\Delta^2 \hat{\mathbf{a}}}{|\partial_\alpha \langle H \rangle_{\rho_\alpha}|^2}, \quad (13)$$

where we have used the shorthand $\partial_\alpha \equiv \partial/\partial\alpha$ and μ is the number of measurements. For the derivation of the second equality, and also for a similar expression for a biased estimator, see Appendix B.

Hence, the variance should be included in our label prediction approach. We first rewrite the expressions (2) and (11). Let us denote the probability of obtaining the outcome x_i after measuring Π in the state ρ_α as $p_i = \text{Tr } \Pi_i \rho_\alpha$. Since H has the form (6), we get

$$\mathbf{a} = \sum_i x_i p_i. \quad (14)$$

Similarly, for the variance we obtain

$$\Delta_{\rho_\alpha}^2 H = \sum_i x_i^2 p_i - \left(\sum_i x_i p_i \right)^2. \quad (15)$$

It is important that both the expectation (14) and the variance (15) can be calculated from the same measurement results. Indeed, experimentally, one obtains only the probabilities as frequencies $p_i \approx \mu_i/\mu$ with μ_i being the number of times the outcome x_i was observed, and μ the total number of measurements (or shots). Therefore, with little post-processing overhead we modify the optimization procedure (5) such that it takes into account the variance of our observable,

$$(\mathbf{x}^*, \boldsymbol{\theta}^*) = \arg \min_{\mathbf{x}, \boldsymbol{\theta}} \left(w_{\text{ls}} f_{\text{ls}}(\mathbf{x}, \boldsymbol{\theta}) + w_{\text{var}} f_{\text{var}}(\mathbf{x}, \boldsymbol{\theta}) \right), \quad (16)$$

where

$$f_{\text{ls}}(\mathbf{x}, \boldsymbol{\theta}) = \sum_{j=1}^T \left(\alpha_j - \mathbf{a}_j(\mathbf{x}, \Pi(\boldsymbol{\theta})) \right)^2, \quad (17)$$

$$f_{\text{var}}(\mathbf{x}, \boldsymbol{\theta}) = \sum_{j=1}^T \Delta_{\rho_{\alpha_j}}^2 H(\mathbf{x}, \boldsymbol{\theta}), \quad (18)$$

with $w_{\text{ls}}, w_{\text{var}} > 0$ being the weights. We seek to simultaneously minimize the least squares between the given labels and expectations in (17), and the variance of the observable in (18). Therefore, a weighted sum of these two expressions forms a cost function which is to be minimized in (16). In Sections V A and V C, we show how by adjusting the weights w_{ls} and w_{var} one can trade off between a higher estimation accuracy and a lower variance.

E. Summary and remarks on the method

Let us outline the procedure for solving a regression problem with the proposed method, which may essentially be considered a variational quantum algorithm [22]. Having access to a training set $\mathcal{T} = \{\rho_{\alpha_j}, \alpha_j\}_{j=1}^T$, for each quantum state we compute the expectations

$\mathbf{a}_j(\mathbf{x}, \boldsymbol{\theta}) \equiv \text{Tr } H(\mathbf{x}, \boldsymbol{\theta}) \rho_{\alpha_j}$ of the observable (6) or (8). Similarly, for this observable, we compute the variances $\Delta_{\rho_{\alpha_j}}^2 H(\mathbf{x}, \boldsymbol{\theta})$ defined in (15). These two quantities and the true labels α_j are then inserted into the cost function in (16). Having access to this function, a classical minimization algorithm evaluates it in order to iteratively update the parameters $(\mathbf{x}, \boldsymbol{\theta})$ towards optimal $(\mathbf{x}^*, \boldsymbol{\theta}^*)$, e.g., using a gradient-based optimization algorithm.

We emphasize again that by measuring an observable H in a state ρ_α , one obtains not the exact expectation $\mathbf{a} = \text{Tr } H \rho_\alpha$ itself, but a μ -shot estimation $\hat{\mathbf{a}}$ of it. \mathbf{a} is, generally, a function of α due to a possible bias. After the measurement, the state reduces to one of the eigenstates of the observable. In variational quantum computing, such post-measurement state is normally discarded (not reused for further computations). Thus, one needs to be able to prepare the labeled states ρ_α , or have a number of their replicas¹. However, in most of numerical experiments presented in this work, we assume that we can perform an arbitrary number of measurement shots μ on the labeled states ρ_α , which results in $\hat{\mathbf{a}} = \mathbf{a}$ in the limit $\mu \rightarrow \infty$. In other words, it is supposed that one can compute the expectations $\mathbf{a} = \text{Tr } H \rho_\alpha$ exactly. Nonetheless, in Appendix C 8, we numerically study the performance of the method assuming finite μ .

It also noteworthy that once an optimal observable $H(\mathbf{x}^*, \boldsymbol{\theta}^*)$ is obtained, one can estimate the number of measurements μ to achieve a given MSE $\Delta^2 \hat{\alpha}$ or $\Delta^2 \hat{\mathbf{a}}$ using formula (13). As common for variational quantum algorithms, the post-measurement labeled states ρ_α are again assumed to be discarded. Therefore, we need μ identical replicas of the states to achieve a desired MSE with a given observable.

F. Fisher information

The MSE (13) is known to be lower-bounded by the classical Cramer-Rao bound (cCRB) [58]:

$$\Delta^2 \hat{\alpha} \geq \frac{1}{\mu I_c(\Pi, \rho_\alpha)}, \quad (19)$$

where $I_c(\Pi, \rho_\alpha)$ is the classical Fisher information (cFI) which in our setup can be written as [34]

$$I_c(\Pi, \rho_\alpha) = \sum_i \frac{1}{p_i} \left(\frac{\partial p_i}{\partial \alpha} \right)^2 \quad (20)$$

with p_i depending on α through ρ_α .

Classical Fisher information $I_c(\Pi, \rho_\alpha)$ is known to be upper-bounded by its quantum counterpart $I_q(\rho_\alpha)$. To

¹ To avoid confusion, here we did not use a more common term “copies” as it appears further in a slightly different context.

obtain the latter one introduces the symmetric logarithmic derivative (SLD) operator L ,

$$\partial_\alpha \rho_\alpha = \frac{1}{2}(\rho_\alpha L + L \rho_\alpha), \quad (21)$$

and calculates the quantum Fisher information (qFI) as

$$I_q(\rho_\alpha) = \text{Tr } L^2 \rho_\alpha. \quad (22)$$

In Appendix D we list various ways of finding L and computing $I_q(\rho_\alpha)$.

With qFI, one can obtain a tighter version of the bound (19) called the quantum Cramer-Rao bound (qCRB), namely,

$$\Delta^2 \hat{\alpha} \geq \frac{1}{\mu I_c(\Pi, \rho_\alpha)} \geq \frac{1}{\mu I_q(\rho_\alpha)}. \quad (23)$$

Thus, being dependent on both the measurements Π and state ρ_α cFI $I_c(\Pi, \rho_\alpha)$ is upper bounded by qFI $I_q(\rho_\alpha)$, which depends solely on the state ρ_α . One can find the measurement operators such that cFI attains its maximum [56],

$$\max_{\Pi} I_c(\Pi, \rho_\alpha) = I_q(\rho_\alpha).$$

In order to find such optimal measurements Π , one could compute the eigenprojectors of the SLD operator L introduced in (D1) [58]. Additionally, one can use L itself for constructing an optimal observable

$$H = \alpha \mathbb{1} + \frac{1}{I_q(\rho_\alpha)} L \quad (24)$$

resulting in

$$\langle H \rangle_{\rho_\alpha} = \alpha, \quad \partial_\alpha \langle H \rangle_{\rho_\alpha} = 1, \quad \Delta_{\rho_\alpha}^2 H = \frac{1}{I_q(\rho_\alpha)}.$$

However, the eigenprojectors of L (i.e. also the optimal measurements Π) generally depend on the parameter α to be estimated. Therefore, it is often impossible to find a POVM such that it saturates qCRB over the entire range of α .

One peculiarity of the theory presented in this Section is that it is devised on the assumption that the parameter to be estimated is unknown but fixed [67]. Such a setting is often considered together with the maximum likelihood estimator (MLE). This estimator is unbiased in the limit of large μ . In this limit any other estimator is no better than MLE [65]. Additionally, in the limit $\mu \rightarrow \infty$ MLE saturates the Cramer-Rao bound, which therefore is said to be asymptotically attainable [68, 69]. However, the expressions for CRB (23) themselves are valid for unbiased estimators (the biased case is discussed later in Section IIH) and any μ . Combined with (13), it allows to characterize the observable as

$$\frac{\Delta_{\rho_\alpha}^2 H}{|\partial_\alpha \langle H \rangle_{\rho_\alpha}|^2} \geq \frac{1}{I_q(\rho_\alpha)}, \quad (25)$$

As we show in Appendix B, this relation is preserved in the presence of bias as well. Therefore, we will treat the Cramer-Rao bounds (23) as a figure of merit for our method for predicting the label α for a given ρ_α .

G. Bayesian approach

As we noted above, the estimation theory based on the Fisher information is “local”. Therefore it generally produces a “local” optimal observable when using (24). In practice, the parameter itself can be a random variable with a specific prior probability distribution. Then one can apply the Bayesian approach for finding a “global” optimal observable. In this approach, one minimizes the (Bayesian) MSE for a parameter $\theta \in [a, b]$ obtained by the measurement of an observable M [58, 70]:

$$\Delta_B^2 \theta = \int_a^b \text{Pr}(\theta) \text{Tr } \rho(\theta) (M - \theta \mathbb{1})^2 d\theta, \quad (26)$$

where $\text{Pr}(\theta)$ is the prior probability distribution for θ . Note that here we denote the parameter to be estimated and the corresponding observable as θ and M , respectively, for a better distinguishability with the proposed method (16). The optimal observable M_0 minimizing the MSE (26) satisfies

$$\frac{1}{2} (\bar{\rho} M_0 + M_0 \bar{\rho}) = \bar{\theta} \bar{\rho}, \quad (27)$$

where

$$\bar{\rho} = \int_a^b \text{Pr}(\theta) \rho(\theta) d\theta \quad (28)$$

is a prior-weighted density operator and

$$\bar{\theta} \bar{\rho} = \int_a^b \text{Pr}(\theta) \theta \rho(\theta) d\theta \quad (29)$$

is the prior mean operator [58]. If $\bar{\rho}$ is strictly positive, the solution M_0 of (27) is unique [70].

The optimal observable M_0 gives rise to the Bayesian quantum Cramer-Rao bound [58]

$$\Delta_B^2 \theta \geq \Delta_p^2 \theta - I_B, \quad (30)$$

where

$$\Delta_p^2 \theta = \int_a^b \text{Pr}(\theta) \theta^2 d\theta \quad (31)$$

and

$$I_B = \text{Tr } \bar{\rho} M_0^2, \quad (32)$$

the *quantum Bayes information*. Therefore, one can use (30) to assess the quality of the solution obtained, but the optimal observable M_0 has to be known. Alternatively for this purpose, the van Trees bound can be used [35, 67, 71]. In addition to these bounds, one can characterize the performance of the Bayesian approach by entropic quantities, such as the mutual information between the parameter and the measurement [72].

In this work, we also compare the observables found by minimizing the Bayesian MSE (26) to the ones obtained with our method (16). Importantly, in Section IV C we show that under specific assumptions the method (16) reduces to the Bayesian MSE (26) if one puts equal weights $w_{\text{ls}} = w_{\text{var}}$ and the flat prior $\text{Pr}(\theta) = 1/(b-a)$.

H. Biased estimator

The expected value of an observable H measured in the state ρ_α allows an estimation of α for a given ρ_α . This estimation could also contain a bias $b(\alpha)$, i.e. [58]

$$\mathbf{a} \equiv \text{Tr } \rho_\alpha H = \alpha + b(\alpha),$$

with the estimation $\hat{\mathbf{a}}$ obtained from a measurement with the MSE $\Delta^2 \hat{\mathbf{a}} = \Delta^2 H / \mu$ [62, 64, 73]. In this biased case, the earlier expressions have to be adjusted. Indeed, if $b \neq 0$, instead of the MSE $\Delta^2 \hat{\alpha}$, one would rather observe $\langle (\hat{\mathbf{a}} - \alpha)^2 \rangle$ in an experiment. We can transform the corresponding formulas (13) and (19) to [69]

$$\langle (\hat{\mathbf{a}} - \alpha)^2 \rangle = \frac{\Delta^2 H}{\mu} + b^2, \quad (33)$$

$$\langle (\hat{\mathbf{a}} - \alpha)^2 \rangle \geq \frac{|\partial_\alpha \langle H \rangle|^2}{\mu I_q} + b^2. \quad (34)$$

See Appendix B for a detailed derivation. In Appendix C 8, these expressions are used to verify our numerical experiments with finite μ .

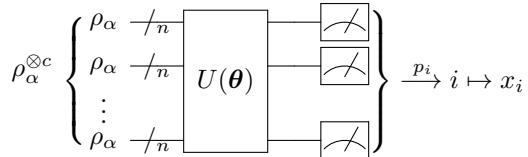
We note again that similarly to (13) and (23), for an optimized observable H from the expression (33) one can estimate the number of measurements μ needed for achieving a desired error of estimating the label α [74]. Indeed, since we engineer the observable H ourselves, we know its variance on the states of the training set, as well as the bias b , from which one can also approximate $\partial_\alpha \langle H \rangle_\alpha = \partial_\alpha b + 1$ (see Appendix B).

The bias of estimation could be worked around by inversion of the function \mathbf{a} [75]. Indeed, if \mathbf{a} is bijective within a range of α , then one gets the desired estimation as $\hat{\alpha} = \mathbf{a}^{-1}(\hat{\mathbf{a}})$. Alternatively, one could try to compensate the bias $b(\alpha)$, as one extracts it from the difference between the prediction \mathbf{a} and the true labels α given in the training set \mathcal{T} (see Appendix C 4).

Another strategy of sorting out an unwanted bias is to modify the prediction itself,

$$\mathbf{a}(\mathbf{x}, \boldsymbol{\theta}, c, \rho_\alpha) = \text{Tr } H(\mathbf{x}, \boldsymbol{\theta}) \rho_\alpha^{\otimes c}, \quad (35)$$

i.e. we process c copies of the n -qubit state ρ_α *simultaneously* as one joint state $\rho_\alpha^{\otimes c}$, and so that H is now a cn -qubit observable. In line with Sec. II C, calculating the quantity (35) can be schematically depicted as follows:



That is, here we seek to find an observable H acting on the composite state $\rho_\alpha^{\otimes c}$, which is now treated as a *one* labeled state with the label α . This introduces a non-linearity to the prediction [76, 77], and similar techniques

are utilized in QML to improve its performance [9, 12, 19, 21, 78]. In Appendix C 9 c we apply this method to a problem of predicting α for $\rho_\alpha = e^{-i\alpha\sigma_z/2} |+\rangle\langle+| e^{i\alpha\sigma_z/2}$, in which case one cannot find H giving the expectation $\text{Tr } H \rho_\alpha = \alpha$. However, we show that for any $c \geq 1$ there is an observable H_c such that the expectation $\text{Tr } H_c \rho_\alpha^{\otimes c}$ gives the first c terms of the Fourier series of the linear function $f(\alpha) = \alpha$.

III. RELATION TO THE LITERATURE

There is a vast amount of literature dedicated to QML and its various aspects. One of such aspects is the capability of QML-models of generalization, i.e., the performance of trained models on unseen data. The ability of a model to generalize has been studied with respect to, e.g., the size of the training set [78, 79] or number of accesses to the process preparing a data point [80], number of parametrized gates in the variational circuit [81], data encoding strategy [82], and classical and quantum information-theoretic quantities measuring correlation between training data and learner's hypothesis [12, 83]. In our work, we do not study this aspect of our method analytically. However, we observe that the number of states for training depends on the connection between the labeled state and its label. Among the considered problems only entanglement quantification requires a substantial training set size which we study numerically.

Another aspect of QML considered in the literature is the construction of models. QML models can be based on shadow tomography [84, 85]. This approach can be used for predicting the expectation of an exponential number of arbitrary two-outcome observables in state ρ by *simultaneously* measuring a polynomial number of copies of ρ . Based on shadow tomography and other clever measurement and post-processing techniques, the work [80] proposes an algorithm such that given n copies of an n -qubit state ρ , it efficiently predicts expectations $\text{Tr } P \rho$ for *all* Pauli strings P . Moreover, as shown in [86], conducting collective measurements on only two copies of state allows classification of observables and quantum processes. Regarding the latter, the work [87] describes, inter alia, an algorithm which learns a quantum process from collective measurements on not necessarily identical state copies.

Shadow tomography and related techniques require to measure many copies of the state as a whole, which demands for a quantum memory to store the copies. To circumvent this obstacle, the work [88] introduced the notion of classical shadows. A classical shadow is essentially a collection of results of randomized measurements conducted for a given state. Similarly to the shadow tomography, this method also allows to predict the expectations of observables, but the copies of a state can be measured *independently*. However, the number of copies needed for accurate prediction depends on the so-called

shadow norm of the observables in question as well as on the way random measurements are performed. For QML, classical shadows were utilized in [89] for learning states and unitaries. Closer to our setting is one of the algorithms described in [90], where an unknown observable O is learned assuming a training set of the form $\{\rho_{\alpha_j}, \text{Tr } O\rho_{\alpha_j}\}_j$. This may not hold for some cases, for instance, if the labels α_j enter the states ρ_{α_j} only non-linearly. Nonetheless, this algorithm should still be applicable for labels α with arbitrary connection to ρ_α .

The notion of classical shadows gives rise to the concept “*measure first, ask questions later*” [91]. Indeed, a classical shadow is essentially a classical representation of a quantum state. Once obtained, it can be utilized for various purposes, including solving machine learning tasks. For example, classical shadows can be fed into a classical neural network which learns to classify phases of matter [92], even in the unsupervised setting [86, 91]. More generally, for classical data, one can train a so-called shadow model [93] by using the classical shadows technique for training a quantum device to produce bit-string “advice” for a classical algorithm. The latter is then used for evaluating the labels without the need for the quantum device. Although such methods are appealing as they minimize the use of quantum resources, they also have their limits of applicability [93, 94].

As in the present work, QML models can also be designed in a different setting, the setting of variational quantum computing [22, 95]. This approach is believed to be suitable for noisy intermediate scale quantum (NISQ) devices. Although we also consider processing several copies of a labeled state, doing so for many copies (as required for shadow tomography and related methods) may be prohibitive for such devices [96]. As for classical shadows, one could try to perform random Clifford measurements for estimating the expectations of (8). In our setting, however, estimating this expectation in a given labeled state with a desired precision ϵ would require about $m2^{n-m} \max_i(x_i^2/\epsilon^2)$ measurements (see Theorem 1 in [88]). Therefore, the larger m is, the fewer measurements we need to conduct, but the more parameters we need to vary. Here we do not apply this technique and leave it for future considerations.

Within the variational quantum computing approach the work [16] considers quantum simulation of multiparticle states governed by a specific Lagrangian aiming at prediction of one of its parameters. The authors apply a QCNN to transform the states and measure a single-qubit observable σ_z , the expectation of which is used as a prediction for the parameter. We consider a similar problem of predicting the strength of the transverse field h of the Ising Hamiltonian H_h given its ground state $|\psi_h\rangle$. One difference between our work and [16] is that we accompany our numerical experiments with the simulation of finite number of measurement shots (see Appendix C 8), and compare the variance of the optimized observable against qCRB.

A QCNN was also utilized in [75] to approximate a

μ -shot estimate \hat{a} of the expectation $a = \text{Tr } \rho_\alpha O$ by a trigonometric polynomial $f(\alpha)$ and obtain the desired parameter as its inverse. The authors prove that the approach works well (in terms of required μ) for any non-trivial observable O and certain dependencies of ρ_α and a on α . In one of the numerical experiments, they considered finding an optimal observable for predicting the angle α of a unitary rotation of a state of n qubits. Similarly to [16], the observable had the form of a single-qubit operator σ_z transformed by a QCNN. The MSE given by the optimized observable scales as $1/n^2$, i.e. it follows the ultimate Heisenberg limit [37]. To optimize the observable, the authors minimized the MSE between f/n and α , where the factor $1/n$ was introduced for achieving the Heisenberg limit.

Our approach of optimizing the observable is different, as we account for its variance (linked to the MSE of estimation via (13) or (33)) through explicit addition of it to the cost function. Additionally, we test our method on a variety of tasks, including entanglement quantification. Another difference with [16] and [75] is in our observable being many-qubit. This may be important as we notice that measuring one qubit out of many may result in higher prediction variance. We emphasize that what matters here is apparently not the observable’s locality itself, but the dimensionality of its eigenprojectors, see Sections V B 2 and V B 3. Additionally, we can vary the spectrum of our observable which brings more flexibility.

The idea of parametrizing the observable’s spectrum was recently proposed in [97]. In the reference, classical data α are encoded into quantum states via a parametrized unitary $V(\alpha)$. This allows to utilize the data re-uploading techniques [6–8], i.e. one can alternate between the encoding unitary $V(\alpha)$ and variational circuits $U(\theta_i)$ for achieving higher prediction accuracy. In contrast to [97], in our regression tasks we consider data which are initially quantum. For such data, the re-uploading techniques are not applicable, unless we have access to the process Φ_α taking as input an initial state ρ and producing the labeled state $\Phi_\alpha[\rho]$ for a given label α . However, we consider processing c copies of the labeled state as one joint state (i.e., $\rho_\alpha^{\otimes c}$) which may introduce a desired non-linearity [76, 78].

Also in [97] it is proposed to parametrize the observable in the Pauli basis with variable coefficients. In our approach, we represent the observable as a linear combination of eigenprojectors with parameters being the eigenvalues. Although the two techniques are similar, ours is more compatible with the notion of SLD operators (21), as well as more transparent in application to Naimark’s extension (7) which readily translates into working with general POVM elements. Naimark’s extension may play an important role if one wants to measure fewer qubits with no harm to the prediction variance (see Section V B 2). Additionally, in contrast to the observable parametrization proposed in [97], our parametrization *always* allows to compute $\text{Tr } H^2 \rho_\alpha$ by only a classical post-processing of the measurement results obtained for

computing $\text{Tr } H\rho_\alpha$.

We also provide analytical results for the proposed method. Assuming a large size of the training set, we write an equation for finding an optimal observable and derive upper bounds on its variance. Interestingly, the obtained optimal observable cannot give unbiased predictions on the whole range of the labels. Importantly, we also show that with equal weights in (16), our method is reducible to minimizing the Bayesian MSE, an approach for finding a global observable. For this approach, variational quantum algorithms have also been developed [35, 98, 99], as well as executed experimentally [100].

In both our work and [97], the variance of the observable is taken into account. We propose the assessment of the quality of the solution by comparing the variance against the Cramer-Rao bounds. The idea comes from quantum metrology [37, 65, 66]. One is given a usually *known*, but possibly noised parametrized channel Φ_α with an aim to find an optimal input state ρ and measurements for the output state $\Phi_\alpha[\rho]$ allowing a more accurate prediction of the parameter α . For this setting, there exist variational algorithms as well [33, 34]. One typically varies the input states and measurements to maximize the Fisher information about the *fixed* parameter α . The Fisher information under maximization may be classical or quantum, or it may be an easier-to-compute surrogate of the latter [101]. Our setting is slightly different, as the parameter α may take values from a fairly wide interval. Additionally, we assume no knowledge about the channel Φ_α , nor do we control the input states ρ for it.

IV. THEORETICAL ARGUMENTS

In this Section, we analyze the method introduced in (16). Assuming certain approximations, we first obtain an equation for an optimal observable H . Then, we derive upper bounds on the total variance of the parameter prediction. Finally, we show that for the condition $w_{\text{ls}} = w_{\text{var}}$ and uniform distribution of the labels, our method is equivalent to the minimization of the Bayesian MSE.

A. Approximation for the optimal observable

When a training set comprises some fixed family of states $\{\rho_\alpha\}_\alpha$, the solution of the optimization procedure (16) can be approximated by the solution of the minimization problem

$$\min_H w_{\text{ls}} \int_a^b (\text{Tr } \rho_\alpha H - \alpha)^2 d\alpha + w_{\text{var}} \int_a^b (\text{Tr } \rho_\alpha H^2 - (\text{Tr } \rho_\alpha H)^2) d\alpha \quad (36)$$

with fixed non-negative weights $w_{\text{ls}}, w_{\text{var}}$. Here it is supposed that finite sums in Eqs. (17) and (18) can be ap-

proximated by integrals over the range $[a, b]$ of possible values of the predicted parameter α provided that the distribution of the training sample's labels is dense enough.

The optimization problem (36) can be treated analytically with the use of the method which was demonstrated in the context of quantum state discrimination in Chapter 2 of Ref. [102]. Considering a small perturbation ϵ around the optimal observable H_0 by an arbitrary Hermitian operator Y , $H = H_0 + \epsilon Y$, we obtain that $H^2 = H_0^2 + \epsilon(H_0 Y + Y H_0) + \epsilon^2 Y^2$. Substituting expressions for H and H^2 into (36) and setting the contribution in front of ϵ to zero yields

$$w_{\text{var}} \int_a^b \text{Tr } \rho_\alpha (H_0 Y + Y H_0) d\alpha + 2(w_{\text{ls}} - w_{\text{var}}) \int_a^b \text{Tr}(\rho_\alpha Y) \text{Tr}(H_0 \rho_\alpha) d\alpha - 2w_{\text{ls}} \int_a^b \alpha \text{Tr}(\rho_\alpha Y) d\alpha = 0. \quad (37)$$

The contribution in front of ϵ^2 reads

$$w_{\text{ls}} \int_a^b (\text{Tr } \rho_\alpha Y)^2 d\alpha + w_{\text{var}} \int_a^b (\text{Tr } \rho_\alpha Y^2 - (\text{Tr } \rho_\alpha Y)^2) d\alpha. \quad (38)$$

This expression is non-negative since $(\text{Tr } \rho_\alpha Y)^2 \leq \text{Tr } \rho_\alpha Y^2$ as a particular case of the inequality [103]

$$f(\text{Tr } \rho X) \leq \text{Tr } \rho f(X), \quad (39)$$

which holds for a convex function f , a Hermitian operator X , and a state ρ . Non-negativity of the expression (38) implies that the operator H_0 , which satisfies (37) for any Y , is the solution to the minimization problem (36). Making use of the fact that (37) holds for any Hermitian Y , inside the trace we can gather all the terms that are multiplied by Y and set their sum to zero. We arrive at an operator equation for the optimal observable H_0 :

$$\frac{1}{2} (\tilde{\rho} H_0 + H_0 \tilde{\rho}) - \frac{k}{L} \int_a^b \alpha \rho_\alpha d\alpha + \frac{(k-1)}{L} \int_a^b \text{Tr}(H_0 \rho_\alpha) \rho_\alpha d\alpha = 0, \quad (40)$$

where

$$\tilde{\rho} = \frac{1}{L} \int_a^b \rho_\alpha d\alpha, \quad L = b - a, \quad k = \frac{w_{\text{ls}}}{w_{\text{var}}}, \quad (41)$$

with dependence on weights being isolated in the factor k , and hence only the ratio of weights matters.

The structure of (40) can be used to get the following general property of the optimal observable H_0 . Applying the trace to both sides and simplifying the result one gets

$$\int_a^b \text{Tr}(H_0 \rho_\alpha) d\alpha = \int_a^b \alpha d\alpha = \frac{b^2 - a^2}{2}, \quad (42)$$

i.e. irrespective of weights the area under the prediction curve equals to the area under the straight line corresponding to the true values of the label. The manifestation of this property can be most clearly seen in Fig. 6 (left) and Fig. 23 (left).

B. Upper bound on the total variance

When the ratio of weights $k \leq 1$, Eq. (40) also implies an upper estimate on the total variance of the optimal observable H_0 . In Appendix E, we derive the following bound:

$$\int_a^b \Delta^2 H_0 d\alpha \leq k \left(\frac{b^3 - a^3}{3} - \frac{(b^2 - a^2)^2}{4L} \right). \quad (43)$$

This expression shows that the total variance can be made arbitrarily small by choosing a sufficiently small weight ratio k . Assuming $a = 0$ and $b = L$, for the *average* total variance one obtains

$$\frac{1}{L} \int_0^L \Delta^2 H_0 d\alpha \leq \frac{kL^2}{12}, \quad (44)$$

i.e. the average total variance for this particular case can be made less than ϵ by selecting the weight ratio as small as $k \leq \min(1, 12\epsilon/L^2)$.

Eqs. (43) and (44) point to the fact that the procedure (16) can be regarded as the *variance regularization*, the term used in Ref. [97].

We note that the total variance of the optimal observable (43) for *all finite* k can be expressed as (see Appendix E)

$$\begin{aligned} \int_a^b \Delta^2 H_0 d\alpha \\ = k \int_a^b (\alpha \text{Tr} \rho_\alpha H_0 - (\text{Tr} \rho_\alpha H_0)^2) d\alpha. \end{aligned} \quad (45)$$

This expression shows that at finite k the prediction $\text{Tr} \rho_\alpha H_0$ will never coincide exactly with the true values α at each point of the domain $[a, b]$. Indeed, let us suppose that there is no bias at each point α . Then, according to (45), the total variance and hence the variance for all α is equal to zero, which implies an observable H_0 giving a constant prediction $\langle H_0 \rangle_{\rho_\alpha} = c$. This, in turn, leads to a bias $b = c - \alpha$, which contradicts the initial assumption that $\text{Tr} \rho_\alpha H_0 = \alpha$ for any $\alpha \in [a, b]$. Therefore, in the prediction of the parameter according to the procedure (16), there will always be a bias with finite k .

C. Comparison with the Bayesian approach

At equal weights $w_{\text{ls}} = w_{\text{var}} = 1$, the sum of the two terms in (36) simplifies, and the optimization problem

reduces to

$$\min_H \int_a^b \text{Tr} \rho_\alpha (H - \alpha \mathbb{1})^2 d\alpha. \quad (46)$$

This is a minimization of MSE of the observable H over the interval $[a, b]$, which can be compared with the optimization task from the Bayesian approach introduced in Section II G. For more instructive comparison, for the Bayesian approach we denote the parameter under prediction as θ and the corresponding observable as M . Recall that in this approach, the parameter θ is a random variable which follows a prior probability distribution $\text{Pr}(\theta)$. The Bayesian MSE for θ , which is obtained by the measurement of an observable M , reads

$$\Delta_B^2 \theta = \int_a^b \text{Pr}(\theta) \text{Tr} \rho(\theta) (M - \theta \mathbb{1})^2 d\theta. \quad (47)$$

From the last two expressions, it is seen that the minimization task (46) is equivalent to the minimization of (47) if the prior is uniform (or *flat*), i.e., $\text{Pr}(\theta) = 1/(b - a)$. Consequently, the optimization problem (36) with equal weights ($w_{\text{ls}} = w_{\text{var}}$) is equivalent to minimization of the Bayesian MSE with the flat prior.

The correspondence stated above can also be seen at the level of the solutions to the optimization problems. Setting $k = 1$ (equal weights) in (40), one obtains

$$\frac{1}{2} (\tilde{\rho} H_0 + H_0 \tilde{\rho}) = \tilde{\alpha} \tilde{\rho}, \quad (48)$$

where

$$\tilde{\alpha} \tilde{\rho} = \frac{1}{L} \int_a^b \alpha \rho_\alpha d\alpha. \quad (49)$$

The equation (48) for the optimal observable H_0 resembles the equation (27) for the optimal observable M_0 minimizing Bayesian MSE (26). When the prior $\text{Pr}(\theta)$ is uniform, (27) exactly coincides with (48). At the same time, the solution of the problem (36) with non-equal weights can differ substantially from the Bayesian solution for flat prior in terms of approximation error and variance (see Section V A).

V. RESULTS

In this Section, we present the results of numerical experiments of the regression problem solution for the data of the form (1) with our method, i.e., we solve the optimization problem (16), minimizing the least squares (17) between the true parameters α and our predictions a as well as the variance of the observable (18) simultaneously. That is, we show the results of applying our method to predict the parameter of a channel Φ_α given its output state ρ_α , the entanglement of various families of states, and the parameter of a Hamiltonian H_α given its ground state $|\psi_\alpha\rangle$. In our numerical experiments, we assume that

we can calculate the expectations $\mathbf{a} = \text{Tr } H \rho_\alpha$ exactly. However, in Appendix C 8, we also perform simulations with \mathbf{a} obtained as μ -shot estimates $\hat{\mathbf{a}}$.

Where applicable, the classical and quantum Fisher informations were calculated using formulas (20) and (D5), respectively. If not stated otherwise, we use a hardware-efficient ansatz described in Appendix A to represent the parametrized unitary $U(\boldsymbol{\theta})$, and set $w_{\text{ls}} = 1$ and $w_{\text{var}} = 10^{-4}$. For optimization, the BFGS algorithm from the SciPy library [104] is applied. Additionally, we use tools from the QuTiP package [105, 106].

A. Predicting the parameter of the amplitude-damping channel

As the first test case, let us consider the amplitude damping (AD) channel

$$\Phi_\alpha[\rho] = \sum_{k=1}^2 V_k(\alpha) \rho V_k^\dagger(\alpha) \quad (50)$$

with Kraus operators

$$V_1(\alpha) = \sqrt{\alpha} |0\rangle\langle 1|, \quad V_2(\alpha) = |0\rangle\langle 0| + \sqrt{1-\alpha} |1\rangle\langle 1|.$$

The input state $\rho = |+\rangle\langle +|$ is used to obtain the output

$$\rho_\alpha \equiv \Phi_\alpha[\rho] = \frac{1}{2}(\mathbb{1} + \sqrt{1-\alpha}\sigma_x + \alpha\sigma_z) \quad (51)$$

As we show in Appendix C 9 b, the SLD operator for this state has eigenvectors dependent on the parameter α . Hence, there may be no option to find an optimal observable from the construction (24), as such an observable will depend on α and hence will not be global.

In order to find the global optimal observable, we need to solve the equation (40) directly. After several transformations, one gets

$$\begin{aligned} \frac{1}{2}(\tilde{\rho}H_0 + H_0\tilde{\rho}) + \frac{(k-1)}{L} \int_a^b \text{Tr}(\rho_\alpha H_0) \rho_\alpha d\alpha \\ - \frac{k}{2L}(c_2\mathbb{1} + (c_1 + c_3)\sigma_x + c_4\sigma_z) = 0, \end{aligned} \quad (52)$$

where

$$\tilde{\rho} = \frac{1}{2L}(L + c_1\sigma_x + c_2\sigma_z) \quad (53)$$

and

$$\begin{aligned} c_1 &= \frac{2}{3}((1-a)^{3/2} - (1-b)^{3/2}), \\ c_3 &= \frac{2}{5}((1-b)^{5/2} - (1-a)^{5/2}), \\ c_2 &= \frac{b^2 - a^2}{2}, \quad c_4 = \frac{b^3 - a^3}{3}. \end{aligned}$$

We look for the observable in the form

$$H_0 = \frac{1}{2}(h_0\mathbb{1} + h_1\sigma_x + h_2\sigma_y + h_3\sigma_z). \quad (54)$$

Substituting it into (52), after simple but tedious calculations with Pauli matrices we obtain $h_2 = 0$ and the following linear system of equations

$$\begin{cases} Lh_0 + c_1h_1 + c_2h_3 = 2c_2, \\ kc_1h_0 + (L + (k-1)(L - c_2))h_1 \\ \quad + (k-1)(c_1 + c_3)h_3 = 2k(c_1 + c_3), \\ kc_2h_0 + (k-1)(c_1 + c_3)h_1 \\ \quad + (L + (k-1)c_4)h_3 = 2kc_4. \end{cases} \quad (55)$$

Solving (55) for h_0, h_1, h_3 , and for given values of a and b , we can construct our global optimal observable H_0 from (54).

In Fig. 1, we compare the predictions $\mathbf{a} = \text{Tr } H(\mathbf{x}^*, \boldsymbol{\theta}^*) \rho_\alpha$ of the parameter α of the AD channel for the observables $H(\mathbf{x}^*, \boldsymbol{\theta}^*)$ obtained with the two optimization procedures: Via our method (16) with $w_{\text{ls}} = 1$ and three different weights w_{var} , and via the Bayesian approach (26) with uniform prior. Namely, in the former, we trained our model on a set $\mathcal{T} = \{\rho_{\alpha_j}, \alpha_j\}_{j=1}^{500}$ of (deliberately) excessively large size $T = 500$ with equidistant labels α_j . In the latter, we minimize the Bayesian MSE:

$$(\mathbf{x}^*, \boldsymbol{\theta}^*) = \arg \min_{\mathbf{x}, \boldsymbol{\theta}} \int_0^1 \text{Tr} \rho_\alpha (H(\mathbf{x}, \boldsymbol{\theta}) - \alpha \mathbb{1})^2 d\alpha. \quad (56)$$

In order to execute this procedure, one needs an access to the process which prepares ρ_α for a given α . This may be impossible if, e.g. α is an entanglement measure of a random state ρ_α . However, the integral in (56) can be approximated by a sum for discrete values of α present in the training set [100].

Fig. 1 shows that our procedure with equal weights $w_{\text{ls}} = w_{\text{bar}}$ coincides with the Bayesian one with the flat prior. With no preliminary knowledge about the parameter, the Bayesian method produces a rather large prediction error in exchange for smaller variance. The former can be decreased by replacing the Bayesian method with the procedure (16) and by choosing smaller weights w_{var} , again, in exchange for larger variance.

In Fig. 1 the obtained results are also compared with theoretical predictions according to (40), (54), and (55). As we see, the solutions to (55) match well the numerical results of application of our method (16) and minimizing the Bayesian MSE (56). Furthermore, with the solution to (55) for $k = 1$, one can calculate the Bayesian qCRB (30) to obtain

$$\Delta_B^2 \alpha = \Delta_p^2 \alpha - I_B = \frac{178}{2475} \approx 0.0719$$

This value of Bayesian MSE was achieved by the variational procedure (56) in our numerical results, signifying the saturation of the bound.

In order to numerically test our analytical expressions obtained in Section IV, here we trained our model (16) on a set of a large size $T = 500$. However, as we show in Appendix C 9 b, one can get good results having a training set of a much smaller size of $T = 5$ data points.

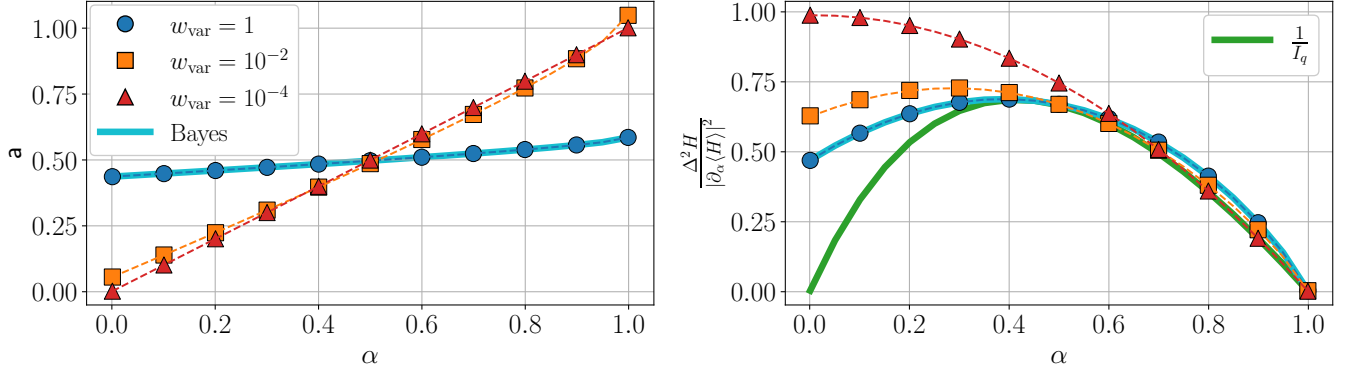


FIG. 1. Left: Predicted \hat{a} vs. true α parameter of the AD channel (50) for fixed $w_{\text{ls}} = 1$ different weights w_{var} . Right: Variance (25) of the optimized observable H vs. true α . In both panels, the solid blue line shows the data produced by the observable obtained by minimizing the Bayesian MSE (56); the dashed lines indicate the data given by the observable obtained from the solution of (55).

Additionally for this regression problem, in Appendix C 8 a we train the model assuming that the expectations $\mathbf{a} = \text{Tr } H \rho_\alpha$ are obtained as μ -shot estimates $\hat{\mathbf{a}}$. As this problem is relatively simple for our method, even $\mu = 2^6$ is enough to achieve good prediction accuracy.

B. Predicting the entanglement of two-qubit states

Here we test our method for entanglement quantification [54, 55, 107–110] for various families of two-qubit states. Namely, we train our model to predict the negativity N of a given two-qubit state ρ ,²

$$N(\rho) = \|\rho^{T_2}\|_1 - 1, \quad (57)$$

where $\|\cdot\|_1$ is the trace norm, and $\rho^{T_2} \equiv (\mathbb{1} \otimes T)[\rho]$ is the partial transpose of ρ with respect to the second qubit. For more details on the negativity and bipartite entanglement overall, see Appendix F.

1. Bell-type states

First, we train the model (16) to predict the negativity (57) of Bell-type states of the form

$$|\Phi_p^+\rangle = \sqrt{p}|00\rangle + \sqrt{1-p}|11\rangle. \quad (58)$$

The training set is $\mathcal{T} = \{|\Phi_{p_j}^+\rangle, N_j\}_{j=1}^5$, where the coefficients p_j are picked randomly from a uniform distribution. The observable H is composed in the form (8) and only $m = 1$ qubit of a two-qubit state (58) is measured.

² We dropped an additional factor $1/2$ which often appears in the literature. All related expressions have been modified accordingly.

Fig. 2 shows the performance of the trained model on the testing set $\mathcal{V} = \{|\Phi_{p_j}^+\rangle, N_j\}_{j=1}^{10}$ with equidistant negativities N_j . As can be seen, not only the accurate predictions $\mathbf{N} = \langle \Phi_p^+ | H(\mathbf{x}^*, \boldsymbol{\theta}^*) | \Phi_p^+ \rangle$ of the negativity $N(\Phi_p^+)$ are obtained, but also the optimized observable H saturates qCRB (23).

The explanation for such good performance could be the following. The negativity of the state (58) reads $N(\Phi_p^+) = 2\sqrt{p(1-p)}$. Then one gets $p = (1 \pm \sqrt{1-N^2})/2$. Therefore, (58) can be rewritten as

$$|\Phi_N^+\rangle = \frac{1}{\sqrt{2}}(c_1|00\rangle + c_2|11\rangle), \quad (59)$$

where $c_{1,2} = \sqrt{1 \pm \sqrt{1-N^2}}$. Using (D3) one finds an SLD operator L with a spectral decomposition

$$L = \frac{1}{\sqrt{1-N^2}}|l_1\rangle\langle l_1| - \frac{1}{\sqrt{1-N^2}}|l_2\rangle\langle l_2|$$

$$|l_{1,2}\rangle = \sqrt{\frac{1 \mp N}{2}}|00\rangle \pm \sqrt{\frac{1 \pm N}{2}}|11\rangle$$

with the eigenvectors $|l_i\rangle$ being dependent on N , giving therefore the observable (24) which cannot saturate the qCRB in the whole range of N .

However, as we see in Fig. 2, the bound is saturated, which suggests that our model finds a better observable. Indeed, solving (40) for the state (59) yields the following optimal observable:

$$H_0 = \begin{pmatrix} \frac{t_3}{t_1} & 0 & 0 & \frac{t_2}{t_1} \\ 0 & 2h_{00} - 2h_{03} + \frac{t_4}{t_1} & 2h_{11} + 2ih_{12} - \frac{t_2}{t_1} & 0 \\ 0 & 2h_{11} - 2ih_{12} - \frac{t_2}{t_1} & 2h_{00} + 2h_{03} - \frac{t_3}{t_1} & 0 \\ \frac{t_2}{t_1} & 0 & 0 & -\frac{t_4}{t_1} \end{pmatrix} \quad (60)$$

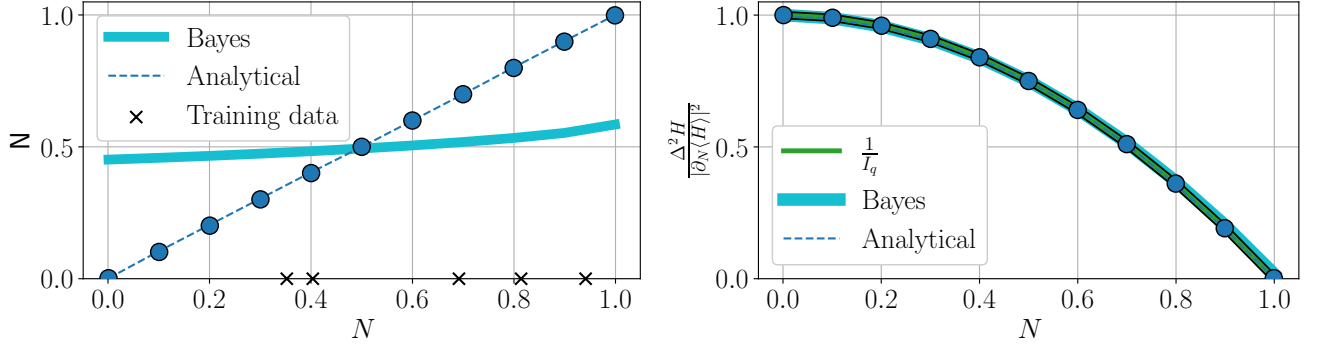


FIG. 2. Left: Predicted \mathcal{N} vs. the true N negativity of the Bell-type state (58); the black crosses indicate the states from the training set. Right: Variance (25) together with the quantum Cramer-Rao bound (23). In both panels, the solid blue line stands for the results obtained via the minimization of the Bayesian MSE (26), and the dashed line indicates the results for the optimal observable (61); in the right panel, the both overlap with qCRB.

where h_{00} , h_{03} , h_{11} and h_{02} are free variables and

$$\begin{aligned} t_1 &= 3k^2\pi^2 + 6k\pi^2 - 12k^2\pi + 12k\pi + 8k^2 - 100k - 16, \\ t_2 &= 3k^2\pi^2 - 12k^2\pi + 6k\pi + 8k^2 - 20k, \\ t_3 &= 24k\pi - 76k - 8, \\ t_4 &= 4k + 8. \end{aligned}$$

If we put a sufficiently small variance weight w_{var} in (16) and (40), which implies $k \rightarrow \infty$, then (60) becomes

$$H_0 = \begin{pmatrix} 0 & 0 & 0 & 1 \\ 0 & 2(h_{00} - h_{03}) & 2(h_{11} + ih_{12}) - 1 & 0 \\ 0 & 2(h_{11} - ih_{12}) - 1 & 2(h_{00} + h_{03}) & 0 \\ 1 & 0 & 0 & 0 \end{pmatrix}. \quad (61)$$

For this observable and the state $|\Phi_N^+\rangle$, one obtains $\langle H_0 \rangle = N$ and $\Delta^2 H_0 = 1 - N^2 = 1/I_q(\Phi_N^+)$.

Therefore, our method finds this or an equivalent observable H giving accurate predictions and saturating qCRB. Thus, one should be careful while analyzing observables obtained via (24) from an SLD operator, as the latter can be not unique. Indeed, with the SLD L being the solution of (21), the uniqueness is guaranteed when ρ_α is strictly positive definite [70]. However, this is not the case as the states (59) are pure. Therefore, more accurately, one should consider all the solutions of (21) and then pick only those which give, by construction (24), an observable independent of the parameter. The whole procedure gets cumbersome, and direct solving of (40) seems to be more preferable for obtaining the global optimal observable.

For the considered task, we also simulated the minimization of the Bayesian MSE (47). In this case, the obtained observable saturates the qCRB (23), but gives inaccurate predictions of the labels. Moreover, if one puts the optimal observable (60) with $k = 1$ into the Bayesian qCRB (30), one gets

$$\Delta_B^2 \alpha = \Delta_p^2 \alpha - I_B = \frac{2\pi^2 - 8\pi + 4}{9\pi^2 - 108} \approx 0.0726799,$$

in agreement with our numerical results.

2. Isotropic states

The next example is dedicated to negativities of the two-qubit isotropic state

$$\rho_q = q |\Phi\rangle\langle\Phi| + \frac{1-q}{4} \mathbb{1}, \quad (62)$$

where $|\Phi\rangle \equiv |\Phi_{1/2}^+\rangle$, the Bell state (58) with $p = 1/2$. Generally, isotropic states are used as a standard noise model. In addition, they are invariant under the local unitary transformations $U \otimes \bar{U}$, where \bar{U} denotes complex conjugation of U . Due to this property the isotropic states can be used as intermediate states in the protocols of entanglement distillation [111].

The negativity of the isotropic state reads

$$N(\rho_q) = \begin{cases} 0, & \text{if } q \leq \frac{1}{3} \\ \frac{3q-1}{2}, & \text{if } q > \frac{1}{3} \end{cases}$$

For $q > 1/3$, we can rewrite (62) as

$$\rho_N = \frac{2N+1}{3} |\Phi\rangle\langle\Phi| + \frac{1-N}{6} \mathbb{1}, \quad (63)$$

for which one can find the spectral decomposition of the SLD operator (21) to be

$$L = \frac{1}{N+1} |l_1\rangle\langle l_1| + \frac{1}{N-1} \sum_{i=2}^4 |l_i\rangle\langle l_i|,$$

$$|l_{1,2}\rangle = \frac{1}{\sqrt{2}}(|00\rangle \pm |11\rangle), \quad |l_3\rangle = |01\rangle, \quad |l_4\rangle = |10\rangle,$$

and qFI is $I_q(\rho_N) = 1/(1-N^2)$. This time, the eigenvectors $|l_i\rangle$ are independent of N , so the optimal observable constructed via (24) is

$$H = |00\rangle\langle 11| + |11\rangle\langle 00| - |01\rangle\langle 01| - |10\rangle\langle 10|. \quad (64)$$

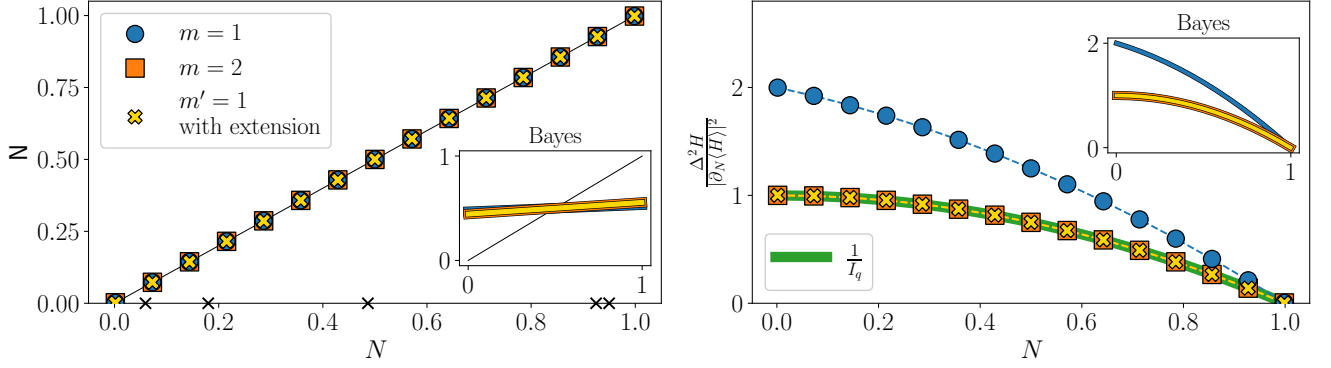


FIG. 3. Left: Predicted N vs. true N negativity of the isotropic state (62) using trained observables of the form (8) with measuring $m \in \{1, 2\}$ qubits. Right: Variance (25) together with cCRB (dashed lines) and qCRB (solid green line). The model was trained on a set $\mathcal{T} = \{\rho_{q_j}, q_j\}_{j=1}^5$ of isotropic states (8) with random $q > 1/3$ with the corresponding negativities indicated as black crosses in the left panel. The yellow crosses in both panels stand for the case of $m' = 1$ measured qubit introduced via the Naimark's extension (7). The insets show the results obtained using the Bayesian approach (26).

On the other hand, solving the equation (40) one can obtain the following optimal observable:

$$H_0 = \frac{1}{(8+k)} \begin{pmatrix} 4 & 0 & 0 & k \\ 0 & 4-k & 0 & 0 \\ 0 & 0 & 4-k & 0 \\ k & 0 & 0 & 4 \end{pmatrix}. \quad (65)$$

For the state ρ_N , this observable gives

$$\langle H_0 \rangle = \frac{4+Nk}{8+k}, \quad \Delta^2 H_0 = \frac{(1-N^2)k^2}{(8+k)^2}.$$

Therefore, as long as k is finite, there will always be a bias in the prediction. This confirms the statement we made at the end of Section IV B. If we assign a small weight to the total variance in (40), i.e., $k \rightarrow \infty$, then this observable coincides with (64).

Interestingly, the observable (64) has two distinct eigenvalues, the unique $x_1 = 1$ and the thrice-degenerate $x_2 = -1$. Moreover, one can verify that this degeneracy for the eigenvalues holds also for (65) for any k . One can find such observable using the procedure (16) by measuring one qubit introduced via the Naimark's extension (7), which we denote $m' = 1$. Indeed, if we look for an optimal observable in the form (8) with measuring one qubit of the state, we could find only an observable with two-dimensional projectors (9). Hence one gets two-fold degenerate eigenvalues.

These eigenvalue degeneracies may be important in solving regression problems. In Fig. 3, we show the negativities of the state (62) predicted by our model with different numbers of measured qubits m . The model was trained on a set $\mathcal{T} = \{\rho_{q_j}, N_j\}_{j=1}^5$, where q_j are uniformly sampled from $(\frac{1}{3}, 1]$, so that the states ρ_{q_j} are always entangled. As we see in Fig. 3, by measuring $m = 1$ or 2 qubits of the isotropic state we are able to find an observable giving accurate predictions

of the negativity. However, with $m = 1$, the variance of the optimized observable is as about twice as large as with $m = 2$, which may be happening due to the eigenvalue degeneracy discussed earlier. Across many runs of our simulations, we obtain an observable with the two-fold degenerate eigenvalues $x_1 = 1$ and $x_2 = -2$. Such an observable may have the form, e.g., $H = (|\Phi\rangle\langle\Phi| + |\psi_1^\perp\rangle\langle\psi_1^\perp|) - 2(|\psi_2^\perp\rangle\langle\psi_2^\perp| + |\psi_3^\perp\rangle\langle\psi_3^\perp|)$, where $|\psi_i^\perp\rangle$ are any vectors orthogonal to $|\Phi\rangle$ and to each other. For this observable and isotropic state ρ_N of the form (63), one can verify that $\langle H \rangle = N$ and $\Delta^2 H = 2 - N - N^2$, which coincides with the blue line in Fig. 3 (right). In contrast, if we measure $m' = 1$ *additional* qubit introduced via the Naimark's extension (7), we obtain an observable giving both accurate predictions and saturating qCRB.

Additionally in the insets of Fig. 3, we plot the results for the observable obtained by means of the Bayesian approach (56). As in the previous cases, the resultant observable does not give accurate label predictions. At the same time, it saturates the quantum Cramer-Rao bounds (23) and (30). For the latter, the observable (65) with $k = 1$ gives

$$\Delta_B^2 \alpha = \Delta_p^2 \alpha - I_B = \frac{2}{27} \approx 0.074,$$

achieved in our numerical experiments for $m = 2$ and $m' = 1$ measured qubit introduced via Naimark's extension.

An extra attention is paid to entangled isotropic states ρ_q with $q > 1/3$, for which one can find an observable giving accurate predictions of the negativity. Unfortunately, there is no such observable if $q \leq 1/3$, as $N = 0$ on this interval. One can use the technique of processing several copies of the state ρ_N , as mentioned in Section II H, with the prediction for N becoming $N = \text{Tr } H \rho_N^{\otimes c}$. In Appendix C 1, we consider the situation case with separable states in the training set.

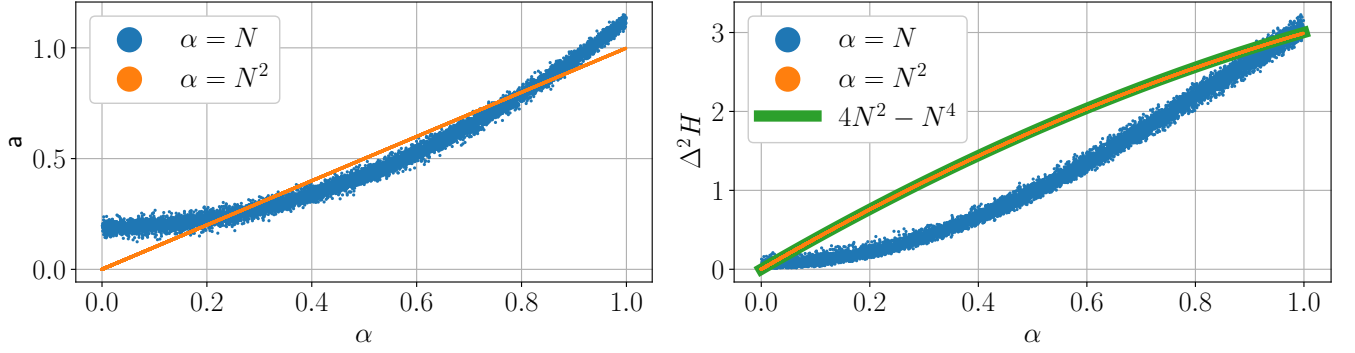


FIG. 4. Left: Predicted negativity N (blue) and the squared negativity N^2 (orange) of 10^4 random pure two-qubit states vs. the corresponding true N and N^2 for $c = 2$ copies. Right: Variance of the trained observable H ; the solid green line indicates the variance of the observables $M_{1,2}$ in (66), which overlaps with the variance of H trained to predict the squared negativity. The models were trained on the sets $\mathcal{T} = \{|\psi_j\rangle^{\otimes 2}, N_j\}_{j=1}^{1000}$ (blue) and $\mathcal{T} = \{|\psi_j\rangle^{\otimes 2}, N_j^2\}_{j=1}^{1000}$ (orange) with random $|\psi_j\rangle$ and evenly distributed N_j .

3. Random pure states

The presented approach aims to assume as little knowledge about the regression problem as possible. In some specific cases, however, one might also try to augment the method with an extra knowledge about the system. As an example, from entanglement theory an upper bound on the *square* of the negativity of an arbitrary *two-qubit* mixed state [112] is known:

$$[N(\rho)]^2 \leq \text{Tr } \rho^{\otimes 2} M_i, \quad i = 1, 2, \quad (66)$$

where $M_1 = 4P_-^{(1)} \otimes I^{(2)}$ and $M_2 = 4I^{(1)} \otimes P_-^{(2)}$. Here $P_-^{(i)}$ denotes the projector onto the antisymmetric subspace of the two copies of the i -th subsystem. Originally in [112] the bound was derived for the square of another entanglement measure, the concurrence [113–115]. However, it is known that for the case of two-qubit mixed states the concurrence is always lower-bounded by the negativity [116]. There is also a similar *lower* bound [117] on the square of concurrence $C(\rho)$ of an arbitrary bipartite state:

$$[C(\rho)]^2 \geq \text{Tr } \rho^{\otimes 2} V_i, \quad i = 1, 2, \quad (67)$$

where $V_1 = 4(P_-^{(1)} - P_+^{(1)}) \otimes P_-^{(2)}$ and $V_2 = 4P_-^{(1)} \otimes (P_-^{(2)} - P_+^{(2)})$, with $P_+^{(i)}$ being the projector onto the symmetric subspace of the two copies of the i -th subsystem.

The bounds (66), (67) have the form of expectation value of a Hermitian operator with respect to *two copies* of a given state fitting our approach well. In addition, for *pure* two-qubit states the bound gives the *exact* value of squared negativity [112] (and also concurrence and negativity coincide for such states [116]). Thus, we can test the performance of our method on randomly generated pure states and check how well it can variationally find the appropriate observable on two copies to obtain the exact value of the squared negativity. For this, we trained

our regression model on a set $\mathcal{T} = \{|\psi_j\rangle^{\otimes 2}, N_j^2\}_{j=1}^{1000}$ consisting of random pure states along with their squared negativities, which are evenly distributed on the interval $[0, 1]$. In our simulations, we used an ansatz of $l = 2$ layers and measured all $m = 4$ qubits as per (8).

The results depicted in Fig. 4 show that the found observable provides very good predictions for the squared negativity and is able to reproduce numerically two-copy observables like M_1 and M_2 defined above. For comparison, we additionally plot the results of the performance of our model trained on the same data set, but without squaring the negativities. For both cases, in Fig. 4 we also plot the variance of the optimized observable $\Delta^2 H$. For either M_1 or M_2 in (66) and two copies of a pure two-qubit state $|\psi_N\rangle$ with negativity N , one can find that $\Delta_{\psi_N}^2 M_{1,2} = 4N^2 - N^4$ which is saturated by H found with our method.

Interestingly, one can obtain these results by measuring $m = 1$ out of $n = 4$ qubits, but only if it is introduced via the Naimark's extension (7). Indeed, both observables $M_{1,2}$ in (66) have only a four-fold degenerate eigenvalue $x_1 = 4$. In the meantime, the observables $V_{1,2}$ in (67) have a three-fold degenerate $x_1 = -4$ and a non-degenerate $x_2 = 4$. If one looks for an optimal observable in the form (4) by measuring $m = 1$ qubit of $\rho_N^{\otimes 2}$, one could obtain only an observable with eight-fold degenerate eigenvalues (excluding the trivial case). This can be resolved by Naimark's extension with $m' = 1$ additional qubit.

4. Random mixed states

Prediction of the negativity of *random mixed* states presents a more challenging problem. To solve it, we train our model on a set $\mathcal{T}_c = \{\rho_j^{\otimes c}, N_j\}_{j=1}^{1000}$, where the states ρ_j are generated such that their negativities N_j are evenly distributed on $[0, 1]$. To parametrize the ob-

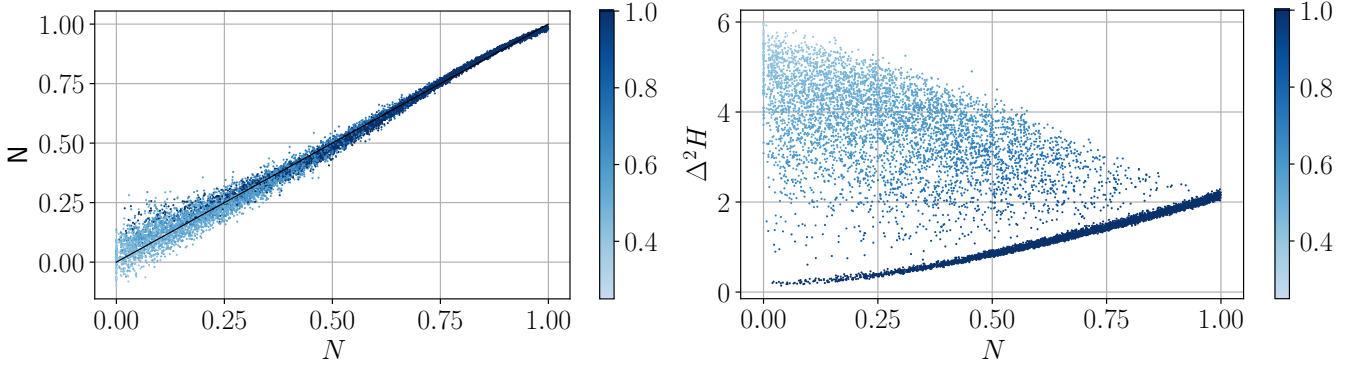


FIG. 5. Left: Predicted negativity N of 10^4 random mixed states vs. the true negativity N for $c = 4$ copies. Right: Variance of the trained observable H . The color of the points indicates the purity of the corresponding states. The model was trained on a set $\mathcal{T} = \{\rho_j^{\otimes 4}, N_j\}_{j=1}^{1000}$ with random ρ_j and N_j evenly distributed on $[0, 1]$.

servable, we used an ansatz of $l = 2$ layers.

In Fig. 5 we show the predictions of the negativity of randomly generated mixed states by considering $c = 4$ copies. Additionally, we indicate the purity $P(\rho) = \text{Tr} \rho^2$ of a given state ρ . As can be seen, for lower negativities the states are generally more mixed, which results both in higher prediction error and variance $\Delta^2 H$ of the optimized observable. Nonetheless, our model performs well even in a difficult case of using a training set of a relatively modest size. However, in this case, our method requires measuring all $m = 2c$ qubits, which results in $|\mathbf{x}| = 2^{2c}$ additional parameters to vary. Still, our model achieves good prediction accuracy without any knowledge about the connection between the data points ρ_j and their labels N_j . For comparison, in Appendix C 2 we also show the results obtained for the same training set, but computed with $c = 1, 2, 3$ copies. As one could expect, the more copies we process, the better results we get. Following the intuition provided by (66), in Appendix C 3 we apply our method for predicting the squared negativities which results in a significant increase of accuracy for $c = 2, 4$, but giving a little advantage for $c = 3$ compared with $c = 2$.

We make two remarks here. First, as mentioned above, while measuring all $m = 8$ qubits of the composite state $\rho^{\otimes 4}$ indeed allows to obtain an observable giving accurate predictions of the negativity, the optimization process is computationally demanding. In Appendix C 5, we train our model with smaller m and discuss the training complexity of this process. However, while our simulations show that $m = 6$ gives predictions and variances one may consider acceptable, each measured qubit may contribute to the accuracy significantly.

Our second remark concerns the size of the training set T . With the exception for predicting the negativity, all the regression tasks we considered in this work required few (up to ten) training states for finding good observables. In Appendix C 6, we train our model for predicting the negativity for different training set sizes T

from 100 to 1000. We observe that the MSE calculated on the testing set approximately scales with this size as $T^{-5/4}$.

C. Predicting transverse field of the Ising Hamiltonian

Another interesting example of application of our approach is prediction of the transverse field h of the Ising Hamiltonian

$$H_h = -J \sum_{i=1}^n (\sigma_z^i \sigma_z^{i+1} + h \sigma_x^i), \quad (68)$$

where σ_x^i, σ_z^i are Pauli operators acting on the i th qubit, and we apply the periodic boundary conditions $\sigma_z^{n+1} \equiv \sigma_z^1$. Thus, given a collection of the ground states $|\psi_h\rangle$ of H_h in the form (1), one wishes to solve (16) finding an observable H such that the expectation $\langle H \rangle_{\psi_h}$ gives a prediction of the transverse field h . In our numerical experiments, we consider $n = 8$ qubits and set $J = 1$.

In Section II D, we mentioned that by adjusting the weights w_{ls} and w_{var} in (16), we can trade-off between the accuracy of the prediction and its variance. It is already shown in Section V A for the case of the amplitude-damping channel, where the model is trained on a deliberately large training set of $T = 500$ entries. Here, we make use of a much more modest set with only $T = 10$ points. We will look for an observable in the form (8) with $m = 4$ and the ansatz of $l = 5$ layers.

In Fig. 6, the results of predicting the transverse field h of (68) with setting $w_{\text{ls}} = 1$ and considering $w_{\text{var}} \in \{1, 10^{-2}, 10^{-4}\}$ are shown. As might be expected, the greater is the weight w_{var} , the less accurate predictions become. However, with $w_{\text{var}} = 1$, one is closer to the qCRB (23).

Note that with $w_{\text{var}} = 10^{-4}$, one gets good results by measuring only $m = 4$ qubits out of $n = 8$ and utilizing an ansatz of $l = 5$ layers. However, in Appendix C 7

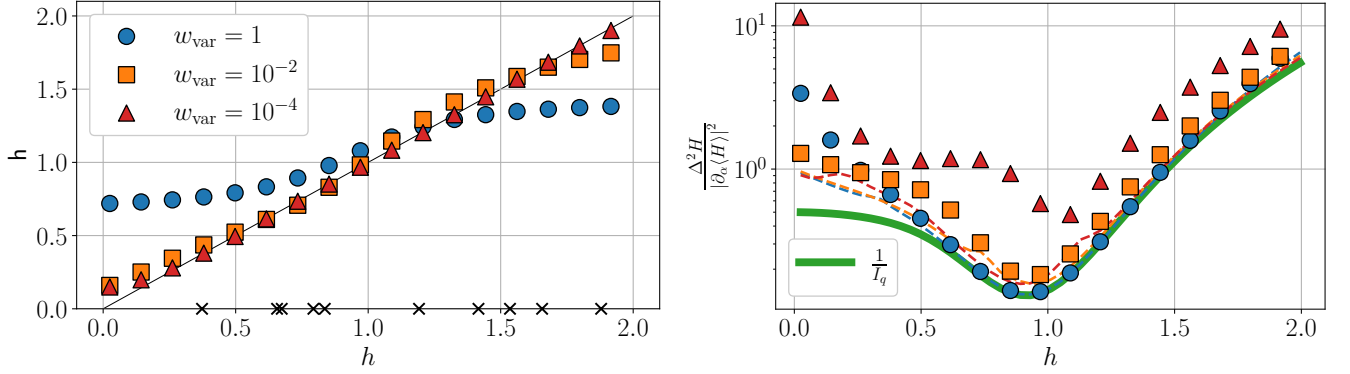


FIG. 6. Left: Predicted \hat{h} vs. true h transverse field of the 8-qubit Ising Hamiltonian (68) for different weights w_{var} in (16); the black crosses on the x -axis indicate the training data. Right: Variance (25) vs. h ; the dashed lines indicate cCRB (19). The observable H is trained on a set $\mathcal{T} = \{|\psi_{h_j}\rangle, h_j\}_{j=1}^{10}$ with $|\psi_j\rangle$ being the ground states of (68), and the fields h_j are generated randomly. In the right panel, the dashed lines of the corresponding colors indicate the achieved cCRB, while the solid green line stands for qCRB (23).

we show that if all $m = 8$ qubits are measured and an ansatz of $l = 2$ layers is used, the even better results are obtained, especially in terms of variance. Additionally in that Appendix, we discuss the training complexity of our method in solving the considered regression task. In short, despite the possible better prediction accuracy and variance due to greater m , such results are harder to achieve since each additional measured qubit exponentially increases the number of trainable parameters (see (8)).

As of the minimization of the Bayesian MSE (26), for this case it is computationally heavy. However, as one would do in practice [100], one can approximate it as a sum of discrete points. If we possess only the data given in the training set and assume the uniform distribution of the labels, we reduce the problem to (16) with equal weights $w_{\text{ls}} = w_{\text{var}} = 1$. As can be seen in Fig. 6, in this case the method gives too much preference to the minimization of the variance, sacrificing the accuracy. This is in line with the results of minimizing the Bayesian MSE for other regression problems considered in this work.

The problem of predicting the transverse field was also solved with simulation of a finite number of measurements μ . Namely, in Appendix C 8, the method is used with an assumption that instead of the exact expectations $\hat{h} = \langle \psi_h | H | \psi_h \rangle$ we get their μ -shot estimates \hat{h} during the training. This of course worsens the results compared to the case of “infinite” μ reported in this section. However, with a moderate number of measurements, a good estimation accuracy is still obtained.

VI. DISCUSSION

In this work, using the optimization routine (16), we solve a regression problem for labeled data points represented by quantum states ρ_α with α being the label.

The prediction \hat{a} of the label α is $\text{Tr } H \rho_\alpha$ with H being a constructed observable.

Our approach assumes no knowledge about the link between the data points and their labels. We applied our method for the cases when $\rho_\alpha = \Phi_\alpha[\rho]$ where α parametrizes a quantum channel Φ_α acting on some fixed input state ρ (see Section V A), α is an entanglement measure of ρ_α (see Section V B), and $\rho_\alpha = |\psi_\alpha\rangle\langle\psi_\alpha|$ with $|\psi_\alpha\rangle$ being the ground state of a parametrized Hamiltonian H_α (see Section V C). Appendix C contains additional numerical results related to various aspects of the proposed method, such as the number of measured qubits m in (8), number of copies c of the labeled state processed as one composite state, and finite number of measurements μ . Additionally in that Appendix, we study the problem of predicting the parameter of the depolarizing channel and the angle of a Pauli rotation.

To assess the performance of our method, we employ quantum metrology techniques. Alongside the prediction accuracy, we also look at the error propagation (13) and Cramer-Rao bounds (23), which together produce (25). For some cases, the proposed method allows finding an observable H such that it saturates qCRB. Additionally, by tuning w_{ls} and w_{var} in (16), one can trade off between prediction accuracy and its variance, as we show in Sections V A and V C.

Interestingly, to solve the most regression problems considered in this work we needed training sets of a few states (up to $T = 10$). The exception was the prediction of the negativity of two-qubit states (see Section V B 4), which required a training set of the size $T = 1000$. In Appendix C 6, we numerically study the dependence of the performance of our method on T for the latter problem. We observe that MSE for the optimized observable calculated on the training set scales as $T^{-5/4}$. This is in line with known upper bounds on generalization error, which typically scale as $T^{-1/2}$ (see, e.g., [81]).

In Appendix C 5 we discuss the training complexity of

our method for solving the regression problem. Namely, we study the dependence of the number of iterations of the BFGS algorithm on the number of measured qubits m when we look for an observable in the form (8). While for each m it takes up to 2000 iterations for the algorithm to converge, the number of calls of the cost function in (16) grows exponentially. Indeed, each increment of m doubles the number of varied eigenvalues in (8). One may try to look for an optimal observable on fewer qubits m , as we did for the problem of predicting the transverse field in Section V C. However, for the problem of predicting the negativity of random states, we observed that increasing m may contribute significantly to both the prediction accuracy and variance.

One possible way of circumventing this issue is taking into account the knowledge about the problem to be solved. Indeed, as is shown in Section V B 3 and Appendix C 3, learning to predict the *squared* negativity gives a significant advantage. Moreover, for pure states, one can obtain nearly perfect accuracy by measuring only $m' = 1$ qubit introduced via the Naimark's extension (7). Additionally, one could construct the variational ansatz $U(\theta)$ such that it preserves certain symmetries (an obvious one in our case is the permutation symmetry on c copies of the labeled state, $\rho_\alpha^{\otimes c}$) [118–120]. Alternatively, to construct an ansatz, one could apply various techniques proposed in the literature [121, 122], including the optimization of the ansatz's structure [123, 124].

Throughout this work we assume that the expectations $\mathbf{a} = \text{Tr } H \rho_\alpha$ can be computed exactly. In a measurement experiment, however, one would obtain a μ -shot estimation $\hat{\mathbf{a}}$ of it. In Appendix C 8, we numerically study the performance of our method with simulating a finite number of measurements μ . As one may expect, larger μ give better performance both in terms of the estimation accuracy and the variance. For an easier regression problem with single-qubit labeled states and simple optimal observable, even a modest number of shots $\mu = 2^6$ allows to achieve good results. In contrast, for a harder problem with eight-qubit states, a rather large number of measurements $\mu = 2^{14}$ does not allow to train the model such that it gives the results close to the case of “infinite” μ . This issue of the shot noise is a common challenge for variational quantum algorithms [125]. To overcome it, a variety of techniques have been proposed, such as clever initialization [125, 126], adaptive tuning of the variance weight in (16) as proposed in [97], exploiting symmetries in the labeled states [74], and adjusting the optimizer's hyperparameters (e.g., learning rate in the Adam algorithm [127]) [128, 129]. We note that in this work we applied the optimization algorithms from the SciPy library [104] “out of the box” with random initializations of the variational parameters.

We studied the proposed method also analytically, assuming a large size of the training set (1). In Section IV, first we obtained an equation for an observable which, under the above-mentioned assumption, solves the minimization problem (16). For several regression problems,

we solved this equation and numerically verified the solutions against the method (16). Furthermore, for optimal observables we derive an upper bound on the total variance, which depends on the ratio $k = w_{\text{ls}}/w_{\text{var}}$ and the range of the label α . Another interesting finding is that the observable obtained with the proposed method cannot be unbiased on the whole range of the label α .

For a large training set size T and $k = 1$, our method (16) reduces to the minimization of the Bayesian MSE (26) if the prior distribution of the labels α is uniform (see Section IV C). When applicable, we numerically compare our method to the Bayesian approach. We find that the observable obtained via this approach gives more biased predictions, as it prefers to minimize the variance. At the same time, in numerical minimization of the Bayesian MSE we obtain observables saturating the Bayesian quantum Cramer-Rao bound (30).

In analytical considerations one might as well take into account finite training set size T , as in (1). In this case the equation for the optimal observable (40) is straightforwardly rewritten to

$$\frac{1}{2} (\tilde{\rho}_f H_0 + H_0 \tilde{\rho}_f) - \frac{k}{T} \sum_{j=1}^T \alpha_j \rho_{\alpha_j} + \frac{(k-1)}{T} \sum_{j=1}^T \text{Tr}(H_0 \rho_{\alpha_j}) \rho_{\alpha_j} = 0, \quad (69)$$

where

$$\tilde{\rho}_f = \frac{1}{T} \sum_{j=1}^T \rho_{\alpha_j} \quad (70)$$

is a finite sum density operator defined in analogy with (41). Eq. (69) could be beneficial in analyzing the generalization error of the presented regression method in application to specific tasks with arbitrarily distributed (possibly sparse) training sets.

As mentioned earlier, the application of our method results in an observable giving generally a biased prediction $\text{Tr } H \rho_\alpha$. This bias can sometimes be mitigated, as we show in Appendix C 4. Alternatively, one can find H such that it acts on $\rho_\alpha^{\otimes c}$, several copies of the labeled state. As we show in Appendices C 1, C 2 and C 9 c, the more copies we process simultaneously, the higher is the prediction accuracy.

In particular, we have observed that the prediction of the negativity of random mixed two-qubit states works better in a multi-copy scenario. The prediction gets more accurate with an increase of the number of copies, as can be seen from comparing results for 1, 2, 3, 4 copies (see Appendix C 2). The possible explanation could be devised from recent results on nonlinear multipartite witnesses [130]. The witnesses of this kind are also suited for a multi-copy scenario. In Appendix G, we adapt the theory to demonstrate that some specific witnesses show better entanglement detection (averaged over random states) with higher number of copies. Although this

is just entanglement detection without estimating any entanglement measure, the inequalities (66) and (67) suggest³ that there might be lower and upper bounds on entanglement measures associated with such witnesses. Also, the higher the number of copies is, the tighter and more accurate these bounds are. As a possible direction of further research it would be interesting to establish connections between entanglement measures and multi-copy witnesses.

Among the trainable parameters in (16) there are eigenvalues of the observable H . Thus, if the labeled states are of n qubits the number of parameters to vary would be exponential. As we mentioned earlier, one may search for an observable H such that it is enough to measure a fewer number of qubits $m < n$ in some cases (see Section II C). This may be advantageous also in the way that if $m = 1$, then one can have the variational circuit U in (9) to be in the form of a QCNN [16, 60] which is known to be immune to barren plateaus [61]. However, the usefulness of such ansätze was recently put under question [131].

In this regard, our work opens new directions for further studies. As such, one can investigate the applicability of QCNNs for regression tasks we consider. In Section V B 2 for the prediction of the negativity of isotropic states (62) of $n = 2$ qubits, we discuss an observable H requiring the measurement of only $m = 1$ qubit and providing the same prediction accuracy as that of an efficient observable with $m = 2$, but with about twice greater variance. It could be interesting to understand for which regression problems there exists an observable H_m of the form (8) requiring a measurement of $m < n$ qubits and providing accurate predictions with $\langle H_m \rangle_{\rho_\alpha} = \langle H_n \rangle_{\rho_\alpha}$, and $\Delta_{\rho_\alpha}^2 H_m = \Delta_{\rho_\alpha}^2 H_n$, presumably also saturating the Cramer-Rao bound. Similar results were recently demonstrated for states that have symmetries, for which one can find observables with the same expectation but generally a lower variance [74].

It would be also interesting to consider predictions of some hard-to-compute quantities. For instance, unlike the qubit-qubit case, for mixed qutrit-qutrit states (and also ones of higher dimensions) there is no effective procedure of computing entanglement measures [132]. This is also true for multipartite quantum states, in which case a relevant question is the calculation of various measures [133–135] of genuine entanglement, i.e., entanglement present in each bipartite cut of a quantum state [136, 137]. In the context of quantum channels, important quantities for transmitting classical and quantum information include channel capacities [138]. The question is how effective the regression method will be in predicting the properties listed above.

VII. ACKNOWLEDGEMENTS

The work was supported in the framework of the Roadmap for Quantum Computing (Contracts No. 868-1.3-15/15-2021 and No. R2163).

³ In fact, the lower bound in (67) is an example of nonlinear witness.

-
- [1] M. Schuld, I. Sinayskiy, and F. Petruccione. An introduction to quantum machine learning. *Contemporary Physics*, 56(2):172–185, 2015.
 - [2] J. Biamonte, P. Wittek, N. Pancotti, P. Rebentrost, N. Wiebe, and S. Lloyd. Quantum machine learning. *Nature*, 549(7671):195–202, 2017.
 - [3] Seth Lloyd and Christian Weedbrook. Quantum generative adversarial learning. *Physical review letters*, 121(4):040502, 2018.
 - [4] M. Schuld and N. Killoran. Quantum machine learning in feature hilbert spaces. *Physical Review Letters*, 122(4):040504, 2019.
 - [5] K. Mitarai, M. Negoro, M. Kitagawa, and K. Fujii. Quantum circuit learning. *Physical Review A*, 98(3):032309, 2018.
 - [6] Adrián Pérez-Salinas, Alba Cervera-Lierta, Elies Gil-Fuster, and José I Latorre. Data re-uploading for a universal quantum classifier. *Quantum*, 4:226, 2020.
 - [7] Adrián Pérez-Salinas, David López-Núñez, Artur García-Sáez, Pol Forn-Díaz, and José I Latorre. One qubit as a universal approximant. *Physical Review A*, 104(1):012405, 2021.
 - [8] Maria Schuld, Ryan Sweke, and Johannes Jakob Meyer. Effect of data encoding on the expressive power of variational quantum-machine-learning models. *Physical Review A*, 103(3):032430, 2021.
 - [9] Takahiro Goto, Quoc Hoan Tran, and Kohei Nakajima. Universal approximation property of quantum machine learning models in quantum-enhanced feature spaces. *Physical Review Letters*, 127(9):090506, 2021.
 - [10] Patrick Rebentrost, Masoud Mohseni, and Seth Lloyd. Quantum support vector machine for big data classification. *Physical review letters*, 113(13):130503, 2014.
 - [11] Daniel K Park, Carsten Blank, and Francesco Petruccione. The theory of the quantum kernel-based binary classifier. *Physics Letters A*, 384(21):126422, 2020.
 - [12] Leonardo Banchi, Jason Pereira, and Stefano Pirandola. Generalization in quantum machine learning: A quantum information standpoint. *PRX Quantum*, 2(4):040321, 2021.
 - [13] Maria Schuld, Ilya Sinayskiy, and Francesco Petruccione. Prediction by linear regression on a quantum computer. *Physical Review A*, 94(2):022342, 2016.
 - [14] Teppei Suzuki and Michio Katouda. Predicting toxicity by quantum machine learning. *Journal of Physics Communications*, 4(12):125012, 2020.
 - [15] Pranath Reddy and Aranya B Bhattacharjee. A hybrid quantum regression model for the prediction of molecular atomization energies. *Machine Learning: Science and Technology*, 2(2):025019, 2021.
 - [16] Lento Nagano, Alexander Miessen, Tamiya Onodera, Ivano Tavernelli, Francesco Tacchino, and Koji Terashi. Quantum data learning for quantum simulations in high-energy physics. *Physical Review Research*, 5(4):043250, 2023.
 - [17] Vojtěch Havlíček, Antonio D Córcoles, Kristan Temme, Aram W Harrow, Abhinav Kandala, Jerry M Chow, and Jay M Gambetta. Supervised learning with quantum-enhanced feature spaces. *Nature*, 567(7747):209–212, 2019.
 - [18] Carsten Blank, Daniel K Park, June-Koo Kevin Rhee, and Francesco Petruccione. Quantum classifier with tailored quantum kernel. *npj Quantum Information*, 6(1):41, 2020.
 - [19] Sofiene Jerbi, Lukas J Fiderer, Hendrik Poulsen Nautrup, Jonas M Kübler, Hans J Briegel, and Vedran Dunjko. Quantum machine learning beyond kernel methods. *Nature Communications*, 14(1):517, 2023.
 - [20] Marcello Benedetti, Erika Lloyd, Stefan Sack, and Mattia Fiorentini. Parameterized quantum circuits as machine learning models. *Quantum Science and Technology*, 4(4):043001, 2019.
 - [21] M. Schuld, A. Bocharov, K. M Svore, and N. Wiebe. Circuit-centric quantum classifiers. *Physical Review A*, 101(3):032308, 2020.
 - [22] M. Cerezo et al. Variational quantum algorithms. *Nature Reviews Physics*, 3(9):625–644, 2021.
 - [23] Jacob Biamonte. Universal variational quantum computation. *Physical Review A*, 103(3):L030401, 2021.
 - [24] Alberto Peruzzo, Jarrod McClean, Peter Shadbolt, Man-Hong Yung, Xiao-Qi Zhou, Peter J Love, Alán Aspuru-Guzik, and Jeremy L O’Brien. A variational eigenvalue solver on a photonic quantum processor. *Nature Communications*, 5:4213, 2014.
 - [25] A. Kandala, A. Mezzacapo, K. Temme, M. Takita, M. Brink, J. M. Chow, and J. M. Gambetta. Hardware-efficient variational quantum eigensolver for small molecules and quantum magnets. *Nature*, 549:242, Sep 2017.
 - [26] A. Kardashin, A. Pervishko, J. Biamonte, and D. Yudin. Numerical hardware-efficient variational quantum simulation of a soliton solution. *Physical Review A*, 104:L020402, Aug 2021.
 - [27] Xiaosi Xu, Jinzhao Sun, Suguru Endo, Ying Li, Simon C Benjamin, and Xiao Yuan. Variational algorithms for linear algebra. *Science Bulletin*, 66(21):2181–2188, 2021.
 - [28] Carlos Bravo-Prieto, Ryan LaRose, Marco Cerezo, Yigit Subasi, Lukasz Cincio, and Patrick J Coles. Variational quantum linear solver. *Quantum*, 7:1188, 2023.
 - [29] R. LaRose, A. Tikku, É. O’Neel-Judy, L. Cincio, and P. J Coles. Variational quantum state diagonalization. *npj Quantum Information*, 5(1):1–10, 2019.
 - [30] Benjamin Commeau, Marco Cerezo, Zoë Holmes, Lukasz Cincio, Patrick J Coles, and Andrew Sornborger. Variational hamiltonian diagonalization for dynamical quantum simulation. *arXiv preprint arXiv:2009.02559*, 2020.
 - [31] Cristina Cirstoiu, Zoe Holmes, Joseph Iosue, Lukasz Cincio, Patrick J Coles, and Andrew Sornborger. Variational fast forwarding for quantum simulation beyond the coherence time. *npj Quantum Information*, 6(1):82, 2020.
 - [32] Jinfeng Zeng, Chenfeng Cao, Chao Zhang, Pengxiang Xu, and Bei Zeng. A variational quantum algorithm for hamiltonian diagonalization. *Quantum Science and Technology*, 6(4):045009, 2021.
 - [33] Bálint Koczor, Suguru Endo, Tyson Jones, Yuichiro Matsuzaki, and Simon C Benjamin. Variational-state quantum metrology. *New Journal of Physics*,

- 22(8):083038, 2020.
- [34] Johannes Jakob Meyer, Johannes Borregaard, and Jens Eisert. A variational toolbox for quantum multi-parameter estimation. *npj Quantum Information*, 7(1):89, 2021.
 - [35] Raphael Kaubruegger, Denis V Vasilyev, Marius Schulte, Klemens Hammerer, and Peter Zoller. Quantum variational optimization of ramsey interferometry and atomic clocks. *Physical review X*, 11(4):041045, 2021.
 - [36] Uwe Dorner, Rafal Demkowicz-Dobrzanski, Brian J Smith, Jeff S Lundeen, Wojciech Wasilewski, Konrad Banaszek, and Ian A Walmsley. Optimal quantum phase estimation. *Physical review letters*, 102(4):040403, 2009.
 - [37] Stefano Pirandola, B Roy Bardhan, Tobias Gehring, Christian Weedbrook, and Seth Lloyd. Advances in photonic quantum sensing. *Nature Photonics*, 12(12):724–733, 2018.
 - [38] Senrui Chen, Sisi Zhou, Alireza Seif, and Liang Jiang. Quantum advantages for pauli channel estimation. *Physical Review A*, 105(3):032435, 2022.
 - [39] Juan Carrasquilla and Roger G Melko. Machine learning phases of matter. *Nature Physics*, 13(5):431–434, 2017.
 - [40] Evert PL Van Nieuwenburg, Ye-Hua Liu, and Sebastian D Huber. Learning phase transitions by confusion. *Nature Physics*, 13(5):435–439, 2017.
 - [41] A. V. Uvarov, A. S. Kardashin, and J. D Biamonte. Machine learning phase transitions with a quantum processor. *Physical Review A*, 102(1):012415, 2020.
 - [42] Nana Liu and Patrick Rebentrost. Quantum machine learning for quantum anomaly detection. *Physical Review A*, 97(4):042315, 2018.
 - [43] Jin-Min Liang, Shu-Qian Shen, Ming Li, and Lei Li. Quantum anomaly detection with density estimation and multivariate gaussian distribution. *Physical Review A*, 99(5):052310, 2019.
 - [44] A. Patterson, H. Chen, L. Wossnig, S. Severini, D. Browne, and I. Rungger. Quantum state discrimination using noisy quantum neural networks. *Physical Review Research*, 3(1):013063, 2021.
 - [45] H. Chen, L. Wossnig, S. Severini, H. Neven, and M. Mohseni. Universal discriminative quantum neural networks. *Quantum Machine Intelligence*, 3(1):1–11, 2021.
 - [46] P.-H. Qiu, X.-G. Chen, and Y.-W. Shi. Solving quantum channel discrimination problem with quantum networks and quantum neural networks. *IEEE Access*, 7:50214–50222, 2019.
 - [47] AS Kardashin, AV Vlasova, AA Pervishko, D Yudin, and JD Biamonte. Quantum-machine-learning channel discrimination. *Physical Review A*, 106(3):032409, 2022.
 - [48] Akash Kundu and Jarosław Adam Mischak. Variational certification of quantum devices. *Quantum Science and Technology*, 7(4):045017, 2022.
 - [49] Joe Gibbs, Zoe Holmes, Matthias C Caro, Nicholas Ezzell, Hsin-Yuan Huang, Lukasz Cincio, Andrew T Sornborger, and Patrick J Coles. Dynamical simulation via quantum machine learning with provable generalization. *Physical Review Research*, 6(1):013241, 2024.
 - [50] Peng-Hui Qiu, Xiao-Guang Chen, and Yi-Wei Shi. Detecting entanglement with deep quantum neural networks. *IEEE Access*, 7:94310–94320, 2019.
 - [51] Claudio Sanavio, Edoardo Tignone, and Elisa Ercolessi. Entanglement classification via witness operators generated by support vector machine. *The European Physical Journal Plus*, 138(10):936, 2023.
 - [52] Lukasz Cincio, Yiğit Subaşı, Andrew T Sornborger, and Patrick J Coles. Learning the quantum algorithm for state overlap. *New Journal of Physics*, 20(11):113022, 2018.
 - [53] Peter D Johnson, Jonathan Romero, Jonathan Olson, Yudong Cao, and Alán Aspuru-Guzik. Qvector: an algorithm for device-tailored quantum error correction. *arXiv preprint arXiv:1711.02249*, 2017.
 - [54] Jan Roik, Karol Bartkiewicz, Antonín Černoch, and Karel Lemr. Entanglement quantification from collective measurements processed by machine learning. *Physics Letters A*, 446:128270, 2022.
 - [55] Kun Wang, Zhixin Song, Xuanqiang Zhao, Zihe Wang, and Xin Wang. Detecting and quantifying entanglement on near-term quantum devices. *npj Quantum Information*, 8(1):52, 2022.
 - [56] Jing Liu, Haidong Yuan, Xiao-Ming Lu, and Xiaoguang Wang. Quantum fisher information matrix and multiparameter estimation. *Journal of Physics A: Mathematical and Theoretical*, 53(2):023001, 2020.
 - [57] Johannes Jakob Meyer. Fisher information in noisy intermediate-scale quantum applications. *Quantum*, 5:539, 2021.
 - [58] Jasmininder S Sidhu and Pieter Kok. Geometric perspective on quantum parameter estimation. *AVS Quantum Science*, 2(1), 2020.
 - [59] Soorya Rethinasamy, Rochisha Agarwal, Kunal Sharma, and Mark M Wilde. Estimating distinguishability measures on quantum computers. *Physical Review A*, 108(1):012409, 2023.
 - [60] Iris Cong, Soonwon Choi, and Mikhail D Lukin. Quantum convolutional neural networks. *Nature Physics*, 15(12):1273–1278, 2019.
 - [61] Arthur Pesah, Marco Cerezo, Samson Wang, Tyler Volkoff, Andrew T Sornborger, and Patrick J Coles. Absence of barren plateaus in quantum convolutional neural networks. *Physical Review X*, 11(4):041011, 2021.
 - [62] Nathan Shettell, Elham Kashefi, and Damian Markham. Cryptographic approach to quantum metrology. *Physical Review A*, 105(1):L010401, 2022.
 - [63] Christopher King. The capacity of the quantum depolarizing channel. *IEEE Transactions on Information Theory*, 49(1):221–229, 2003.
 - [64] Nathan Shettell. Quantum information techniques for quantum metrology. *arXiv preprint arXiv:2201.01523*, 2022.
 - [65] Luca Pezze, Augusto Smerzi, Markus K Oberthaler, Roman Schmied, and Philipp Treutlein. Quantum metrology with nonclassical states of atomic ensembles. *Reviews of Modern Physics*, 90(3):035005, 2018.
 - [66] Géza Tóth and Iagoba Apellaniz. Quantum metrology from a quantum information science perspective. *Journal of Physics A: Mathematical and Theoretical*, 47(42):424006, 2014.
 - [67] Rafał Demkowicz-Dobrzański, Wojciech Górecki, and Mădălin Guță. Multi-parameter estimation beyond quantum fisher information. *Journal of Physics A: Mathematical and Theoretical*, 53(36):363001, 2020.
 - [68] Luca Pezze and Augusto Smerzi. Quantum theory of phase estimation. *arXiv preprint arXiv:1411.5164*, 2014.

- [69] F. Chapeau-Blondeau. Optimized probing states for qubit phase estimation with general quantum noise. *Physical Review A*, 91:052310, 2015.
- [70] S. Personick. Application of quantum estimation theory to analog communication over quantum channels. *IEEE Transactions on Information Theory*, 17(3):240–246, 1971.
- [71] Yan Li, Luca Pezzè, Manuel Gessner, Zhihong Ren, Weidong Li, and Augusto Smerzi. Frequentist and bayesian quantum phase estimation. *Entropy*, 20(9):628, 2018.
- [72] Ruvi Lecamwasam, Syed Assad, Joseph J Hope, Ping Koy Lam, Jayne Thompson, and Mile Gu. Relative entropy of coherence quantifies performance in bayesian metrology. *PRX Quantum*, 5(3):030303, 2024.
- [73] Nathan Shettell and Damian Markham. Quantum metrology with delegated tasks. *Physical Review A*, 106(5):052427, 2022.
- [74] Da-Jian Zhang and DM Tong. Inferring physical properties of symmetric states from the fewest copies. *Physical Review Letters*, 133(4):040202, 2024.
- [75] C Huerta Alderete, Max Hunter Gordon, Frédéric Sauvage, Akira Sone, Andrew T Sornborger, Patrick J Coles, and Marco Cerezo. Inference-based quantum sensing. *Physical Review Letters*, 129(19):190501, 2022.
- [76] Yadong Wu, Juan Yao, Pengfei Zhang, and Hui Zhai. Expressivity of quantum neural networks. *Physical Review Research*, 3(3):L032049, 2021.
- [77] Zoë Holmes, Nolan J Coble, Andrew T Sornborger, and Yiğit Subaşı. Nonlinear transformations in quantum computation. *Physical Review Research*, 5(1):013105, 2023.
- [78] Leonardo Banchi, Jason Luke Pereira, Sharu Theresa Jose, and Osvaldo Simeone. Statistical complexity of quantum learning. *Advanced Quantum Technologies*, page 2300311, 2023.
- [79] Hsin-Yuan Huang, Michael Broughton, Masoud Mohseni, Ryan Babbush, Sergio Boixo, Hartmut Neven, and Jarrod R McClean. Power of data in quantum machine learning. *Nature communications*, 12(1):2631, 2021.
- [80] Hsin-Yuan Huang, Richard Kueng, and John Preskill. Information-theoretic bounds on quantum advantage in machine learning. *Physical Review Letters*, 126(19):190505, 2021.
- [81] Matthias C Caro, Hsin-Yuan Huang, Marco Cerezo, Kunal Sharma, Andrew Sornborger, Lukasz Cincio, and Patrick J Coles. Generalization in quantum machine learning from few training data. *Nature communications*, 13(1):4919, 2022.
- [82] Matthias C Caro, Elies Gil-Fuster, Johannes Jakob Meyer, Jens Eisert, and Ryan Sweke. Encoding-dependent generalization bounds for parametrized quantum circuits. *Quantum*, 5:582, 2021.
- [83] Matthias C Caro, Tom Gur, Cambyse Rouzé, Daniel Stilck Franca, and Sathyawageeswar Subramanian. Information-theoretic generalization bounds for learning from quantum data. In *The Thirty Seventh Annual Conference on Learning Theory*, pages 775–839. PMLR, 2024.
- [84] Scott Aaronson. Shadow tomography of quantum states. In *Proceedings of the 50th annual ACM SIGACT symposium on theory of computing*, pages 325–338, 2018.
- [85] Costin Bădescu and Ryan O’Donnell. Improved quantum data analysis. In *Proceedings of the 53rd Annual ACM SIGACT Symposium on Theory of Computing*, pages 1398–1411, 2021.
- [86] Hsin-Yuan Huang, Michael Broughton, Jordan Cotler, Sitan Chen, Jerry Li, Masoud Mohseni, Hartmut Neven, Ryan Babbush, Richard Kueng, John Preskill, et al. Quantum advantage in learning from experiments. *Science*, 376(6598):1182–1186, 2022.
- [87] Marco Fanizza, Yihui Quek, and Matteo Rosati. Learning quantum processes without input control. *PRX Quantum*, 5(2):020367, 2024.
- [88] Hsin-Yuan Huang, Richard Kueng, and John Preskill. Predicting many properties of a quantum system from very few measurements. *Nature Physics*, 16(10):1050–1057, 2020.
- [89] Haimeng Zhao, Laura Lewis, Ishaan Kannan, Yihui Quek, Hsin-Yuan Huang, and Matthias C Caro. Learning quantum states and unitaries of bounded gate complexity. *PRX Quantum*, 5(4):040306, 2024.
- [90] Hsin-Yuan Huang, Sitan Chen, and John Preskill. Learning to predict arbitrary quantum processes. *PRX Quantum*, 4(4):040337, 2023.
- [91] Andreas Elben, Steven T Flammia, Hsin-Yuan Huang, Richard Kueng, John Preskill, Benoît Vermersch, and Peter Zoller. The randomized measurement toolbox. *Nature Reviews Physics*, 5(1):9–24, 2023.
- [92] Hsin-Yuan Huang, Richard Kueng, Giacomo Torlai, Victor V Albert, and John Preskill. Provably efficient machine learning for quantum many-body problems. *Science*, 377(6613):eabk3333, 2022.
- [93] Sofiene Jerbi, Casper Gyurik, Simon C Marshall, Riccardo Molteni, and Vedran Dunjko. Shadows of quantum machine learning. *Nature Communications*, 15(1):5676, 2024.
- [94] Casper Gyurik, Riccardo Molteni, and Vedran Dunjko. Limitations of measure-first protocols in quantum machine learning. *arXiv preprint arXiv:2311.12618*, 2023.
- [95] Marco Cerezo, Guillaume Verdon, Hsin-Yuan Huang, Lukasz Cincio, and Patrick J Coles. Challenges and opportunities in quantum machine learning. *Nature Computational Science*, 2(9):567–576, 2022.
- [96] Valentin Gebhart, Raffaele Santagati, Antonio Andrea Gentile, Erik M Gauger, David Craig, Natalia Ares, Leonardo Banchi, Florian Marquardt, Luca Pezzè, and Cristian Bonato. Learning quantum systems. *Nature Reviews Physics*, 5(3):141–156, 2023.
- [97] David A. Kreplin and Marco Roth. Reduction of finite sampling noise in quantum neural networks. *Quantum*, 8:1385, 2024.
- [98] Raphael Kaubruegger, Athreya Shankar, Denis V Vasiliev, and Peter Zoller. Optimal and variational multi-parameter quantum metrology and vector-field sensing. *PRX Quantum*, 4(2):020333, 2023.
- [99] Tyler G Thurtell and Akimasa Miyake. Optimizing one-axis twists for variational bayesian quantum metrology. *Physical Review Research*, 6(2):023179, 2024.
- [100] Christian D Marciniak, Thomas Feldker, Ivan Pogorelov, Raphael Kaubruegger, Denis V Vasiliev, Rick van Bijnen, Philipp Schindler, Peter Zoller, Rainer Blatt, and Thomas Monz. Optimal metrology with programmable quantum sensors. *Nature*, 603(7902):604–609, 2022.

- [101] Marco Cerezo, Akira Sone, Jacob L Beckey, and Patrick J Coles. Sub-quantum fisher information. *Quantum Science and Technology*, 6(3):035008, 2021.
- [102] A. Holevo. *Quantum Systems, Channels, Information: A Mathematical Introduction*. de Gruyter & Co, Berlin, Boston, 2012.
- [103] Hayashi M. *Quantum Information Theory. Mathematical Foundation*. Springer Berlin, Heidelberg, 2017.
- [104] Pauli Virtanen, Ralf Gommers, Travis E Oliphant, Matt Haberland, Tyler Reddy, David Cournapeau, Evgeni Burovski, Pearu Peterson, Warren Weckesser, Jonathan Bright, et al. SciPy 1.0: Fundamental Algorithms for Scientific Computing in Python. *Nature Methods*, 17:261–272, 2020.
- [105] J Robert Johansson, Paul D Nation, and Franco Nori. Qutip: An open-source python framework for the dynamics of open quantum systems. *Computer physics communications*, 183(8):1760–1772, 2012.
- [106] J.R. Johansson, P.D. Nation, and Franco Nori. Qutip 2: A python framework for the dynamics of open quantum systems. *Computer Physics Communications*, 184(4):1234–1240, 2013.
- [107] V. Vedral, M. B. Plenio, M. A. Rippin, and P. L. Knight. Quantifying entanglement. *Phys. Rev. Lett.*, 78:2275–2279, Mar 1997.
- [108] Ryszard Horodecki, Paweł Horodecki, Michał Horodecki, and Karol Horodecki. Quantum entanglement. *Rev. Mod. Phys.*, 81:865–942, Jun 2009.
- [109] Otfried Gühne and Géza Tóth. Entanglement detection. *Physics Reports*, 474(1):1–75, 2009.
- [110] C. Eltschka and J. Siewert. Quantifying entanglement resources. *Journal of Physics A: Mathematical and Theoretical*, 47:424005, 2014.
- [111] Michał Horodecki and Paweł Horodecki. Reduction criterion of separability and limits for a class of distillation protocols. *Phys. Rev. A*, 59:4206–4216, Jun 1999.
- [112] Cheng-Jie Zhang, Yan-Xiao Gong, Yong-Sheng Zhang, and Guang-Can Guo. Observable estimation of entanglement for arbitrary finite-dimensional mixed states. *Phys. Rev. A*, 78:042308, Oct 2008.
- [113] Charles H. Bennett, David P. DiVincenzo, John A. Smolin, and William K. Wootters. Mixed-state entanglement and quantum error correction. *Phys. Rev. A*, 54:3824–3851, Nov 1996.
- [114] William K. Wootters. Entanglement of formation of an arbitrary state of two qubits. *Phys. Rev. Lett.*, 80:2245–2248, Mar 1998.
- [115] Florian Mintert, Marek Kuś, and Andreas Buchleitner. Concurrence of mixed bipartite quantum states in arbitrary dimensions. *Phys. Rev. Lett.*, 92:167902, Apr 2004.
- [116] Christopher Eltschka, Géza Tóth, and Jens Siewert. Partial transposition as a direct link between concurrence and negativity. *Phys. Rev. A*, 91:032327, Mar 2015.
- [117] Florian Mintert and Andreas Buchleitner. Observable entanglement measure for mixed quantum states. *Phys. Rev. Lett.*, 98:140505, Apr 2007.
- [118] Martín Larocca, Frédéric Sauvage, Faris M Sbahi, Guillaume Verdon, Patrick J Coles, and Marco Cerezo. Group-invariant quantum machine learning. *PRX Quantum*, 3(3):030341, 2022.
- [119] Johannes Jakob Meyer, Marian Mularski, Elies Gil-Fuster, Antonio Anna Mele, Francesco Arzani, Alissa Wilms, and Jens Eisert. Exploiting symmetry in variational quantum machine learning. *PRX Quantum*, 4(1):010328, 2023.
- [120] Quynh T Nguyen, Louis Schatzki, Paolo Braccia, Michael Ragone, Patrick J Coles, Frederic Sauvage, Martin Larocca, and Marco Cerezo. Theory for equivariant quantum neural networks. *PRX Quantum*, 5(2):020328, 2024.
- [121] Zidu Liu, Pei-Xin Shen, Weikang Li, Lu-Ming Duan, and Dong-Ling Deng. Quantum capsule networks. *Quantum Science and Technology*, 8(1):015016, 2022.
- [122] Raoul Heese, Patricia Bickert, and Astrid Elisa Niederle. Representation of binary classification trees with binary features by quantum circuits. *Quantum*, 6:676, 2022.
- [123] Zhide Lu, Pei-Xin Shen, and Dong-Ling Deng. Markovian quantum neuroevolution for machine learning. *Physical Review Applied*, 16(4):044039, 2021.
- [124] Harper R Grimsley, Sophia E Economou, Edwin Barnes, and Nicholas J Mayhall. An adaptive variational algorithm for exact molecular simulations on a quantum computer. *Nature communications*, 10(1):3007, 2019.
- [125] Giuseppe Scirra, Nikita Astrakhantsev, Sebastiano Pilati, and Guglielmo Mazzola. Challenges of variational quantum optimization with measurement shot noise. *Physical Review A*, 109(3):032408, 2024.
- [126] Harper R Grimsley, George S Barron, Edwin Barnes, Sophia E Economou, and Nicholas J Mayhall. Adaptive, problem-tailored variational quantum eigensolver mitigates rough parameter landscapes and barren plateaus. *npj Quantum Information*, 9(1):19, 2023.
- [127] Diederik P Kingma. Adam: A method for stochastic optimization. *arXiv preprint arXiv:1412.6980*, 2014.
- [128] Kevin J Sung, Jiahao Yao, Matthew P Harrigan, Nicholas C Rubin, Zhang Jiang, Lin Lin, Ryan Babush, and Jarrod R McClean. Using models to improve optimizers for variational quantum algorithms. *Quantum Science and Technology*, 5(4):044008, 2020.
- [129] Xavier Bonet-Monroig, Hao Wang, Diederick Vermetten, Bruno Senjean, Charles Moussa, Thomas Bäck, Vedran Dunjko, and Thomas E O’Brien. Performance comparison of optimization methods on variational quantum algorithms. *Physical Review A*, 107(3):032407, 2023.
- [130] Albert Rico and Felix Huber. Entanglement detection with trace polynomials. *Phys. Rev. Lett.*, 132:070202, Feb 2024.
- [131] Pablo Bermejo, Paolo Braccia, Manuel S Rudolph, Zoë Holmes, Lukasz Cincio, and M Cerezo. Quantum convolutional neural networks are (effectively) classically simulable. *arXiv preprint arXiv:2408.12739*, 2024.
- [132] Y. Huang. Computing quantum discord is np-complete. *New Journal of Physics*, 16:033027, 2014.
- [133] Aditi Sen(De) and Ujjwal Sen. Channel capacities versus entanglement measures in multiparty quantum states. *Phys. Rev. A*, 81:012308, Jan 2010.
- [134] Yue Dai, Yuli Dong, Zhenyu Xu, Wenlong You, Chengjie Zhang, and Otfried Gühne. Experimentally accessible lower bounds for genuine multipartite entanglement and coherence measures. *Phys. Rev. Appl.*, 13:054022, May 2020.
- [135] K V Antipin. Construction of genuinely entangled subspaces and the associated bounds on entanglement measures for mixed states. *Journal of Physics A: Mathematical*

- ical and Theoretical*, 54(50):505303, nov 2021.
- [136] George Svetlichny. Distinguishing three-body from two-body nonseparability by a bell-type inequality. *Phys. Rev. D*, 35:3066–3069, May 1987.
 - [137] W. Dür, G. Vidal, and J. I. Cirac. Three qubits can be entangled in two inequivalent ways. *Phys. Rev. A*, 62:062314, Nov 2000.
 - [138] Mark M Wilde. From classical to quantum shannon theory. *arXiv preprint arXiv:1106.1445*, 2011.
 - [139] Ernesto Campos, Daniil Rabinovich, Vishwanathan Akshay, and J Biamonte. Training saturation in layerwise quantum approximate optimization. *Physical Review A*, 104(3):L030401, 2021.
 - [140] Andrea Skolik, Jarrod R McClean, Masoud Mohseni, Patrick Van Der Smagt, and Martin Leib. Layerwise learning for quantum neural networks. *Quantum Machine Intelligence*, 3:1–11, 2021.
 - [141] Tak Hur, Leeseok Kim, and Daniel K Park. Quantum convolutional neural network for classical data classification. *Quantum Machine Intelligence*, 4(1):3, 2022.
 - [142] Pauli Virtanen, Ralf Gommers, Travis E Oliphant, Matt Haberland, Tyler Reddy, David Cournapeau, Evgeni Burovski, Pearu Peterson, Warren Weckesser, Jonathan Bright, et al. Scipy 1.0: fundamental algorithms for scientific computing in python. *Nature methods*, 17(3):261–272, 2020.
 - [143] Marco G Genoni, Paolo Giorda, and Matteo GA Paris. Optimal estimation of entanglement. *Physical Review A*, 78(3):032303, 2008.
 - [144] Jing Liu, Jie Chen, Xiao-Xing Jing, and Xiaoguang Wang. Quantum fisher information and symmetric logarithmic derivative via anti-commutators. *Journal of Physics A: Mathematical and Theoretical*, 49(27):275302, 2016.
 - [145] Leonid Gurvits. Classical deterministic complexity of edmonds’ problem and quantum entanglement. In *Proceedings of the Thirty-Fifth Annual ACM Symposium on Theory of Computing*, STOC ’03, page 10–19, New York, NY, USA, 2003. Association for Computing Machinery.
 - [146] Charles H. Bennett, Herbert J. Bernstein, Sandu Popescu, and Benjamin Schumacher. Concentrating partial entanglement by local operations. *Phys. Rev. A*, 53:2046–2052, Apr 1996.
 - [147] Michał Horodecki, Paweł Horodecki, and Ryszard Horodecki. General teleportation channel, singlet fraction, and quasidistillation. *Phys. Rev. A*, 60:1888–1898, Sep 1999.
 - [148] Luca Pezzé and Augusto Smerzi. Entanglement, nonlinear dynamics, and the heisenberg limit. *Phys. Rev. Lett.*, 102:100401, Mar 2009.
 - [149] A. Peres. Separability criterion for density matrices. *Physical Review Letters*, 77:1413, 1996.
 - [150] K. Życzkowski, P. Horodecki, A. Sanpera, and M. Lewenstein. Volume of the set of separable states. *Physical Review A*, 58:883, 1998.
 - [151] G. Vidal and R. F. Werner. Computable measure of entanglement. *Physical Review A*, 65:032314, 2002.
 - [152] M. Horodecki, P. Horodecki, and R. Horodecki. Separability of mixed states: necessary and sufficient conditions. *Physics Letters A*, 223:1, 1996.
 - [153] S. Lee, D.-P. Chi, S.-D. Oh, and J. Kim. Convex-roof extended negativity as an entanglement measure for bipartite quantum systems. *Physical Review A*, 68:062304, 2003.
 - [154] Jens Eisert. Entanglement in quantum information theory. *arXiv preprint arXiv:quant-ph/0610253*, 2006.
 - [155] Aram W. Harrow. The church of the symmetric subspace. *arXiv preprint arXiv:quant-ph/1308.6595*, 2013.

Appendix A: Hardware-efficient ansatz

In this work, we represent the parametrized quantum circuit $U(\boldsymbol{\theta})$ by the so-called hardware-efficient ansatz (HEA) [25, 26]. The idea behind such ansätze is in alternation between single-qubit rotations and operations capable of introducing entanglement into the system. In our implementation, an example of which is shown in Fig. 7, the ansatz consists of several layers of parametrized gates. Each layer contains an array of x - and z - of Pauli rotations acting on individual qubits, followed by a cascade of controlled y -rotations which produce entanglement. In our ansatz, we also have the “zeroth layer” containing no entangling gates. Therefore, the total number of the parameters in an n -qubit l -layered ansatz is $3ln - l + 2n$.

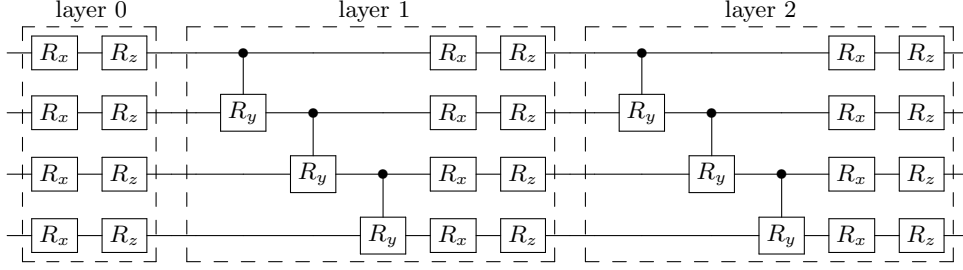


FIG. 7. Example of a two-layered hardware-efficient ansatz for four qubits. Here, $R_i(\theta) = e^{-i\theta\sigma_i}$, and the rotation angles θ are omitted in the circuit.

As one may notice, all gates in the ansatz are parametrized. This could be helpful for applying optimization techniques such as layerwise training [139, 140]. That is, having trained an ansatz of l layers, one adds another layer with the parameters initialized to zeros, and continues the training of the resultant $(l + 1)$ -layered ansatz. Similarly, in our setting one could first train the ansatz for c copies of a state ρ_α . Then add another copy and, correspondingly, add new gates to the ansatz with the parameters set to zeros, and continue the optimization for $\rho_\alpha^{\otimes(c+1)}$.

In Section II C, we discussed measurements of m out of n qubits of the transformed state $U(\boldsymbol{\theta})\rho_\alpha U^\dagger(\boldsymbol{\theta})$ for reduction of the number of parameters \boldsymbol{x} in (8) from 2^n to 2^m . For such a purpose, one can represent $U(\boldsymbol{\theta})$ in the form of a so-called quantum convolutional neural network (QCNN) [16, 60, 141]. A QCNN can be viewed as a sequence of convolutional layers, which usually consist of two-qubit gates acting on neighboring qubits, and pooling layers, in which one traces out a subset (usually, a half) of qubits. At the end of the QCNN, one measures an observable of interest on the remaining qubits. In Fig. 8, we show an example of a QCNN for a state ρ_α of $n = 8$ qubits and an observable H of the form (8) for $m = 1$ measured qubit.

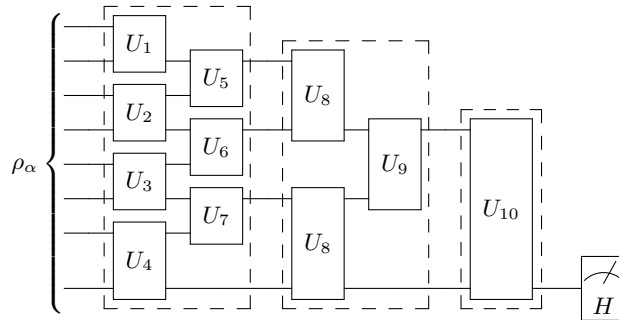


FIG. 8. Example of an eight-qubit QCNN with measuring an observable H of the form (8) with $m = 1$ measured qubit. In this implementation considered in [141], adjacent convolutional and pooling layers are combined into one layer shown by dashed frames, after each of which a half of the qubits is traced out. The two-qubit unitaries U_i can be constructed, e.g., from one- and two-qubit gates shown in Fig. 7.

Despite allowing to have fewer parameters in both \boldsymbol{x} and $\boldsymbol{\theta}$, it is not always advantageous to measure $m < n$ qubits, even if the corresponding observable H gives $\text{Tr } H\rho_\alpha = \alpha$. In Section V B 2, we consider a regression task in which, if one measures $m = 1$ qubit, one gets the variance $\Delta^2 H$ about twice as large as if measuring $m = 2$ qubits.

Appendix B: Mean squared error and Cramer-Rao bound for biased estimators

In Section II H, we mentioned that for a given ρ_α the estimator obtained from the expectation $\text{Tr } H\rho_\alpha$ of α can be biased. In this Appendix, following the works [58, 62, 64, 73], we derive the expressions for the MSE (33) and cCRB (34) for a biased estimator.

First, let us introduce a bias into our prediction,

$$\mathbf{a}(\alpha) \equiv \text{Tr } H\rho_\alpha = \alpha + b(\alpha), \quad (\text{B1})$$

where we have a bias $b(\alpha)$ and an observable in the form $H = \sum_i x_i \Pi_i$ with the operators $\{\Pi_i\}_i$ forming a POVM, and $x_i \in \mathbb{R}$. Denoting $p_i = \text{Tr } \Pi_i \rho_\alpha$, we can rewrite (B1) as

$$\mathbf{a}(\alpha) = \sum_i x_i p_i.$$

Now, suppose that we perform μ measurements for obtaining this expectation value in an experiment. Each measurement results in an outcome $m_k = x_i$ which is observed with probability p_i . Hence, the estimation of \mathbf{a} can be written as

$$\hat{\mathbf{a}} \equiv \frac{1}{\mu} \sum_{k=1}^{\mu} m_k.$$

In this expression, m_k are independent and identically distributed (i.i.d.) random variables, each on average giving $\langle m_k \rangle = \sum_i x_i p_i$ for all k . Then $\langle \hat{\mathbf{a}} \rangle = \mathbf{a}$ as in (B1). The MSE of the estimation $\hat{\mathbf{a}}$ is

$$\begin{aligned} \Delta^2 \hat{\mathbf{a}} &\equiv \langle (\hat{\mathbf{a}} - \mathbf{a})^2 \rangle = \langle \hat{\mathbf{a}}^2 \rangle - \langle \hat{\mathbf{a}} \rangle^2 = \left\langle \left(\frac{1}{\mu} \sum_{k=1}^{\mu} m_k \right)^2 \right\rangle - \left\langle \frac{1}{\mu} \sum_{k=1}^{\mu} m_k \right\rangle^2 = \frac{1}{\mu^2} \left(\sum_{k=1}^{\mu} \langle m_k^2 \rangle - \sum_{k=1}^{\mu} \langle m_k \rangle^2 \right) \\ &= \frac{1}{\mu^2} \left(\sum_{k=1}^{\mu} \sum_i x_i^2 p_i - \sum_{k=1}^{\mu} \left(\sum_i x_i p_i \right)^2 \right) = \frac{1}{\mu^2} \left(\mu \langle H^2 \rangle - \mu \langle H \rangle^2 \right) = \frac{1}{\mu} \Delta^2 H. \end{aligned}$$

In the derivation above, we used the property of i.i.d. random variables that $\langle m_k m_l \rangle = \langle m_k \rangle \langle m_l \rangle$ for $k \neq l$.

So, we have an expression of the error of the estimation $\hat{\mathbf{a}}$. However, after training and testing the model, one would observe neither $\Delta^2 \hat{\mathbf{a}}$ nor $\Delta^2 \hat{\alpha}$, but rather $\langle (\hat{\mathbf{a}} - \alpha)^2 \rangle$, i.e., the error between the estimation $\hat{\mathbf{a}}$ and the labels α from the training set. One can obtain it after the following chain of transformations:

$$\Delta^2 \hat{\mathbf{a}} \equiv \langle (\hat{\mathbf{a}} - \mathbf{a})^2 \rangle = \langle [(\hat{\mathbf{a}} - \alpha) - (\mathbf{a} - \alpha)]^2 \rangle = \langle (\hat{\mathbf{a}} - \alpha)^2 \rangle - (\mathbf{a} - \alpha)^2 = \langle (\hat{\mathbf{a}} - \alpha)^2 \rangle - b^2,$$

where we have inserted the bias from (B1) at the end. Now, since we obtained $\Delta^2 \hat{\mathbf{a}} = \Delta^2 H / \mu$, we can write

$$\langle (\hat{\mathbf{a}} - \alpha)^2 \rangle = \frac{\Delta^2 H}{\mu} + b^2, \quad (\text{B2})$$

which is the equation (33). Finally, recalling the error propagation formula (13) and qCRB (23), as well as noticing that

$$\frac{\Delta^2 \hat{\mathbf{a}}}{|\partial_\alpha \langle H \rangle|^2} = \frac{\Delta^2 H}{\mu |\partial_\alpha \langle H \rangle|^2} = \Delta^2 \hat{\alpha} \geq \frac{1}{\mu I_q},$$

we arrive to the desired inequality (34):

$$\langle (\hat{\mathbf{a}} - \alpha)^2 \rangle \geq \frac{|\partial_\alpha \langle H \rangle|^2}{\mu I_q} + b^2. \quad (\text{B3})$$

Interestingly, combining (B2) and (B3) and noticing that $\partial_\alpha b = \partial_\alpha \langle H \rangle - 1$, one can also obtain

$$\frac{\Delta^2 H}{|1 + \partial_\alpha b|^2} \geq \frac{1}{I_q}, \quad (\text{B4})$$

which can be used for estimating the Fisher information. Indeed, having trained the observable H , one obtains the variances $\Delta^2 H$ via measurements according to (15), and the bias $b = \text{Tr } H \rho_\alpha + \alpha$ is observed on the labels from the training set $\mathcal{T} = \{\rho_{\alpha_j}, \alpha_j\}_{j=1}^T$. Therefore, if the training set size T is sufficiently large, and the labels α_j are distributed uniformly, then one could try to approximate $\partial_\alpha b$ via finite differences. As an instance, for $1 < j < T$ and assuming $\alpha_j < \alpha_{j+1}$, the central difference approximation would be

$$\partial_\alpha b(\alpha) \Big|_{\alpha=\alpha_j} = \frac{b(\alpha_{j+1}) - b(\alpha_{j-1})}{\alpha_{j+1} - \alpha_{j-1}} + O((\alpha_{j+1} - \alpha_{j-1})^2).$$

Appendix C: Additional results

Here we provide additional results of numerical application of our method for predicting the negativity with various conditions (e.g., using fewer copies of the labeled state), and for solving other regression problems, such as predicting the angle of a Pauli rotation, and predicting the strength of transverse field for the Ising Hamiltonian.

1. Accounting for non-entangled states while predicting the negativity of isotropic states

In Section VB 2, we studied the prediction of the negativity N of isotropic states ρ_q with the restriction that there are no separable states with $q \leq 1/3$ in the training set. Importantly we would like to learn to predict not the coefficient q in (62), but the negativity N , which depends on q non-linearly. In this Appendix, we train our model on the sets $\mathcal{T} = \{\rho_{q_j}^{\otimes c}, N_j\}_{j=1}^{10}$, where $q_j \in [0, 1]$ and $c \in \{1, 4\}$. The results are shown in Fig. 9.

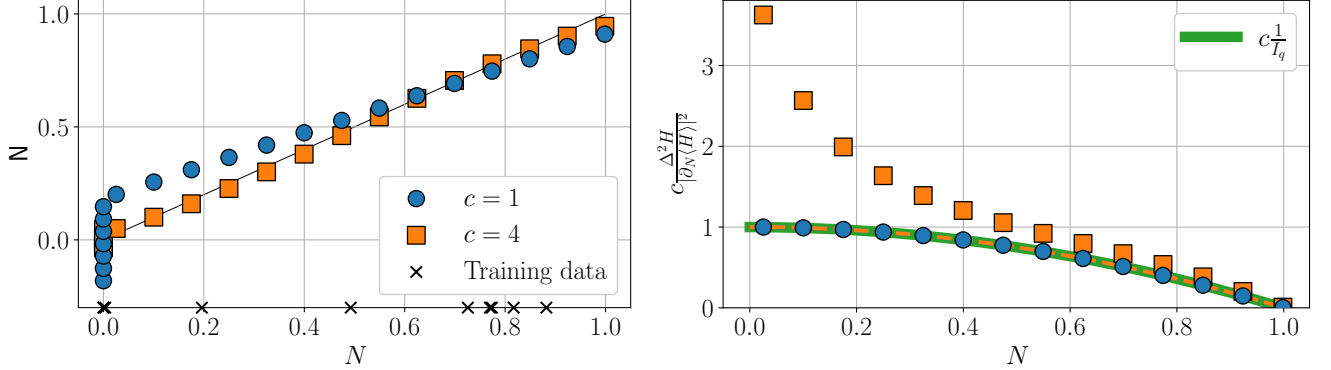


FIG. 9. Left: Predicted N vs. true N negativity of the isotropic state (62) estimated for different number of copies c processed simultaneously. Right: Variance (25) together with cCRB (dashed lines) and qCRB (solid green line), all scaled with c ; the points with $q \leq 1/3$ are excluded from this plot, as they give $\partial_N \langle H \rangle = 0$.

As can be seen, the model struggles to predict the negativities for $q \leq 1/3$, for which $N = 0$. However, the more copies c we process simultaneously, the more accurate our predictions for N become. A drawback is that in this case the observable (8) requires the measurement of all $m = 2c$ qubits, for which 2^m parameters \mathbf{x} have to be varied.

Additionally in Fig. 9, we show the variance of the trained observable H and the Cramer-Rao bounds (23). As can be seen, the quantum bound is saturated for a single copy of ρ_N . For both $c = 1$ and $c = 4$, our model finds the ansatz angles $\boldsymbol{\theta}$ which provide $I_c(\Pi(\boldsymbol{\theta}), \rho_N) = I_q(\rho_N)$, but the parameters \mathbf{x} do not give the desired variance of $H(\mathbf{x}, \boldsymbol{\theta})$ for $c = 4$. Note that $I_q(\rho_N^{\otimes c}) = c I_q(\rho_N)$, so the data in the plots are rescaled correspondingly.

2. Prediction of the negativity of random mixed states with fewer copies

In Section VB 4, we applied our method for predicting the negativity (57) of random mixed two-qubit states. To train the model, we processed $c = 4$ copies of the labeled state ρ_N simultaneously. Here we show how the performance of our method changes with processing a fewer number of copies. To train the model, as before, we generated a training set of $T = 1000$ random states with negativities evenly distributed on $[0, 1]$. Additionally, having trained the model with c copies, we use the optimal parameters $\mathbf{x}^*, \boldsymbol{\theta}^*$ as the initial ones for training the model with $c + 1$ copies.

In Fig. 10 the results of predicting the negativity of mixed states for $c \in \{1, 2, 3\}$ are shown. The model trained with only a single copy does not allow to predict anything, which is no surprise in light of the results presented in [118]. In contrast, with two copies, the prediction accuracy is much higher which is in line with our reasoning in Section V B 3. With three copies, the performance does not improve much in comparison to the case with two copies. Finally, with $c = 4$ copies, as we show in Section V B 4, the prediction accuracy increases significantly.

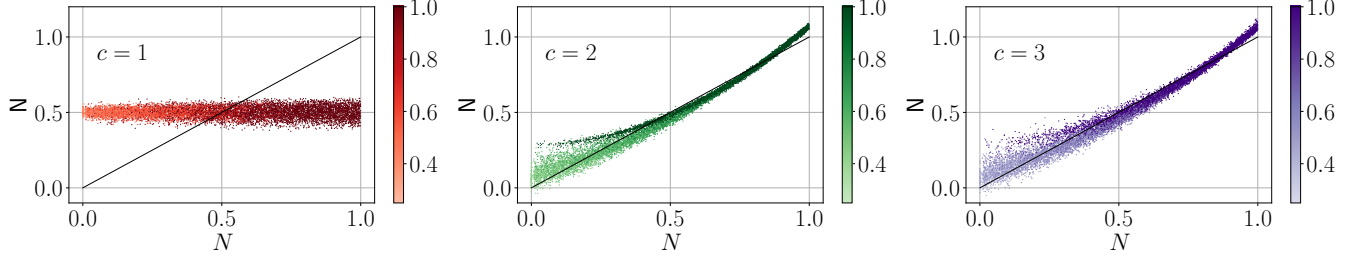


FIG. 10. Predicted \hat{N} vs. true N negativity of 10^4 random mixed states using an observable trained on $c = 1$ (left), $c = 2$ (center), and $c = 3$ (right) copies of the labeled states. The color of points indicates the purity of the corresponding states.

3. Prediction of the squared negativity of random mixed states

In Section V B 3 we have shown that one can predict the squared negativity N^2 of *pure* states using our method. In this Appendix, we test the performance of the method in predicting N^2 as well, but for random *mixed* states. In Fig. 11, we show the prediction accuracy for this case for $c \in \{2, 3, 4\}$ copies of the labeled state. Interestingly, while with $c = 2$ copies the prediction accuracy is quite high, the performance does not increase much for $c = 3$. In contrast, with $c = 4$, the prediction of N^2 is very precise, especially for more pure states. With $c = 1$ copy, we obtained the results similar to the ones presented in Fig. 10 (left) (not shown here).

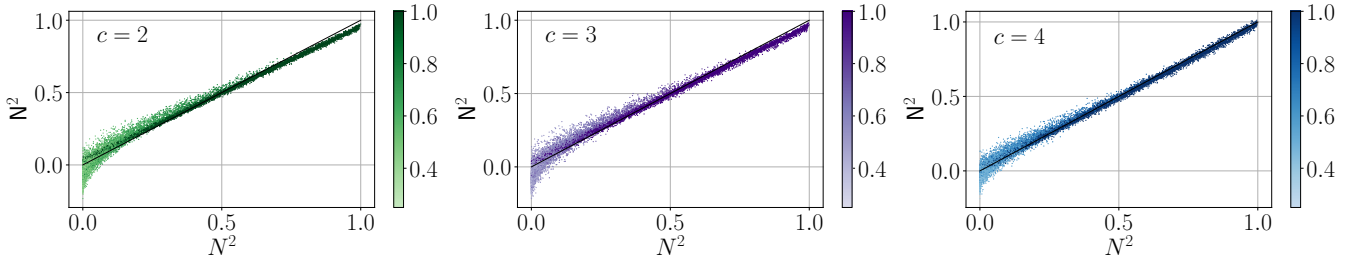


FIG. 11. Predicted \hat{N}^2 vs. true N^2 negativity of 10^4 random mixed states using an observable trained on $c = 2$ (left), $c = 3$ (center), and $c = 4$ (right) copies of the labeled states. The color of points indicates the purity of the corresponding states.

4. Compensation of a bias

As noted in Section II H, $\text{Tr } H \rho_\alpha$ generally evaluates to a function $\mathbf{a}(\alpha)$ instead of α itself. There is a bias $b(\alpha) = \mathbf{a}(\alpha) - \alpha$ which one can try to compensate. Indeed, after the training, we can observe the bias $b(\alpha_j)$ for $(\rho_{\alpha_j}, \alpha_j) \in \mathcal{T}$. One can plot the dependence of b on the obtained predictions \mathbf{a} . If this dependence is monotonic, the data points can be fitted with some function (e.g., polynomial of some degree), which we denote $\tilde{b}(\mathbf{a})$. This function can then be used for processing the predictions \mathbf{a} for unseen data.

In Fig. 12, we show the results of testing this bias compensation method for the case considered in Section V C, where we predicted the transverse field h of the Ising Hamiltonian with the variance weight $w_{\text{var}} = 1$. To fit the prediction \mathbf{h} , we used a polynomial of the degree 5. As can be seen, the values $\mathbf{h} - \tilde{b}$ provide very accurate predictions.

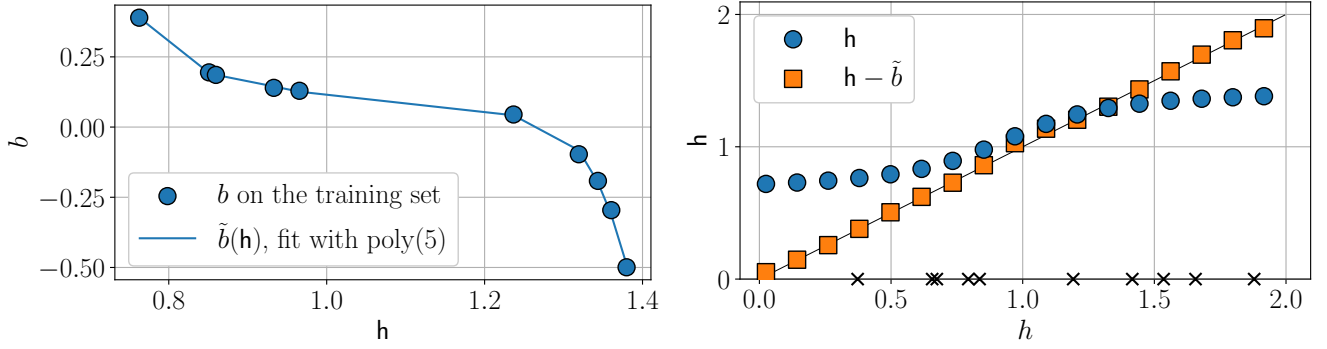


FIG. 12. Compensating the bias of the prediction of the transverse field of the Ising Hamiltonian (68) of $n = 8$ qubits. The observable H is trained on a set $\mathcal{T} = \{|\psi_j\rangle, h_j\}_{j=1}^{10}$ with $|\psi_j\rangle$ being the ground states of (68), the fields h_j are generated randomly, and the weights in (16) are set to $w_{\text{ls}} = w_{\text{var}} = 1$. Left: Dependence of the bias on the predictions for the training set, fitted with a function \tilde{b} being a polynomial of the degree 5. Right: Comparison of the “direct” predictions h with the bias-compensated ones $h - \tilde{b}$ on the testing set.

5. Measuring fewer qubits when predicting the negativity of random states

In Section V B 4, we studied the prediction of the negativity of random mixed states. We looked for an observable in the form (8) with measuring all $m = 8$ of $c = 4$ copies of two-qubit states. In this Appendix, we numerically study the performance and the training complexity of our method in this task with smaller m . For our simulations, we set $w_{\text{var}} = 10^{-4}$, use the hardware-efficient ansatz of $l = 5$ layers, and generate a training set of $T = 1000$ data points.

To speed up our calculations, we do the following. We start the minimization with $m = 1$ and random initial parameters $(\mathbf{x}, \boldsymbol{\theta})$. Once the optimization is terminated, we use the optimized parameters $(\mathbf{x}_1^*, \boldsymbol{\theta}_1^*)$ found for $m = 1$ as the initial ones for $m = 2$. Having obtained $(\mathbf{x}_2^*, \boldsymbol{\theta}_2^*)$ for $m = 2$, we use them to initialize the optimization for $m = 3$. This way, we keep increasing the number of measured qubits until $m = 8$. To quantify the performance of our method applied with different m , we consider the MSE

$$E(\mathbf{x}_m^*, \boldsymbol{\theta}_m^*) = \frac{1}{V} \sum_{j=1}^V \left(N_j - \mathbb{N}_j(\mathbf{x}_m^*, \boldsymbol{\theta}_m^*, \rho_{N_j}) \right)^2, \quad (\text{C1})$$

where $\mathbb{N}_j(\mathbf{x}_m^*, \boldsymbol{\theta}_m^*, \rho_{N_j}) = \text{Tr } H(\mathbf{x}_m^*, \boldsymbol{\theta}_m^*) \rho_{N_j}$ are the expectations calculated for the optimized observable $H(\mathbf{x}_m^*, \boldsymbol{\theta}_m^*)$ measured in a state from a testing set of the size $V = 10^4$.

In Fig. 13, we plot the dependence of the error (C1) on m . Additionally in this Figure, we show the number of times the BFGS optimizer called the cost function in (16). In our numerical experiments, the optimizer required at most about 2000 iterations to terminate for all m . However, at each iteration the BFGS algorithm evaluates the cost function several times (e.g., for computing the gradient). With each increment of m , we nearly double the number of trainable parameters, as well as the number of function evaluations performed by the optimizer.

Therefore, for large system sizes, it is prohibitive to use the proposed method with measuring all the qubits. In this particular case, however, each additional measured qubit may contribute to the gain of prediction accuracy, as one may notice from Fig. 13. To illustrate this, in Fig. 14 we show the prediction accuracy and the variance for an optimized observable on $m = 6$ qubits. Although one may find such results satisfactory, as there is an improvement over the two-copy case (see Fig. 10), the optimized observable on $m = 8$ qubits shows a better performance (see Fig. 5).

6. Training complexity and dependence on the training set size

In the most of our case studies, it was enough to train the model on a data set of a quite modest size T . One exception is the prediction of the negativity of mixed states considered in Section V B 4, for which we used a training set of the size $T = 1000$. In this Appendix, we numerically study the dependence of the performance of our method on the training set size. Such numerical experiment may consume a considerable amount of time to perform, so we restrict the number of iterations of the BFGS algorithm to 1500. Additionally, to speed up our simulation, we execute it as follows. First, we generate a training set $\mathcal{T} = \{\rho_j^{\otimes 4}, N_j\}_{j=1}^{1000}$. Then, we sample $\mathcal{T}_1 \equiv \{\rho_j^{\otimes 4}, N_j\}_{j=1}^{100} \subset \mathcal{T}$ and train our model on

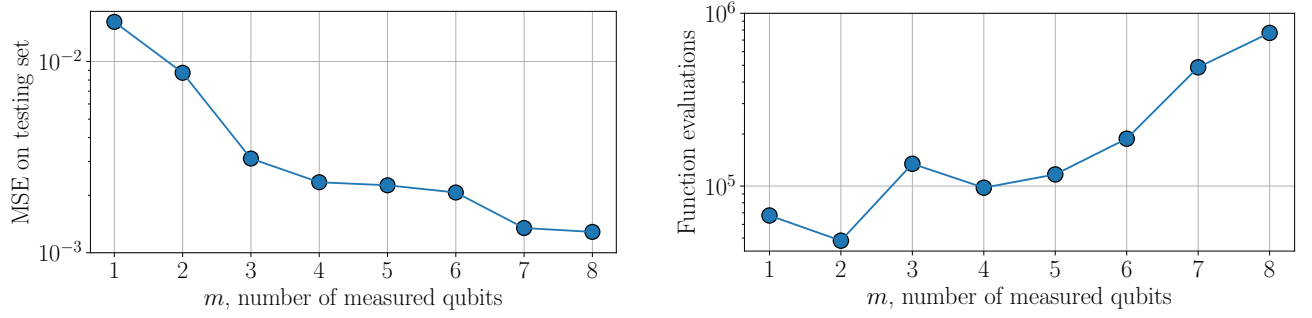


FIG. 13. Left: Testing error (C1) vs. the number of measured qubits m as per (8). Right: Number of evaluations of the cost function performed by the BFGS algorithm vs. the number of measured qubits m ; the number of function calls is *not* cumulative (i.e., it is obtained *individually* for each m).

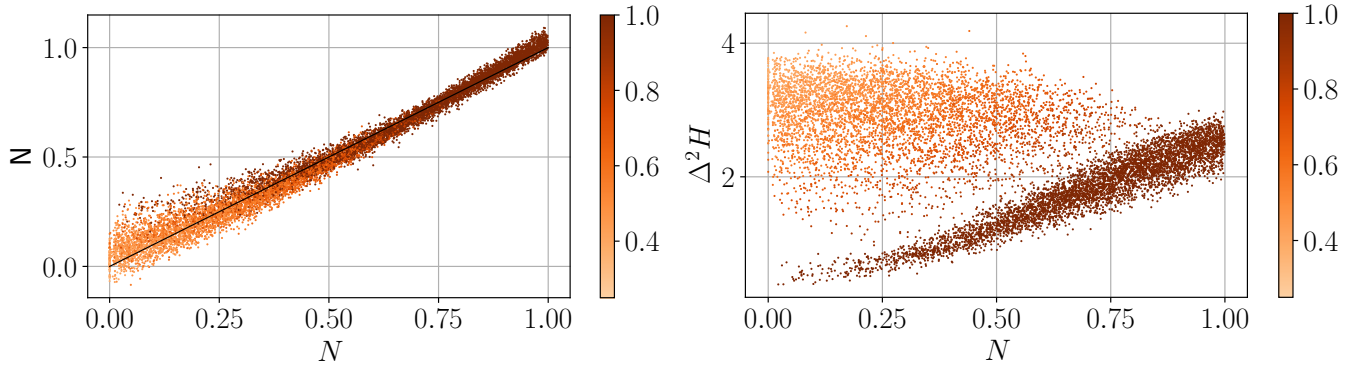


FIG. 14. Left: Predicted negativity \hat{N} of 10^4 random mixed states vs. the true negativity N for $c = 4$ copies and the trained observable H on $m = 6$ qubits. Right: Variance of the trained observable H . The color of points indicates the purity of the corresponding states.

this training set of $T = 100$ data points. Once the optimization for \mathcal{T}_1 has terminated, we use the obtained optimized parameters $(\mathbf{x}_1^*, \boldsymbol{\theta}_1^*)$ as the initial ones for training the model on the set $\mathcal{T}_2 \equiv \{\rho_j^{\otimes 4}, N_j\}_{j=1}^{200} = \mathcal{T}_1 \cup \{\rho_j^{\otimes 4}, N_j\}_{j=101}^{200}$ and get $(\mathbf{x}_2^*, \boldsymbol{\theta}_2^*)$. We keep training the model this way until reaching $\mathcal{T}_{10} = \mathcal{T}$.

To characterize the performance of our method with different T , we again consider the MSE (C1) evaluated on a testing set of $V = 10^4$ states for each $(\mathbf{x}_k^*, \boldsymbol{\theta}_k^*)$. As we show in Fig. 15, the error behaves as $T^{-5/4}$, so it expectedly decreases with the growth of the training set size T . Additionally in Fig. 15, we plot the number of evaluations of the cost function in (16) the BFGS algorithm had to perform before termination. Note that at each iteration, the BFGS algorithm calls the cost function several times, e.g., for calculating the gradient or performing the line search. For $T = 100, 200, 300$, the optimization stopped upon reaching the maximum number of iterations 1500 we set; for the rest values of T , the number of cost function evaluations tends to decrease with T . Note however that the growth of T leads to a bigger number of computed expectations in (16), i.e. it may increase the simulation time.

7. Training complexity of the prediction of the transverse field of the Ising Hamiltonian

In Section VC, we studied the prediction of the transverse field of the eight-qubit Ising Hamiltonian (68) with different variance weights $w_{\text{var}} \in \{1, 10^{-2}, 10^{-4}\}$. Here, we discuss the training complexity of this procedure. Recall that in the main text we performed the simulation for finding an observable in the form (8) with $m = 4$ measured qubits and the hardware-efficient ansatz of $l = 5$ layers.

In Fig. 16, we depict the optimization process for all the three weights w_{var} . To speed up our calculations, we first trained the observable with $w_{\text{var}} = 1$ starting from a random initialization of the trainable parameters, then we used the found optimal parameters $(\mathbf{x}^*, \boldsymbol{\theta}^*)$ as the initial ones for the optimization with $w_{\text{var}} = 10^{-2}$, and then did the same for $w_{\text{var}} = 10^{-4}$. As one sees in Fig. 16, the BFGS algorithm needs several thousands of iterations to converge.

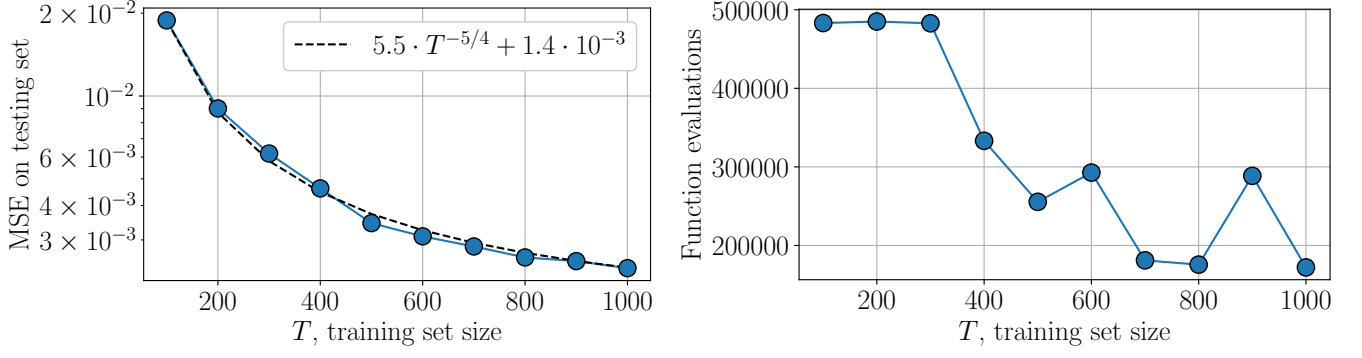


FIG. 15. Left: Testing error (C1) vs. the training set size T in the task of predicting the negativity of random two-qubit mixed states. Right: Number of evaluations of the cost function in (16) performed by the BFGS algorithm vs. the training set size T . The maximum number of iterations for the BFGS algorithm was set to 1500; note that at each iteration, the algorithm may call the cost function several times.

However, in contrast to the prediction of the negativity of random states discussed in Section V B 4, here we measure only $m = 4$ qubits out of $n = 8$. Despite that this significantly decreases the number of variational parameters, we had to increase the number of layers to $l = 5$. Note that it is more advantageous to consider larger l rather than larger m , as the number of parameters is linear in l and exponential in m . In our simulations, we also observe that for all considered weights w_{var} the number of function evaluations per iteration is approximately 152, which is slightly more than the number of trainable parameters.

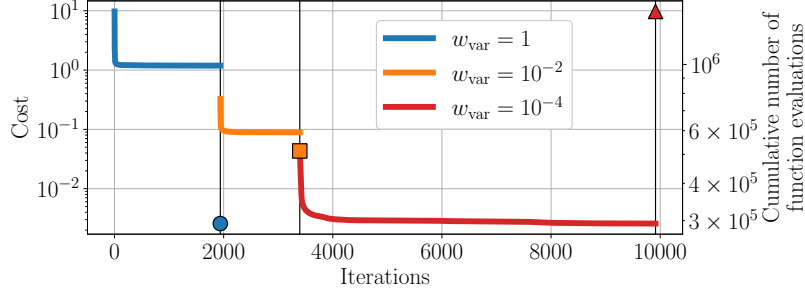


FIG. 16. Value of the cost function in (16) vs. iteration of the BFGS algorithm when training an observable for predicting the transverse field of the Ising Hamiltonian using an ansatz of $l = 5$ layers and measuring $m = 4$ qubits as per (8). The markers and the right vertical axis show the *cumulative* number of times the BFGS algorithm called the cost function in (16). The data are gathered from the numerical simulation for Fig. 6.

As mentioned in Section V C, one can obtain better results using an ansatz with fewer layers $l = 2$ but measuring all $m = 8$ qubits. The simulation results with these settings are shown in Fig. 17. Comparing it with the case of $m = 4$ and $l = 5$ in Fig. 6, one notices an improvement in terms of the variance, especially for $w_{\text{var}} = 1$. Moreover, we needed even less number of iterations of the BFGS algorithm to converge. However, one should rather look at the number of evaluations of the cost function in (16), which is greater for the case of $m = 8$. Indeed, the BFGS algorithm calls the function for calculating the gradient, and the number of calls therefore increases exponentially with m .

One may also notice that with $m = 8$ and $l = 2$ we obtain an observable such that $I_c(\Pi, \rho_\alpha) \approx I_q(\rho_\alpha)$. It shows that the ansatz is expressive enough for obtaining efficient eigenprojectors for all the weights w_{var} considered. This is in contrast to the case of $m = 4$ with $l = 5$ in Fig. 6, where the equality between classical and quantum FI was achieved only on a smaller interval of h . Thus, the number of varied eigenvalues may play an important role in the proposed method, at least for achieving lower variance in the considered regression problem.

8. Dependence on the number of measurements μ

In the main text of this work, we have performed our numerical experiments with the assumption that one can exactly compute the expectations $\mathbf{a} = \text{Tr } H \rho_\alpha$. In reality, however, one can have only an estimate $\hat{\mathbf{a}}$ obtained from

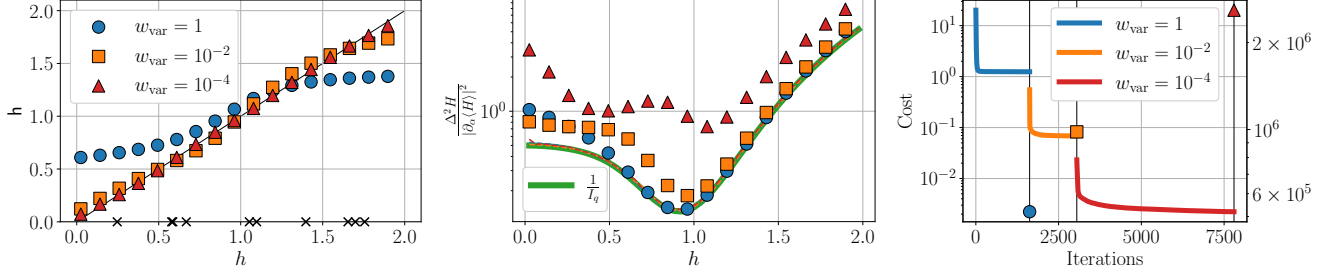


FIG. 17. Predicting the transverse field h for an 8-qubit Ising Hamiltonian (68) using an ansatz of $l = 2$ layers and measuring $m = 8$ qubits as per (8). Left: Predicted h vs. true h transverse field for different weights w_{var} in (16); the black crosses on the x -axis indicate the training data. Center: Variance (25) vs. h ; the dashed lines indicate cCRB (19). Right: Value of the cost function in (16) vs. iteration of the BFGS algorithm during the training; the markers and the right vertical axis show cumulative number of times the BFGS algorithm called the cost function in (16).

a μ -shot measurement experiment. In this Appendix, we numerically study the performance of our method when μ is finite. Namely, during the training, whenever the minimization algorithm calls the cost function in (16), for each data point ρ_{α_j} of the training set the expectation $\mathbf{a}_j = \text{Tr } H(\mathbf{x}, \boldsymbol{\theta}) \rho_{\alpha_j}$ is estimated as $\hat{\mathbf{a}}_j = \frac{1}{\mu} \sum_i x_i \mu_i$, where μ_i is the number of times the i th measurement outcome is observed. For the numerical experiments presented in this section, we set the variance weight in (16) to $w_{\text{var}} = 10^{-4}$.

To study the dependence of estimation accuracy on μ , here we consider two problems from the main text. Namely, an easier one of estimating the parameter of the amplitude damping channel (see Section V A), and a harder one of estimating the transverse field of the Ising Hamiltonian (see Section V C). Instead of the BFGS algorithm used for obtaining the results for the main text, here we apply the COBYQA minimizer which showed a better performance for finite μ among the algorithms built into SciPy [142].

a. Estimating the parameter of the amplitude-damping channel

First, we show the results for a relatively simple problem of estimating the parameter of the amplitude damping channel (50) given its output states $\rho_\alpha \equiv \Phi_\alpha[\rho]$ with the input $\rho = |+\rangle\langle+|$. In Fig. 18, we show the estimates $\hat{\mathbf{a}}$ of $\mathbf{a} = \text{Tr } H(\mathbf{x}^*, \boldsymbol{\theta}^*) \rho_\alpha$ for the number of shots $\mu \in \{2^6, 2^{10}, 2^{14}\}$. We note again that this number of shots was used for *both* training (while obtaining the optimized observable $H(\mathbf{x}^*, \boldsymbol{\theta}^*)$) and evaluating (computing the estimates $\hat{\mathbf{a}}_j$ for the states of the testing set) the model.

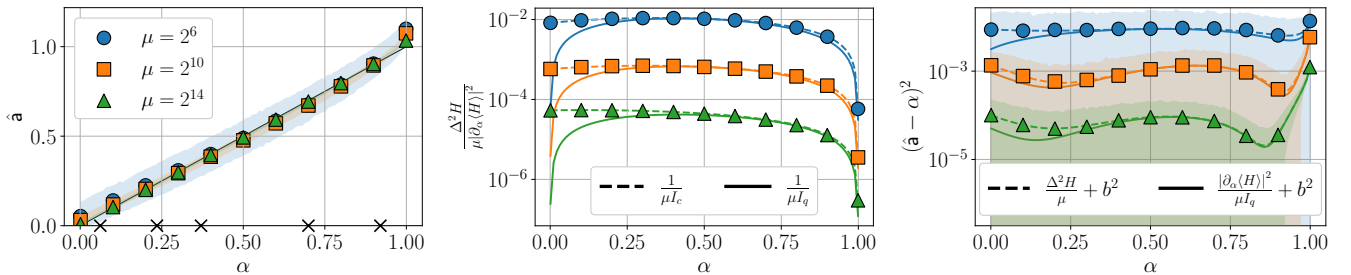


FIG. 18. Left: Estimate $\hat{\mathbf{a}}$ of the expectation $\mathbf{a} = \text{Tr } H(\mathbf{x}^*, \boldsymbol{\theta}^*) \rho_\alpha$ vs. true α parameter of the AD channel (50) for different numbers of measurement shots μ used during the training and testing; the black crosses on the x -axis indicate the training data. Center: Error propagation (13) vs. α for the observables trained with different μ ; the dashed and solid lines indicate the classical and quantum CRB, respectively. Right: Average of $(\hat{\mathbf{a}} - \alpha)^2$ over 1000 measurement experiments with μ shots each; the dashed and solid lines indicate the quantities (33) and (34), respectively. The observables H were trained on a set $\mathcal{T} = \{\rho_{\alpha_j}, \alpha_j\}_{j=1}^5$ with the parameters α_j generated randomly. The shaded areas indicate the standard deviation over 1000 measurement experiments with μ shots each.

Expectedly, the larger is μ , the more accurate is the estimation of \mathbf{a} . No surprise is also that the standard deviation of the estimation also decreases with μ . However, our results show that the number of shots may impact significantly not only the estimation accuracy itself, but also the training process. That is, smaller μ may result in an observable

with greater bias. Nonetheless, for this particular case, even the observable trained with a rather modest number of shots $\mu = 2^6$ gives quite accurate estimations; with a large $\mu = 2^{14}$, the results are close to those in Figs. 1 and 22, where μ is “infinite”. To verify the correctness of our numerical results, in Fig. 18 we also plot the expressions (33) and (34), and observe that they are indeed satisfied. Moreover, one can see that the Cramer-Rao bounds plotted in this figure resemble the ones shown in Figs. 1 and 22 (mind the scale of the y -axis).

b. Estimating the transverse field of the Ising Hamiltonian

When simulating the finite number of measurement shots μ , the task of estimating the transverse field of the Ising Hamiltonian is more challenging. As in Section V C, here we consider 8-qubit Ising Hamiltonian (68). We look for an optimal observable in the form (8), where we measure $m = 4$ qubits and use the variational ansatz of $l = 5$ layers.

In Fig. 19, we show the estimates \hat{h} of the expectations $h = \langle \psi_h | H(\mathbf{x}^*, \boldsymbol{\theta}^*) | \psi_h \rangle$ obtained with the number of shots $\mu \in \{2^6, 2^{10}, 2^{14}\}$. As for the AD channel, the estimation accuracy grows with μ . However, in this case, with a large $\mu = 2^{14}$ we do not reach the accuracy shown in Fig. 6 for “infinite” μ . This may be due to the larger system size as well as because of a more complex relation between h and $|\psi_h\rangle$.

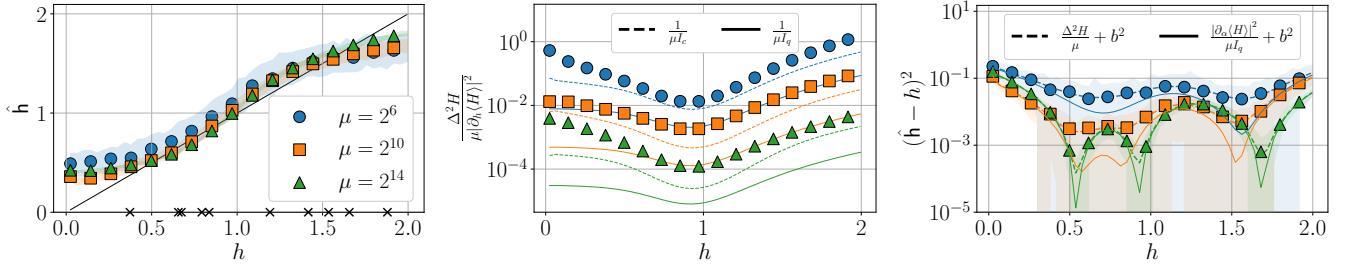


FIG. 19. Left: Estimate \hat{h} of the expectation $h = \langle \psi_h | H(\mathbf{x}^*, \boldsymbol{\theta}^*) | \psi_h \rangle$ vs. true h transverse field of the 8-qubit Ising Hamiltonian (68) for different number of measurement shots μ used during the training and testing; the black crosses on the x -axis indicate the training data. Center: Error propagation (13) vs. h for the observables trained with different μ ; the dashed and solid lines indicate the classical and quantum CRB, respectively. Right: Average of $(\hat{h} - h)^2$ over 100 measurement experiments with μ shots each; the dashed and solid lines indicate the quantities (33) and (34), respectively. The observables H were trained on a set $\mathcal{T} = \{|\psi_{h_j}\rangle, h_j\}_{j=1}^{10}$ with $|\psi_j\rangle$ being the ground states of (68), and the fields h_j are generated randomly. The shaded areas indicate the standard deviation over 100 measurement experiments with μ shots each.

To investigate the impact of the number of shots μ on training and testing, in Fig. 20 we plot the dependence of MSE evaluated on a testing set against μ . Additionally in this Figure, we show the number of times the COBYQA minimizer calls the cost function in (16) during the training. As expected, MSE decreases with the number of shots μ . The number of function evaluations, however, also tends to grow.

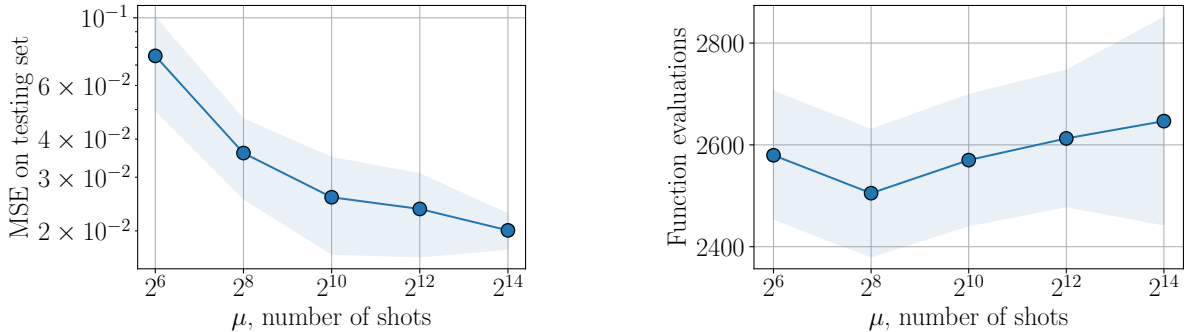


FIG. 20. MSE evaluated on a testing set (left) and number evaluations of the cost function in (16) made by the COBYQA algorithm (right) vs. the number of shots μ used to estimate the expected values during the training. The shaded area shows the standard deviation obtained over 10 models trained with different initial parameters $(\mathbf{x}, \boldsymbol{\theta})$.

9. Channel parameter prediction

Here our method is applied for learning to predict the parameter α of a parametrized channel Φ_α , i.e. the labeled states have the form $\rho_\alpha = \Phi_\alpha[\rho]$ for some *fixed* input state ρ .

a. Depolarizing channel

Let us consider the single-qubit depolarizing channel

$$\Phi_\alpha[\rho] = (1 - \alpha)\rho + \frac{\alpha}{2}\mathbb{1}, \quad (\text{C2})$$

which we have already mentioned in Section II D. Representing the input state as $\rho = \frac{1}{2}(\mathbb{1} + \sum_{j=1}^3 r_j \sigma_j)$ with $r_j \in \mathbb{R}$, one can find the (unnormalized) eigenvectors $|l_k\rangle$ of the SLD operator L of the output state $\rho_\alpha = \Phi_\alpha[\rho]$ to be

$$|l_{1,2}\rangle = \frac{r_3 \pm \sqrt{r_1^2 + r_2^2 + r_3^2}}{r_1 + ir_2} |0\rangle + |1\rangle,$$

which do not depend on the label α . Therefore, a POVM Π which saturates qCRB (23) should not depend on α as well. Let us set the input state to $\rho = |+\rangle\langle+|$. For this input, one can obtain the SLD operator for the output ρ_α as

$$L = \frac{1}{\alpha} |+\rangle\langle+| + \frac{1}{\alpha - 2} |-\rangle\langle-|,$$

which, by formula (22), gives $I_q(\rho_\alpha) = 1/(2\alpha - \alpha^2)$. Note the equality of this to the reciprocal of (12) with $h_2 = h_3 = 0$. In Fig. 21, we show the performance of our method in predicting α for the depolarized state ρ_α . As can be seen, trained on a set of five states with random depolarization strengths α , our model finds an observable giving both accurate predictions and variance saturating the qCRB.

For the input state $\rho = |+\rangle\langle+|$ of the depolarizing channel, we can also solve (40) to obtain an optimal observable $H_0 = \frac{3k+10}{3k+15}\mathbb{1} - \frac{k}{k+5}\sigma_x$. In the limit of large k (small variance weight w_{var}) and for the output state $\Phi_\alpha[\rho]$, this observable gives $\langle H_0 \rangle = \alpha$ and $\Delta^2 H_0 = 2\alpha - \alpha^2$, which matches the results shown in Fig. 21. Additionally in this Figure, we plot prediction accuracy and the variance for the observable obtained via the minimization of the Bayesian MSE (26). For this case, putting $k = 1$ into H_0 found earlier, one can calculate the Bayesian qCRB (30) to obtain

$$\Delta_B^2 \alpha = \Delta_p^2 \alpha - I_B = \frac{10}{81} \approx 0.12345679,$$

the value achieved in our simulations of the Bayesian approach.

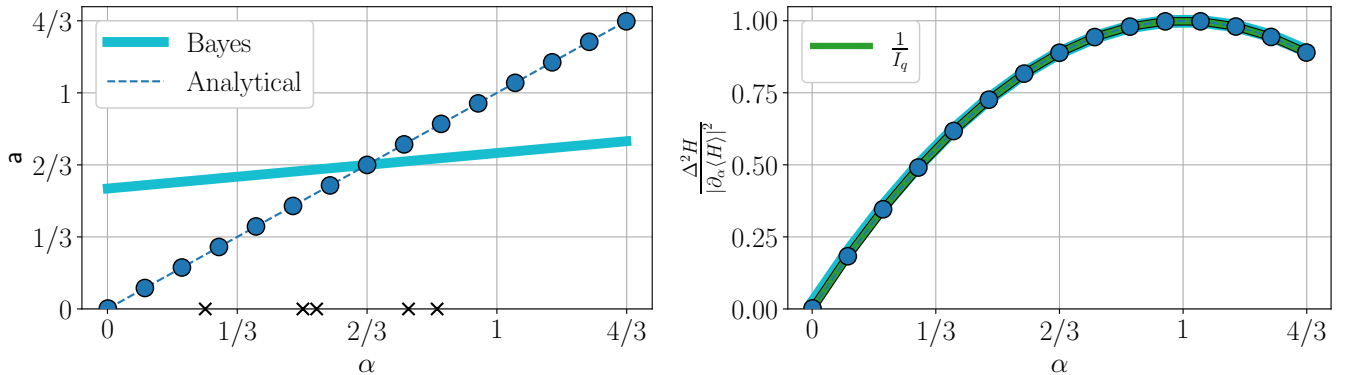


FIG. 21. Left: Predicted a depolarization strength α of the depolarizing channel (C2) with the input state $\rho = |+\rangle\langle+|$. Right: Variance (25) of the optimized observable H . The observable was trained on a set $\mathcal{T} = \{\rho_{\alpha_j}, \alpha_j\}_{j=1}^5$ with random labels α_j indicated as black crosses in the left panel. In both panels, the solid blue line indicates the data for the observable obtained via the Bayesian approach (26).

b. Amplitude damping channel

In Section V A, we considered the amplitude damping (AD) channel

$$\Phi_\alpha[\rho] = \sum_{k=1}^2 V_k(\alpha) \rho V_k^\dagger(\alpha) \quad (\text{C3})$$

with the Kraus operators

$$V_1(\alpha) = \sqrt{\alpha} |0\rangle\langle 1|, \quad V_2(\alpha) = |0\rangle\langle 0| + \sqrt{1-\alpha} |1\rangle\langle 1|.$$

and the input state $\rho = |+\rangle\langle +|$. This is a single-qubit channel which models the decay from the excited state $|1\rangle$ to the ground state $|0\rangle$ [138]. Let us now consider the input state for this channel in the Bloch representation

$$\rho = \frac{1}{2} (\mathbb{1} + \vec{r} \cdot \vec{\sigma}),$$

where $\vec{r} \cdot \vec{\sigma} \equiv \sum_{i=1}^3 r_i \sigma_i$ with $||\vec{r}|| \leq 1$. The output state of the channel therefore reads

$$\Phi_\alpha[\rho] = \frac{1}{2} (\mathbb{1} + \vec{r}_\alpha \cdot \vec{\sigma}), \quad (\text{C4})$$

where $\vec{r}_\alpha = \vec{r}(\alpha)$ is the output state Bloch vector with the components

$$r_x(\alpha) = \sqrt{1-\alpha} r_x, \quad r_y(\alpha) = \sqrt{1-\alpha} r_y, \quad r_z(\alpha) = (1-\alpha) r_z + \alpha. \quad (\text{C5})$$

Let us assume that $r_z = 0$, then by formula (D4) we obtain the following structure of the SLD operator:

$$L = c \mathbb{1} + \vec{a} \cdot \vec{\sigma}, \quad (\text{C6})$$

where

$$c = \frac{r^2 - 2\alpha}{2(1-\alpha)(1+\alpha-r^2)}, \quad (\text{C7})$$

with $r \equiv ||\vec{r}||$, and the components of the vector \vec{a} are

$$a_{x,y} = -\frac{\sqrt{1-\alpha} r_{x,y}}{2(1+\alpha-r^2)}, \quad a_z = \frac{2 + (\alpha-2)r^2}{2(1-\alpha)(1+\alpha-r^2)}. \quad (\text{C8})$$

The eigenvector decomposition of L reads

$$L = (c+a) |\vec{a}\rangle\langle \vec{a}| + (c-a) |-\vec{a}\rangle\langle -\vec{a}|, \quad (\text{C9})$$

where $a \equiv ||\vec{a}||$ and

$$|\vec{a}\rangle = \cos \frac{\theta}{2} |0\rangle + \sin \frac{\theta}{2} e^{i\varphi} |1\rangle$$

with θ, φ such that $a_z/a = \cos \theta$, $(a_x + ia_y)/a = \sin \theta e^{i\varphi}$. More explicitly,

$$L = \lambda_+ |\vec{a}\rangle\langle \vec{a}| + \lambda_- |-\vec{a}\rangle\langle -\vec{a}|, \quad (\text{C10})$$

where

$$\lambda_\pm = \frac{r^2 - 2\alpha \pm \sqrt{(\alpha-2)^2 r^4 + [(1-\alpha)^3 + 4(\alpha-2)] r^2 + 4}}{2(1-\alpha)(1+\alpha-r^2)}. \quad (\text{C11})$$

Let us consider two input states ρ for the amplitude-damping channel. First, if $r = 0$, then the input is the maximally mixed state $\rho = \frac{1}{2} \mathbb{1}$, for which Eqs. (C10) and (C11) yield

$$L = \frac{1}{\alpha+1} |0\rangle\langle 0| + \frac{1}{\alpha-1} |1\rangle\langle 1|, \quad (\text{C12})$$

with the eigenprojectors of L not depending on α , and giving $I_q(\rho_\alpha) = 1/(1-\alpha^2)$. Second, if $\vec{r} = \vec{e}_x$, which corresponds to $\rho = |+\rangle\langle+|$, the eigenvectors of the SLD operator (C10) are characterized by the vector \vec{a} , which in this case has components

$$a_x = -\frac{\sqrt{1-\alpha}}{2\alpha}, \quad a_y = 0, \quad a_z = \frac{1}{2(1-\alpha)}. \quad (\text{C13})$$

The eigenvalues of the SLD operator are

$$\lambda_{\pm} = \frac{1 - 2\alpha \pm \sqrt{(1-\alpha)^3 + \alpha^2}}{2\alpha(1-\alpha)}. \quad (\text{C14})$$

Using (D6), one also obtains $I_q(\rho_\alpha) = (1+\alpha)/[4\alpha(1-\alpha)]$.

Let us look how our model predicts the amplitude-damping channel parameter for $\rho_\alpha = \Phi_\alpha[\rho]$. For both above-mentioned inputs $\rho = \frac{1}{2}\mathbb{1}$ and $\rho = |+\rangle\langle+|$, we find observables which give accurate predictions of α . Interestingly, for either of the inputs, a simple observable $H = \sigma_z$ gives $\text{Tr } H\rho_\alpha = \alpha$. Moreover, for $\rho = \frac{1}{2}\mathbb{1}$, this observable saturates qCRB, which can be verified by combining (C12) and (24). In contrast, $H = \sigma_z$ is not optimal for $\rho = |+\rangle\langle+|$ in the sense of the variance. As can be seen in Fig. 22, our model does not find an observable saturating qCRB in this case. From (C10) and (C11), one can notice that the eigenprojectors of L depend on the parameter α . If $\alpha \rightarrow 0$ the optimal POVM tends to $\{|+\rangle\langle+|, |-\rangle\langle-|\}$, while at the other end of the parameter range, $\alpha \rightarrow 1$, the optimal POVM is $\{|0\rangle\langle 0|, |1\rangle\langle 1|\}$.

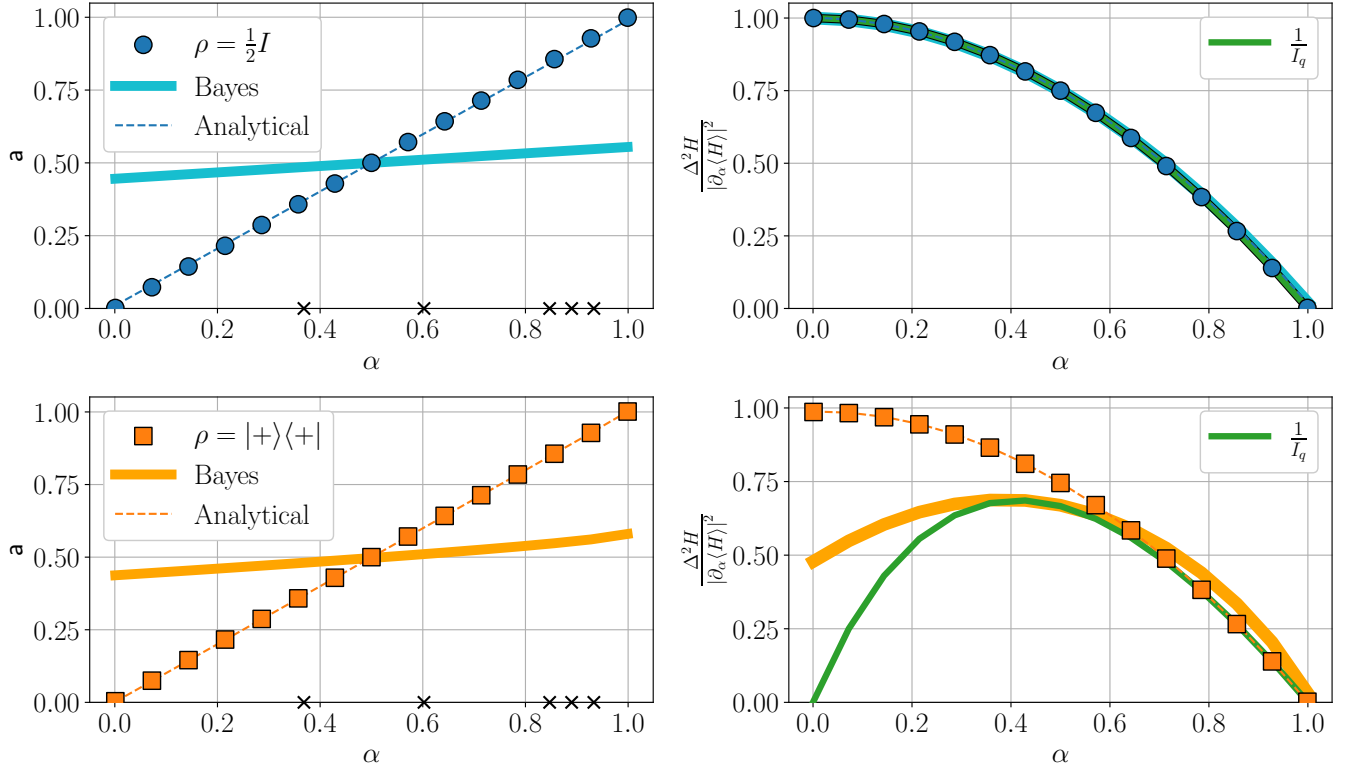


FIG. 22. Left: Predicted $\hat{\alpha}$ vs. true α parameters of the AD channel (C3) for the input states $\rho = \frac{1}{2}\mathbb{1}$ (upper, blue) and $\rho = |+\rangle\langle+|$ (lower, orange). Right: Variance (25) of the trained observable. The models were trained on a set $\mathcal{T} = \{\rho_{\alpha_j}, \alpha_j\}_{j=1}^5$ with random α_j , which are indicated as black crosses in the left panels. In all panels, the blue and orange solid lines indicate the results of the Bayesian approach (26). The dashed lines stand for the analytical solutions obtained by solving (40).

In Section V A, we obtained an optimal observable by solving (40) for the input state $\rho = |+\rangle\langle+|$. Here, similarly, we find such an observable in the form $H_0 = \sum_{i=0}^3 h_i \sigma_i$ for the input $\rho = \frac{1}{2}\mathbb{1}$. The optimal observable in this case is $H_0 = \frac{h_0}{k+8}\mathbb{1} + \frac{k}{8+4}\sigma_z$ yielding $\langle H_0 \rangle_{\rho_\alpha} = \frac{\alpha k + 4}{k+8}$ and $\Delta^2 H_0 = \frac{(1-\alpha^2)k^2}{(k+8)^2}$. For sufficiently large k , i.e. $k \rightarrow \infty$, we obtain $\langle H_0 \rangle_{\rho_\alpha} = \alpha$ and $\Delta^2 H_0 = 1 - \alpha^2$.

In Fig. 22, we also show the results for the observables obtained using the Bayesian approach (26) for both inputs $\rho = |+\rangle\langle+|$ and $\rho = \frac{1}{2}\mathbb{1}$. For the former, the results were shown in Section V A. For the latter, employing the optimal observable obtained above for $k = 1$, one can calculate the Bayesian qCRB (30) to be

$$\Delta_B^2 \alpha = \Delta_p^2 \alpha - I_B = \frac{2}{27} \approx 0.074074074$$

We achieve this value of Bayesian MSE in our simulations, saturating therefore the Bayesian qCRB.

c. Unitary transformation

Let us consider a unitary channel Φ_α which performs the z -rotation of a single-qubit state ρ by an angle $\alpha/2$:

$$\Phi_\alpha[\rho] = e^{-i\alpha\sigma_z/2} \rho e^{i\alpha\sigma_z/2}, \quad \alpha \in [0, \pi]. \quad (\text{C15})$$

Such transformation is often considered in the area of quantum channel estimation and quantum metrology as it incarnates, e.g., the Ramsey interferometry [65]. The main obstacle for us in predicting the label for ρ_α with our method is that we cannot directly obtain α as the expected value of some observable H . Instead, as noted in Section II H, our prediction is generally biased. However, one can suppress this bias by training an observable acting on a number of copies of the labeled state.

Indeed, let $\rho = |+\rangle\langle+|$ and consider c copies of this state passed through the channel (C15):

$$\begin{aligned} \rho_\alpha^{\otimes c} &= \left[e^{-i\alpha\sigma_z/2} |+\rangle\langle+| e^{i\alpha\sigma_z/2} \right]^{\otimes c} \\ &= \left[\frac{1}{2} (\mathbb{1} + e^{i\alpha} |1\rangle\langle 0| + e^{-i\alpha} |0\rangle\langle 1|) \right]^{\otimes c} \\ &= \frac{1}{2^c} \left[\mathbb{1}^{\otimes c} + \sum_{k=1}^c \left(e^{ik\alpha} |0\rangle\langle 1|^{\otimes k} + e^{-ik\alpha} |1\rangle\langle 0|^{\otimes k} \right) \otimes \mathbb{1}^{\otimes(c-k)} + R \right], \end{aligned}$$

where in the last line R is the rest of terms to complete $\rho_\alpha^{\otimes c}$. From this expansion, one can *guess* an observable H_c such that

$$\text{Tr} \rho_\alpha^{\otimes c} H_c = i \sum_{k=1}^c \frac{(-1)^k}{k} (e^{ik\alpha} - e^{-ik\alpha}), \quad (\text{C16})$$

which is precisely the first c terms of the Fourier series of the function $f(\alpha) = \alpha$. Indeed, if we take

$$H_c = i \sum_{k=1}^c \frac{(-2)^k}{k} \left(|0\rangle\langle 1|^{\otimes k} - |1\rangle\langle 0|^{\otimes k} \right) \otimes \mathbb{1}^{\otimes(c-k)}, \quad (\text{C17})$$

then we get

$$\begin{aligned} \text{Tr} \rho_\alpha^{\otimes c} H_c &= i \sum_{k=1}^c \frac{(-2)^k}{k} \text{Tr} \left[\left(\rho_\alpha^{\otimes k} \otimes \rho_\alpha^{\otimes(c-k)} \right) \left((|0\rangle\langle 1|^{\otimes k} - |1\rangle\langle 0|^{\otimes k}) \otimes \mathbb{1}^{\otimes(c-k)} \right) \right] \\ &= i \sum_{k=1}^c \frac{(-2)^k}{k} \text{Tr} \left[\rho_\alpha^{\otimes k} \left(|0\rangle\langle 1|^{\otimes k} - |1\rangle\langle 0|^{\otimes k} \right) \right] \\ &= i \sum_{k=1}^c \frac{(-2)^k}{k} \left(\langle 1 | \rho_\alpha | 0 \rangle^k - \langle 0 | \rho_\alpha | 1 \rangle^k \right) \\ &= i \sum_{k=1}^c \frac{(-1)^k}{k} (e^{ik\alpha} - e^{-ik\alpha}). \end{aligned}$$

Therefore, we can expect that the more copies c of the state ρ_α we process simultaneously, the more $\text{Tr} \rho_\alpha^{\otimes c} H_c$ gets closer to α (i.e. the lower is the bias). The example of rotation angle α prediction in (C15) confirms that as shown in Fig. 23. As can be seen, already with a single copy ($c = 1$) we obtain quite an accurate estimation for α , which

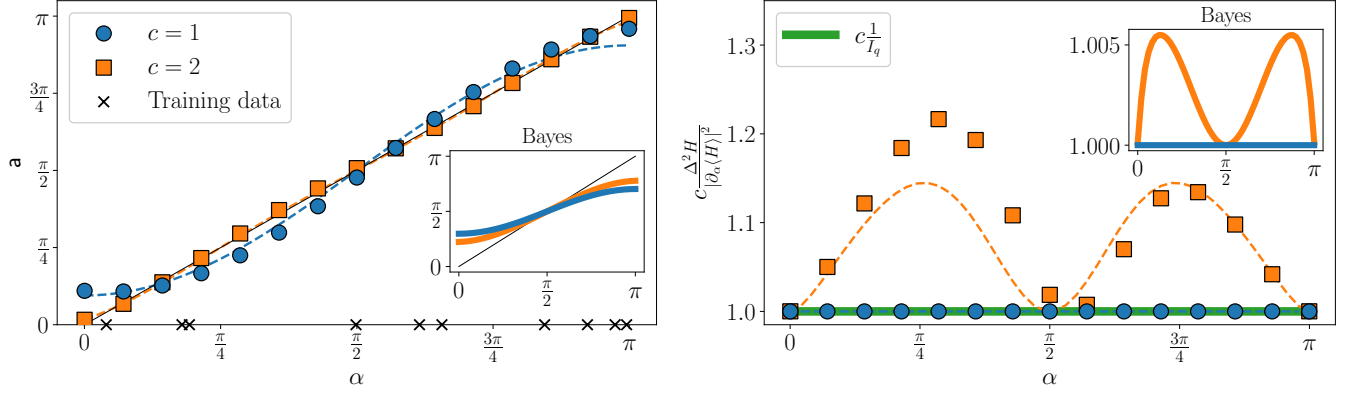


FIG. 23. Left: Predicted $\hat{\alpha}$ vs. true α rotation angle of the state (C15). Right: Variance (25) of the trained observables. The observables H are trained on a set $\mathcal{T}_c = \{\rho_j^{\otimes c}, \alpha_j\}_{j=1}^{10}$ with randomly generated α_j and $c = 1, 2$ simultaneously processed copies. In both panels, the dashed lines of the corresponding colors indicate the data given by the optimal observables (C18) and (C19). The insets show the data for the observables obtained via the minimization of the Bayesian MSE (26).

significantly improves with $c = 2$ copies. However, in contrast to the single-copy case, with two copies we do not saturate CRB (23).

Solving the equation (40) for the channel (C15) with the input state $\rho = |+\rangle\langle+|$, one can obtain the following optimal observable for the case $c = 1$ to be

$$H_1 = \frac{\pi}{2} \mathbb{1} - \frac{4k}{\pi(1+k)} \sigma_x. \quad (\text{C18})$$

Similarly for $c = 2$ copies, the optimal observable takes the form

$$H_2 = \left(\frac{\pi}{2} - t\right) \mathbb{1} \otimes \mathbb{1} + t(\sigma_x \otimes \sigma_x + \sigma_y \otimes \sigma_y + \sigma_z \otimes \sigma_z) - \frac{12k\pi(k+8)}{r(1+2k)} (\mathbb{1} \otimes \sigma_x + \sigma_x \otimes \mathbb{1}) - \frac{3k(3\pi^2 - 32)}{r} (\sigma_x \otimes \sigma_y + \sigma_y \otimes \sigma_x), \quad (\text{C19})$$

where $r = -32 - 64k + 27\pi^2 + 9k\pi^2$ and t is arbitrary. The predictions obtained with these observables, as well as their variance, are shown in Fig. 23. It may seem that these predictions do not agree with the results obtained via the method (16), especially for the variance. Recall however that the observables (C18) and (C19) are obtained with the assumption of a large training set, i.e., $T \rightarrow \infty$. When we set $T = 1000$, our simulations show almost perfect agreement with this analytical solution.

It should also be noted that the Bayesian approach produces an observable with a smaller variance, but in exchange to a large bias. One can also verify that the both observables (C18) and (C19) with $k = 1$ saturate the Bayesian qCRB (30) evaluating to, respectively,

$$\frac{\pi^4 - 48}{12\pi^2} \approx 0.417182, \quad -\frac{1}{8} + \frac{\pi^2}{12} + \frac{9}{8 - 3\pi^2} \approx 0.28097,$$

which were achieved in our simulations.

For a more general one-qubit unitary transformation

$$\Phi_\alpha[\rho] = e^{-i\alpha \vec{n} \cdot \vec{\sigma}} \rho e^{if_\alpha \vec{n} \cdot \vec{\sigma}}, \quad (\text{C20})$$

with $f_\alpha \equiv f(\alpha)$ being an arbitrary function of parameter α and $\vec{n} \cdot \vec{\sigma} \equiv \sum_i \sigma_i n_i$ the generator of rotation around the axis parallel to a given fixed unit vector \vec{n} , one can single out the properties that affect the prediction error. Indeed, let the input state be given by the Bloch representation $\rho = 1/2(I + \vec{r} \cdot \vec{\sigma})$. One can use Eqs. (22) and (D2) to calculate qFI of the output state:

$$I_q(\Phi_\alpha[\rho]) = 4(\partial_\alpha f_\alpha)^2 r^2 \sin^2(\hat{\vec{n}} \hat{\vec{r}}), \quad (\text{C21})$$

where $\partial_\alpha f_\alpha$ is the derivative of f with respect to α and $\hat{\vec{n}} \hat{\vec{r}}$ is an angle between vectors \vec{n} and \vec{P} . From this expression, it can be seen that the effects of functional dependence on the parameter and mixedness of the input state are isolated

in the factors $(\partial_\alpha f_\alpha)^2$ and r^2 , respectively. Since qFI appears in the denominator of the qCRB (23), these two factors significantly affect the estimation error $\Delta^2 \hat{\alpha}$. In particular, the case of highly mixed input states ($r \ll 1$) is expected to require higher number of measurements in comparison with pure case to achieve reasonable values of the estimation error.

Appendix D: Formulas for SLD operator and quantum Fisher information

For an n -qubit state ρ_α , qFI can be calculated as $I_q(\rho_\alpha) = \text{Tr } L^2 \rho_\alpha$, where the SLD operator L was defined in Eq. (21). Although defined implicitly, L can be expressed in the basis of $\rho_\alpha = \sum_{k=1}^d \lambda_k |\lambda_k\rangle\langle\lambda_k|$ as

$$L = 2 \sum_{k,l=1}^{2^n} \frac{\langle \lambda_k | \partial_\alpha \rho_\alpha | \lambda_l \rangle}{\lambda_k + \lambda_l} |\lambda_k\rangle\langle\lambda_l|, \quad (\text{D1})$$

where the summation is taken over the indices k and l such that $\lambda_k + \lambda_l \neq 0$ [56, 143]. If ρ_α possesses certain properties, one can obtain L more conveniently [144]. For a mixed single-qubit state, one can write

$$L = 2\partial_\alpha \rho_\alpha - \frac{1}{2} \rho_\alpha^{-1} \partial_\alpha \text{Tr } \rho_\alpha^2, \quad \rho_\alpha^{-1} = \frac{2}{1 - \text{Tr } \rho_\alpha^2} \sigma_y \rho_\alpha^T \sigma_y. \quad (\text{D2})$$

Additionally, if $[\partial_\alpha \rho_\alpha, \rho_\alpha^{-1}] = 0$, then $L = \rho_\alpha^{-1} \partial_\alpha \rho_\alpha$. For a pure state $\rho_\alpha = |\psi_\alpha\rangle\langle\psi_\alpha|$, the SLD operator is simply

$$L = 2\partial_\alpha \rho_\alpha. \quad (\text{D3})$$

Finally, for a single-qubit state in the Bloch representation $\rho_\alpha = \frac{1}{2}(\mathbb{1} + \vec{r}_\alpha \cdot \vec{\sigma})$, where $\vec{r}_\alpha = \vec{r}(\alpha) \in \mathbb{R}^3$ and $\vec{r}_\alpha \cdot \vec{\sigma} \equiv \sum_{i=1}^3 r_i(\alpha) \sigma_i$, one can use the following expression [69]:

$$L = \partial_\alpha \vec{r}_\alpha \cdot \vec{\sigma} + \frac{\vec{r}_\alpha \cdot \partial_\alpha \vec{r}_\alpha}{1 - \|\vec{r}_\alpha\|^2} (\vec{r}_\alpha \cdot \vec{\sigma} - \mathbb{1}). \quad (\text{D4})$$

It is also possible to obtain the qFI directly without calculating the SLD operator. For instance, the following expression is especially useful for numerical calculations

$$I_q(\rho_\alpha) = 8 \frac{1 - F(\rho_\alpha, \rho_{\alpha+d\alpha})}{d\alpha^2}, \quad (\text{D5})$$

where in the numerator we have the fidelity $F(\rho, \tau) = \text{Tr } \sqrt{\sqrt{\rho} \tau \sqrt{\rho}}$ between quantum states ρ and τ [37, 58]. Additionally, if ρ_α is full-rank, one can also obtain the qFI as [56]

$$I_q(\rho_\alpha) = \text{Tr}(\partial_\alpha \rho_\alpha)^2 + \frac{1}{\det(\rho_\alpha)} \text{Tr}(\rho_\alpha \partial_\alpha \rho_\alpha)^2. \quad (\text{D6})$$

Finally, for a pure state $\rho_\alpha = |\psi_\alpha\rangle\langle\psi_\alpha|$, qFI is

$$I_q(\psi_\alpha) = 4 \left(\langle \partial_\alpha \psi_\alpha | \partial_\alpha \psi_\alpha \rangle - |\langle \partial_\alpha \psi_\alpha | \psi_\alpha \rangle|^2 \right).$$

Appendix E: Upper bound on the total variance

As we mentioned in Section IV B, basing on Eq. (40) one can upper-bound the total variance. This can be derived as follows. After multiplying both parts of Eq. (40) by H_0 and taking trace, one obtains

$$\text{Tr } \tilde{\rho} H_0^2 = \frac{1-k}{L} \int_a^b (\text{Tr } \rho_\alpha H_0)^2 d\alpha + \frac{k}{L} \int_a^b \alpha \text{Tr } \rho_\alpha H_0 d\alpha \quad (\text{E1})$$

Let us assume $k \leq 1$, so that the first term in the right part of (E1) be non-negative. The integral in this term can be upper-bounded with the use of inequality (39) as

$$\int_a^b (\text{Tr } \rho_\alpha H_0)^2 d\alpha \leq \int_a^b \text{Tr } \rho_\alpha H_0^2 d\alpha = L \text{Tr } \tilde{\rho} H_0^2, \quad (\text{E2})$$

where in the last step the integration was put under the trace and definition (41) of $\tilde{\rho}$ was used.

With the use of Eq (E2) one arrives at an inequality

$$\text{Tr } \tilde{\rho} H_0^2 \leq (1 - k) \text{Tr } \tilde{\rho} H_0^2 + \frac{k}{L} \int_a^b \alpha \text{Tr } \rho_\alpha H_0 d\alpha, \quad (\text{E3})$$

which can be further simplified to

$$\text{Tr } \tilde{\rho} H_0^2 \leq \frac{1}{L} \int_a^b \alpha \text{Tr } \rho_\alpha H_0 d\alpha, \quad (\text{E4})$$

with k having been eliminated. Note that the left-hand part of (E4) coincides with the quantum Bayes information (32) when the prior is uniform. In its turn, the right-hand part integral can be upper-bounded by a chain of inequalities

$$\begin{aligned} \int_a^b \alpha \text{Tr } \rho_\alpha H_0 d\alpha &\leq \left(\int_a^b \alpha^2 d\alpha \right)^{1/2} \left(\int_a^b (\text{Tr } \rho_\alpha H_0)^2 d\alpha \right)^{1/2} \\ &\leq \left(\int_a^b \alpha^2 d\alpha \right)^{1/2} \left(L \text{Tr } \tilde{\rho} H_0^2 \right)^{1/2} \\ &= \left(\frac{(b^3 - a^3)}{3} L \text{Tr } \tilde{\rho} H_0^2 \right)^{1/2}, \end{aligned} \quad (\text{E5})$$

where the first step is due to the Cauchy-Schwarz inequality and on the second step Eq. (E2) was used. Combining (E4) and (E5), after simple arithmetic one obtains

$$\text{Tr } \tilde{\rho} H_0^2 \leq \frac{b^3 - a^3}{3L}. \quad (\text{E6})$$

The total variance can be expressed as follows

$$\begin{aligned} \int_a^b \Delta^2 H_0 d\alpha &= \int_a^b (\text{Tr } \rho_\alpha H_0^2 - (\text{Tr } \rho_\alpha H_0)^2) d\alpha \\ &= L \text{Tr } \tilde{\rho} H_0^2 - \int_a^b (\text{Tr } \rho_\alpha H_0)^2 d\alpha \\ &= k \int_a^b \left(\alpha \text{Tr } \rho_\alpha H_0 - (\text{Tr } \rho_\alpha H_0)^2 \right) d\alpha, \end{aligned} \quad (\text{E7})$$

where in the last step Eq. (E1) was used. Note that (E7) holds for any finite k as condition $k \leq 1$ was not used here. From this expression, one comes to the remark which concludes Section IV B. Namely, the optimal observable H_0 cannot have a bias vanishing on the whole interval $[a, b]$.

Returning to the case $k \leq 1$, the first term in the rightmost part of (E7) can be upper bounded with the use of (E5) and (E6):

$$\int_a^b \alpha \text{Tr } \rho_\alpha H_0 d\alpha \leq \frac{b^3 - a^3}{3}. \quad (\text{E8})$$

As for the second term, one can exploit convexity of the function $f(x) = x^2$ and write

$$\int_a^b (\text{Tr } \rho_\alpha H_0)^2 d\alpha = L \int_a^b \frac{1}{L} (\text{Tr } \rho_\alpha H_0)^2 d\alpha \geq L \left(\int_a^b \frac{1}{L} \text{Tr } \rho_\alpha H_0 d\alpha \right)^2. \quad (\text{E9})$$

The right side of Eq. (E9) can be evaluated with the use of Eq. (42), which yields

$$\int_a^b (\text{Tr } \rho_\alpha H_0)^2 d\alpha \geq \frac{(b^2 - a^2)^2}{4L}. \quad (\text{E10})$$

Finally, combining (E7), (E8), and (E10), one obtains the upper bound (43) for the total variance:

$$\int_a^b \Delta^2 H_0 d\alpha \leq k \left(\frac{b^3 - a^3}{3} - \frac{(b^2 - a^2)^2}{4L} \right). \quad (\text{E11})$$

Putting $a = 0$ and $b = L$, one reproduces the expression (44) for the average total variance

$$\frac{1}{L} \int_0^L \Delta^2 H_0 d\alpha \leq \frac{kL^2}{12}. \quad (\text{E12})$$

Appendix F: Bipartite entanglement

Consider a bipartite state ρ_{AB} defined on Hilbert space $\mathcal{H}_{AB} = \mathcal{H}_A \otimes \mathcal{H}_B$. The state is called *separable* if it can be represented by an ensemble of product states

$$\rho_{AB} = \sum_i p_i \rho_A^i \otimes \rho_B^i, \quad (\text{F1})$$

with ρ_A^i and ρ_B^i defined on \mathcal{H}_A and \mathcal{H}_B , respectively.

A bipartite state is called *entangled* if it is not separable. In general, it is hard to determine whether a given mixed state is entangled or separable even if one has full access to its density operator [145].

Entanglement measures [107–110] are used to quantify, in some sense, the amount of entanglement present in quantum states. A number of measures have been introduced, but only few of them have clear operational meaning and direct relation to protocols of quantum information processing [113, 146–148]. Nevertheless, even abstractly introduced measures are able to show the presence of entanglement in the sense that they vanish on separable states and take non-zero values on entangled ones. It was shown that computation of such entanglement measures for general states in high dimensions is NP-complete [132].

One of the most efficient theoretical ways to detect entanglement in a bipartite state is to analyze its partial transpose [149]. The *partial transpose* operation ρ^{T_B} with respect to party B is defined by its action on elementary operators as

$$|ij\rangle\langle kl|^{T_B} = |il\rangle\langle kj| \quad (\text{F2})$$

and is extended on arbitrary operators by linearity. If a state is separable, i.e., is of the form (F1), then its partial transpose is necessarily positive, i. e. the state satisfies the *positive partial transpose (PPT) condition*. Consequently, if ρ^{T_B} has at least one negative eigenvalue, i.e. the state violates PPT condition, then its entanglement is detected (*PPT criterion*). The entanglement quantifier, which is related to this approach, is called *negativity* [150, 151] and is defined as

$$N(\rho) = \|\rho^{T_B}\|_1 - 1, \quad (\text{F3})$$

where $\|A\|_1 = \text{tr}\sqrt{A^\dagger A}$ is the trace norm of A .

It is known that the PPT condition is necessary and sufficient for separability of qubit-qubit and qubit-qutrit quantum states [152]. For higher dimensions, there are entangled states with positive partial transpose and, correspondingly, vanishing negativity. In this respect, the negativity is a *faithful* entanglement measure only for qubit-qubit and qubit-qutrit cases. While the definition of negativity can be modified to detect *all* mixed entangled states also in higher dimensions [153], we use expression (F3) because of its practicality and simplicity for the qubit-qubit case, the only case we concentrate on in the present work.

For the qubit-qubit case there is another expression [154] for negativity:

$$N(\rho) = 2 \max\{-\lambda_{\min}(\rho^{T_B}), 0\}, \quad (\text{F4})$$

where $\lambda_{\min}(\rho^{T_B})$ is the smallest eigenvalue of ρ^{T_B} .

Appendix G: Average performance of nonlinear entanglement witnesses with many copies

Here we use the results of Ref. [130] to get insight into the effect of multiple copies on detecting entanglement.

A linear witness is a Hermitian operator (observable) W such that $\text{Tr} \rho_{\text{sep}} W \geq 0$ for all separable states ρ_{sep} and $\text{Tr} \rho_{\text{ent}} W < 0$ for *some* entangled states ρ_{ent} that are detected by this witness. In a multi-copy scenario, one can consider nonlinear witness \mathcal{W} such that $\text{Tr} \rho_{\text{sep}}^{\otimes k} \mathcal{W} \geq 0$ for all separable states ρ_{sep} and $\text{Tr} \rho_{\text{ent}}^{\otimes k} \mathcal{W} < 0$ for some entangled states ρ_{ent} . Such a witness is constructed as a tensor product of linear witnesses:

$$\mathcal{W} = W^{(1)} \otimes \dots \otimes W^{(n)}, \quad (\text{G1})$$

where input and output dimensions of states $\rho^{\otimes k}$ and witnesses should match. As an example, for k copies of a bipartite state ρ_{AB} the structure of \mathcal{W} will be

$$\mathcal{W} = W_{A_1 \dots A_k}^{(1)} \otimes W_{B_1 \dots B_k}^{(2)} \quad (\text{G2})$$

and the average of the observable with respect to k copies of ρ is

$$\langle \mathcal{W} \rangle_{\rho^{\otimes k}} = \text{Tr} \rho_{A_1 B_1} \otimes \dots \otimes \rho_{A_k B_k} \mathcal{W}. \quad (\text{G3})$$

In Ref. [130] it has also been observed that some of the linear witnesses $W^{(i)}$ in (G1) can be replaced with specific positive operators $P^{(i)} > 0$, and the resulting nonlinear witness \mathcal{W} might get even stronger.

In order to consider average performance on random pure bipartite states we follow the lines of Appendix F of Ref. [130] and make special choice of operators $W^{(1)}$ and $W^{(2)}$ in eq. (G2). The first one will be

$$W_{A_1 \dots A_k}^{(1)} = \mathbb{1} - k! P_{A_1 \dots A_k}^-, \quad (\text{G4})$$

where $P_{A_1 \dots A_k}^-$ is the projector onto the antisymmetric subspace of Hilbert space of k parties A_1, \dots, A_k , and the second one, $W_{B_1 \dots B_k}^{(2)}$, is set just to the projector $P_{B_1 \dots B_k}^-$, which is a positive operator. Note that for $k = 2$ copies the resulting nonlinear witness is proportional to the lower bound on squared concurrence in (67).

The average over k copies of Haar-random states $|\psi\rangle \in \mathbb{C}^d$, with $d = d_1 \times d_2$ (4 for 2 qubits), reads

$$\mathbb{E}[\langle \mathcal{W} \rangle] = \int \text{Tr} \mathcal{W} |\psi\rangle\langle\psi|^{\otimes k} d\psi, \quad (\text{G5})$$

and the well-known expression [155] can be used:

$$\int |\psi\rangle\langle\psi|^{\otimes k} d\psi = \binom{d+k-1}{k}^{-1} P_{k,d}^+, \quad (\text{G6})$$

where $P_{k,d}^+$ is the projector onto the symmetric subspace of Hilbert space of k parties, each of dimension d .

Calculation of (G5) with the use of (G6) yields (Ref. [130], eq. (F10)):

$$\mathbb{E}[\langle \mathcal{W} \rangle] = \binom{d+k-1}{k}^{-1} \left(\text{Tr} P_{k,d_1}^- \right)^2 (1 - k!), \quad (\text{G7})$$

where P_{k,d_1}^- - the projector onto the anti-symmetric subspace of Hilbert space of k parties, each of dimension d_1 (here we assume that $d_1 = d_2$). One cannot use (G7) for arbitrarily large number of copies k , since

$$\text{Tr} P_{k,d_1}^- = \begin{cases} \binom{d_1}{k} & \text{if } k \leq d_1, \\ 0 & \text{if } k > d_1 \end{cases} \quad (\text{G8})$$

is the dimension of the antisymmetric subspace of k parties with local dimension d_1 , and the projector vanishes when $k > d_1$. Therefore, for two-qubit states, i. e., when $d_1 = d_2 = 2$, the number of copies is limited by 2. Nevertheless, the following argument can be used. One can take bipartite states with local parties of sufficiently large dimensions d_1 and d_2 and then "split" each local dimension into a tensor product of smaller ones. Let us say, $d_1 = d_2 = 2^s$, then each such subsystem can be split into s one-qubit systems. If the initial state ρ_{AB} factorizes, under splitting operation, into tensor product of s identical two-qubit states, then using k copies of ρ_{AB} will result in ks copies of some two-qubit state. Note also that in this case the entanglement of the initial state is fully determined by the entanglement of its factors. Of course, not every pure state factorizes under splitting operation exactly into a tensor product of states with smaller local dimensions, but averaging in (G5) is performed over Haar-random states, and

this set includes those states that factorize. The simplest example of a factorizable entangled state is the Bell's state of dimension d^2

$$\frac{1}{\sqrt{d^2}} \sum_{l=1}^{d^2} |l\rangle_A |l\rangle_B = \frac{1}{\sqrt{d^2}} \sum_{i,j=1}^d |ij\rangle_A |ij\rangle_B \longrightarrow \left(\frac{1}{\sqrt{d}} \sum_{i=1}^d |i\rangle_{A'} |i\rangle_{B'} \right) \otimes \left(\frac{1}{\sqrt{d}} \sum_{j=1}^d |j\rangle_{A''} |j\rangle_{B''} \right), \quad (\text{G9})$$

where the parties A and B of dimension d^2 are split into d -dimensional parties A' and A'' , B' and B'' , respectively. Splitting results in two identical Bell's states of smaller dimension d .

Now we can use eq. (G7) for k copies, $d_1 = d_2 = 2^s$ and, consequently, $d = d_1 d_2 = 2^{2s}$. Averaging over such Haar-random pure states includes those that can be factorized into s identical two-qubit states. The factorization results in ks copies of such states. The reason why eq. (G7) still holds after splitting is that trace in eq. (G5) is stable under such an operation. When $k = 2$, the averaging is performed over the set which includes $2s$ copies of identical two-qubit states and results in expression

$$\mathbb{E}[\langle \mathcal{W} \rangle] = \binom{2^{2s} + 1}{2}^{-1} \binom{2^s}{2}^2 (1 - 2!) = -\frac{(2^s - 1)^2}{2(2^{2s} + 1)}. \quad (\text{G10})$$

Starting from the value -0.1 at $s = 1$ (2 copies), the average monotonically decreases and tends to -0.5 when $s \rightarrow \infty$. This decreasing of the average value of entanglement witness over random states suggests that entanglement detection becomes more effective with the increase of number of copies of two-qubit states. We can then conjecture that, when working with many copies of states, the regression model variationally finds observables like those in eqs. (G2), (G4) or maybe even more optimal ones connected with some tight bounds on entanglement measures. This could potentially explain the increase of negativity prediction accuracy on 4 copies of states which is seen on Fig. 5.